DEVELOPMENT OF A NEUTRON DIFFRACTION SYSTEM AND NEUTRON IMAGING SYSTEM FOR BEAMPORT CHARACTERIZATION

by

TROY CASEY UNRUH

B.S., Kansas State University 2004

A THESIS

submitted in partial fulfillment of the requirements for the degree

MASTER OF SCIENCE
Nuclear Engineering

Department of Mechanical and Nuclear Engineering
College of Engineering

KANSAS STATE UNIVERSITY
Manhattan, Kansas

2009

Approved by:

Major Professor
Dr. Douglas McGregor

Copyright

Acknowledgments

The author would like to thank the facility and staff of the KSU SMARTLab and the TRIGA nuclear reactor along with DTRA (contract DTRA-01-03-C-0051) and NSF IMR-MIP (Grant no. 0412208) for their support

Abstract

Semiconductor neutron detector design, fabrication and testing are all performed at Kansas State University (KSU). The most prevalent neutron detectors built by the KSU Semiconductor Materials And Radiological Technologies Laboratory (SMART Lab) are comprised of silicon diodes with ^{6}LiF as a neutron converter material. Neutron response testing and calibration of the detectors is performed in a neutron detector test facility. The facility utilizes diffraction with a pyrolytic graphite (PG) monochromator to produce a diffracted neutron beam at the northwest beamport of the KSU Training Research Isotope production General Atomics (TRIGA) Mark-II nuclear reactor. A 2-D neutron beam monitor can also be used in conjunction with the test facility for active calibrations. Described in the following work are the design, construction and operation of a neutron detector test facility and a 2-D neutron detection array.

The diffracted neutron beam at the detector test facility has been characterized to yield a neutron beam with an average Gaussian energy of 0.0253 eV. The diffracted beam yields a flux of 1.2×10^{4} neutrons/cm^{2}/s at 100 kW of reactor power. The PG monochromator is diffracting on the (002) plane that has been positioned at a Bragg angle of 15.5 degrees.

The 2-D neutron detection array has been characterized for uniform pixel response and uniform neutron detection efficiency. The 2-D 5x5 array of neutron detectors with a neutron detection efficiency of approximately 0.5 percent has been used as a beam monitor when performing detector testing. The amplifier circuits for the 5x5 array were designed at the KSU Electronics Design Lab (EDL) and were coupled to a LabVIEW field-programmable gate array that is read out by a custom LabVIEW virtual instrument. The virtual instrument has been calibrated to produce a pixel response that varies by less than two percent from pixel to pixel. The array has been used for imaging and active monitoring of the diffracted neutron beam at the detector test facility. The following work is part of on-going research to develop various types of solid state semiconductor neutron detectors.

Table of Contents

List of Figures

List of Tables

CHAPTER 1 - Introduction

The discovery of neutrons in 1932 by James Chadwick ushered in a new era of radiation research. Four years later neutron diffraction was discovered by both Halban and Preiswerk and by Mitchell and Powers. Initial experiments used radium-beryllium sources, one of few neutron sources available at the time. Neutron research was limited because the intensity of the available neutron sources was low; however, a basic understanding of neutron physics was gained with those resources that were available. With the building of "atomic piles" in the 1940's, now known as nuclear reactors, much more intense neutron beams became available and allowed researchers to study neutron physics in greater detail [1]. At the heart of these experiments are neutron detectors.

1.1 Neutron Detectors

Radiation detectors can be categorized based on many different characteristics. A convenient grouping is based on the type of radiation the detector measures, specifically non-ionizing and ionizing radiation. Non-ionizing radiation is electromagnetic radiation with an energy of less than 10 electron-volts (eV) and will not ionize an atom or a molecule. The detection of non-ionizing radiation will not be covered because the focus of the following work deals exclusively with ionizing radiation detection. Electromagnetic radiation of energy greater then 10 eV allows the medium through which the radiation traverses to be ionized and is thus classified as ionizing radiation [2]. Charged particles, photons and neutrons are also forms of ionizing radiation. All ionizing radiation detectors utilize the same basic principles. Ionizing radiation detectors rarely measure the radiation directly; instead the detectors measure the reaction products resulting from a radiation interaction in the detector. These reaction products generally produce more ionization in the form of gamma rays with the detector material [3]. Charged particles, whether measured directly or from the radiation interactions, primarily lose energy through Coulombic interactions with electrons and nuclei in matter. Under the influence of an electric field, these liberated charge carriers will move, thereby inducing an electrical current in the radiation detector [2,3].

Ionizing radiation detectors for neutrons must rely on the production of reaction products resultant from neutron interactions because neutrons have no charge to produce direct coulombic interaction with atomic bound electrons. Neutron interactions can produce a variety of secondary reaction products through some neutron scattering reactions or various neutron capture reactions. There are two types of neutron scattering reactions, elastic scattering (n,n) and inelastic scattering (n,γ). Elastic scattering transfers some of the incident neutron energy to the target nucleus and the neutron leaves in a different direction with the remaining neutron energy. Inelastic scattering requires the incident neutron to be temporarily absorbed by the target nucleus forming a compound nucleus. The nucleus is raised to an excited state that may de-excite by emitting a gamma-ray and another neutron of lower energy [2,3]. There are 3 types of neutron capture reactions commonly used for neutron detection, transmutation (n,p) or (n,α), radiative capture (n, γ), and fission reaction (n, fission). Transmutation occurs when a target nucleus absorbs a neutron forming a compound nucleus which will eventually loose energy by emitting a proton or an alpha-particle. Radiative capture also requires the target nucleus to absorb a neutron and form a compound nucleus; however the energy loss is achieved by emission of a gamma ray. A fission reaction occurs when a heavy target nucleus absorbs a neutron and gains a large excess of energy. The highly excited compound nucleus will split into two or more lighter nuclei to release the excess energy [2,3].

All of the above neutron interactions can be used for neutron detection, however *most* neutron detectors rely on transmutation or fission reactions. The important reactions for neutron detectors are the $^{10}B(n, \alpha)^{7}Li$ reaction, the $^{3}He(n, p)^{3}H$ reaction, the $^{6}Li(n, t)^{4}He$ reaction, and the ^{235}U or ^{239}Pu fission reactions. Each of these reactions have their advantages and disadvantages for use in various neutron detectors which will be discussed below [2-5].

1.1.1 Gas-Filled Neutron Detectors

The most basic type of gas-filled radiation detector is the ion chamber. The ion chamber produces electron-ion pairs that are in proportion to the initial ionization produced by the radiation interaction with the fill gas. The predominant design of ion

chambers places an electrode or pair of electrodes inside a gas-filled chamber. The single electrode design utilizes a conducting can as the chamber and outer electrode (cathode) with a wire electrode (anode) placed down the central axis that is insulated from the can walls (Figure 1.1). Alternatively, properly spaced parallel plates insulated from each other can also be used as electrodes and placed inside a gas-filled chamber. The fill gas inside the chamber is the medium that ionizing radiation interacts with to create electron-ion pairs. The application of a low DC voltage (<400 volts) between the electrodes creates the electric field needed for charge collection. A higher applied voltage (400-2000 volts) can cause electrons to undergo avalanche multiplication, thereby producing a large number of electron-ion pairs still in proportion to the energy of the absorbed radiation [2-5]. When a gas-filled detector is operated at the higher voltages in this avalanching mode it is referred to as a proportional counter provided that the multiplication factor is still proportional to the initial absorbed energy.

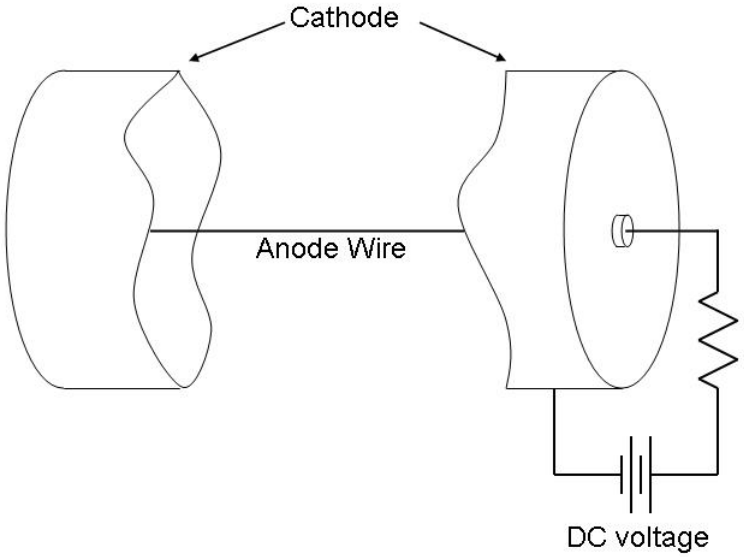

Figure 1.1: Cut-away view of a gas-filled radiation detector. The fill gas is contained within the canister, which performs as the cathode.

A gas-filled neutron detector is simply an ion chamber or proportional counter that is sensitive to neutrons. These methods include incorporation of fill gases with large neutron absorption cross sections (such as ^{3}He) or lining the walls with a neutron sensitive coating (such as ^{10}B or ^{235}U). All methods rely on the spontaneous emission of

ionizing reaction products from the initial neutron interaction. The fill gas, whether neutron absorbing or not, is typically under pressure and as such, will leak out over its operational lifetime causing the measured response to change. The general construction of a cylindrical gas-filled detector utilizes a pressurized chamber with a very thin central wire. These properties dictate that the gas-filled neutron detector can be difficult and expensive to manufacture, while also being fragile to handle and bulky to operate with the required counting electronics [2-5].

1.1.2 Scintillation Neutron Detectors

A scintillation radiation detector relies on the excited electrons from a radiation interaction in a scintillating material to emit photons (UV or visible light) as the electrons de-excite to lower energy levels. The photons are emitted isotropically so a reflector is added around the scintillator to keep photons from escaping the scintillator before the light can be detected. The photons are reflected until absorbed in the scintillator or converted into free electrons through the use of a photocathode. The amount of light produced in the scintillator is very small and is typically amplified in order to accurately measure a signal. After the conversion of a photon to an electron in the photocathode, the final signal amplification is achieved by a photomultiplier tube (Figure 1.2). The photomultiplier tube is evacuated of air and has several dynodes to amplify the electron signal. A voltage potential is applied that is divided evenly over the dynodes to produce an average of 50-120 volt drop between each dynode to generate an electric field for signal amplification [2-5].

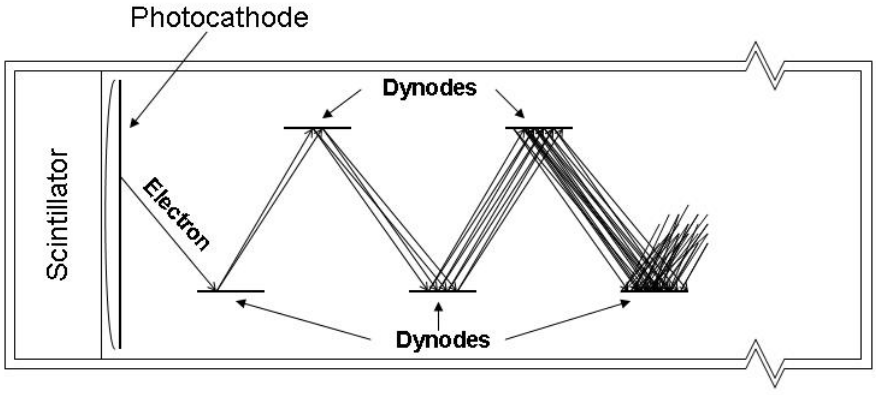

Figure 1.2: Schematic diagram of a scintillator coupled to a photomultiplier tube after a radiation interaction in the scintillator.

Lithium loaded scintillating materials, certain scintillating plastics, or Gadolinium coated scintillators can be used to generate measurable secondary reactions for the detection of neutrons. After the neutron interaction produces electron-ion pairs in the scintillating material, the scintillation detection process is the same as that used for directly detecting other types of ionizing radiation. Certain types of scintillators can be made rugged; but by comparison the photomultiplier is a fragile, bulky, and complex component needed to interpret the neutron interaction. The amplification is highly sensitive to a change in the bias voltage. Neutron-induced radiation damage can also modify the light output properties of the scintillating material [2-5].

A near-real-time alternative to using a photocathode and photomultiplier tube to detect the light from the scintillator is photographic film. The use of instant Polaroid photographic film that contains the developing chemicals in the film packet allow the neutron-induced image to be developed shortly after exposure to observe the location of the interactions [6]. The photographic film relies on a chemical reaction during exposure and development and can only be performed once. A constant supply of film is needed to operate a photographic film-based scintillation detector. The photographic film is developed at a later time after irradiation and can not provide real-time information about the neutron field.

1.1.4 Semiconductor Neutron Detectors

In semiconductor radiation detectors the radiation event is measured by the number of charge carriers set free in the detector volume as ionizing radiation produces free electron-hole pairs. The free electrons are transferred from the valence band to the conduction band in the semiconductor. The absence of electrons in the valence band also means the presence of a "hole" in the valence band. The application of an electric field across the material will cause the free charges to move and the resulting current can be measured. The output signal of the charge motion is proportional to the energy of the incident radiation. A signal from the semiconductor can be measured with appropriate counting electrons if contacts are applied to the surface [2].

There are 2 types of neutron detectors based on semiconductor radiation detectors, those being solid-state and thin-film coated neutron detectors. The solid-state neutron detectors are inherently neutron sensitive because the semiconducting material is highly neutron-reactive. Pyrolytic boron nitride, mercuric iodide (HgI_2), cadmium telluride (CdTe) and cadmium zinc telluride (CZT) have all been studied as possible solid state semiconductor neutron detectors with limited success [7-9,37]. By contrast, thin-film coated neutron detectors rely on a neutron reactive material applied to the semiconductor surface to achieve neutron sensitivity. The secondary reaction products that are emitted from the neutron interactions in the thin film can be detected in the underlying semiconductor diode as shown in Figure 1.3 [10].

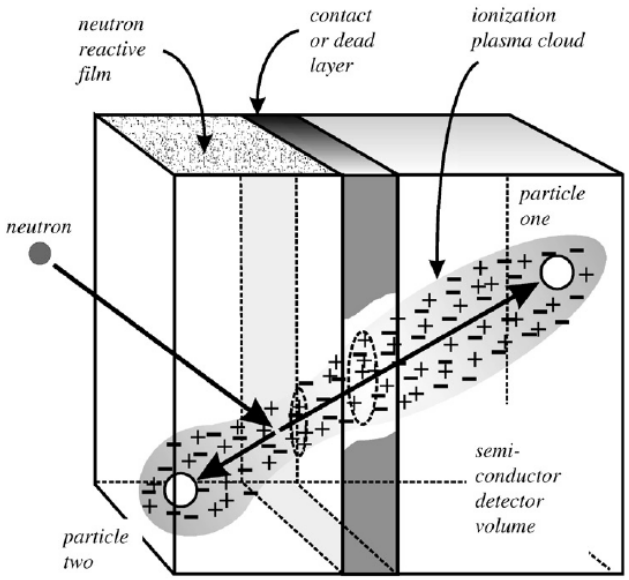

Figure 1.3: The fundamental approach to a thin-film semiconductor neutron detector [10].

The most common arrangement consists of a planar diode that has a thin film or multi-layer films of ^{6}LiF or ^{10}B applied to the surface. The ^{6}LiF and ^{10}B films generally rely on the $^{6}Li(n, \alpha)^{3}He$ and $^{10}B(n, \alpha)^{7}Li$ reactions, respectively. GaAs and silicon are the primary semiconductor substrate materials that have been coupled to the neutron reactive thin-films. Of the two materials, GaAs has shown superior radiation hardness, but silicon is less expensive, easier to process, and has a smaller neutron interaction cross-section. The majority of present work in thin-film semiconductor neutron detectors describe devices with silicon as the substrate material [10-20].

The advent of Very-Large-Scale Integration (VLSI) processing techniques has made the silicon-based semiconductor neutron detector easy to produce in mass quantities at low costs. When properly designed, the semiconductor diodes require little if any applied bias to generate an output signal. The associated counting electronics are very simple and thus have low power consumption. Semiconductors operate faster compared to other commonly used radiation detectors. All of these characteristics have made semiconductor neutron detectors the logical choice for the next generation of neutron detectors [10-20].

1.2 Detector Test Facility

The students and faculty at the Kansas State University (KSU) Semiconductor Materials And Radiological Technologies Laboratory (SMART Lab) design and construct semiconductor neutron detectors in-house. Neutron response testing and calibrations are best performed with an intense neutron source. The SMART Lab is conveniently located in the same building as an excellent neutron source, the KSU Training Research Isotope production General Atomics (TRIGA) Mark II Nuclear Reactor. The KSU TRIGA reactor was constructed with beamports to allow neutrons to be emitted from the reactor core through the biological radiation shielding. The beamports provide neutrons for use in a wide variety of experiments [21]. The beamports are operated on an "as needed" basis, so no facility specifically for neutron-detector characterization was installed.

The TRIGA reactor has 4 beamports; a fast (piercing), a tangential, and two radials as shown in Figure 1.4 [21]. The fast beamport pierces the graphite-reflector surrounding the reactor core. The neutrons emitted from the fast beamport undergo very little moderation and as a result, the fast beamport has a higher neutron flux than any of the other beamports. Many of these neutrons are high-energy (fast) upon leaving the beamport because they do not lose energy though scattering in the reflector. The gamma-ray exposure is also much greater at the fast beamport than any other beamport, and the large flux of neutrons and gamma rays make radiation shielding difficult. The shielding requirements necessary are further complicated by the fact that a brick wall, surrounding the source cave, is perpendicular and in close vicinity to the beamline (see Figure 1.4),

hence producing an environment with a large albedo neutron field. The fast beamport is seldom used and not considered as a viable option for the basis of a neutron detector testing facility because of the higher neutron energies, the higher gamma-ray exposure rates, and the limited usable floor space around the beamport.

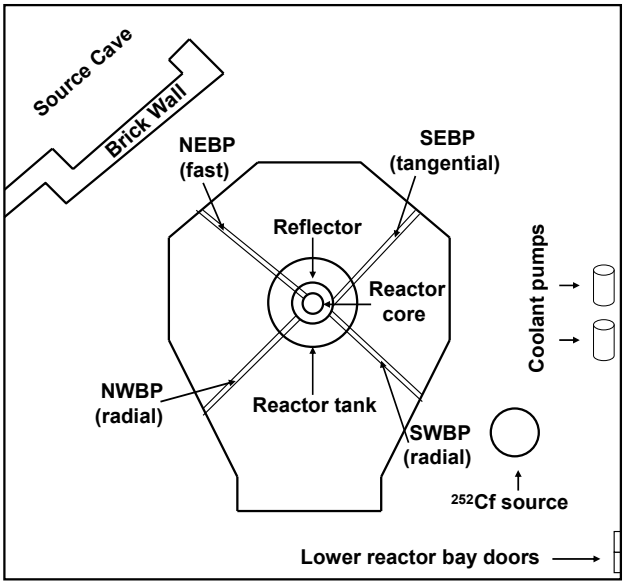

Figure 1.4: Layout of reactor bay floor showing the location of the beamports [21].

The most frequently used beamport is the beamport positioned tangentially to the reactor core. The tangential beamport position is different from the other beamports which are positioned radially and point directly at the reactor core. The tangential position requires neutrons to scatter into the beamport in order to reach the work station at the other end, which is not necessarily true for the other beamports. The tangential position results in the lowest fraction of fast neutrons in the neutron beam and the smallest gamma-ray exposure rate [21]. Installation of a neutron detector testing facility would be the most ideal at the tangential beamport as compared to the other available beamports, as is commonplace at most test reactors. However, the tangential beamport at the KSU TRIGA is widely utilized by other experimenters; as such it is not possible to occupy the beamport for extended periods of time. A neutron detector testing facility is to be a permanent installation exclusively for the support of SMART Lab neutron detector testing. Hence, the tangential beamport is not an option for a permanent testing facility.

The two remaining beamports are the moderated radial beamports, which are positioned radially to the reactor core, but do not pierce the graphite reflector. The characteristics of the radial beamports only differ in location around the reactor core; one is located southwest of the reactor core and the other is located northwest of the reactor core. These beamports are used infrequently because the characteristics of the neutron beam are not as favorable as the tangential beamport. The radial position allows for a larger fraction of fast neutrons in the neutron beam and a larger amount of gamma-ray exposure than the tangential position. The beamport opening of the southwest beamport (SWBP) is located near a permanently installed ^{252}Cf neutron source (Figure 1.4) as well as the lower reactor bay door and also the cooling system for the reactor pool [21]. The close proximity of the SWBP beamport to a neutron source, large cooling pumps and the lower reactor bay door could have negative impact on results, hence not an ideal choice for the location of a neutron detector test facility.

The northwest beamport (NWBP) is located just beneath the stairs that lead to the 21-foot-level (Figure 1.5) and below the loading dock of the reactor bay [21]. The location is favorable because very little reactor related equipment occupies the surrounding floor space leaving more room for equipment related to the detector test port.

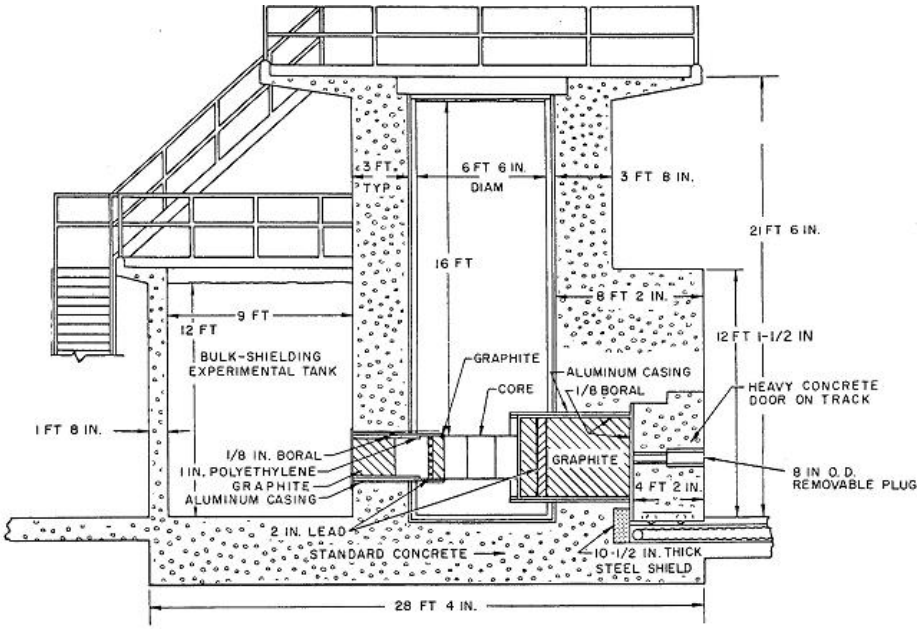

Figure 1.5: Cross sectional side-view of KSU reactor [21].

Hence the NWBP was determined the best location for the test station. Yet, one problem remained; providing an environment suitable for neutron detector characterization. Not only did this mean the neutron beam had to be well calibrated, but it also meant a workspace free from radiological hazards was necessary. Testing performed directly in the neutron beam was not an option as it left great risk for unnecessary radiation expose while repeatedly operating the detection equipment. The presence of gamma-rays was also undesirable for testing purposes because it would not allow researchers to distinguish between interaction events caused by gamma-rays as compared to events caused solely by neutrons. Finally, a monoenergetic neutron beam was desired so specific energy-dependent neutron interactions could be utilized for detector characterization purposes. To achieve the aforementioned requirements, it was necessary to use thermal neutron diffraction to deliver a monoenergetic neutron beam with a low gamma ray background.

1.2.1 Thermal Neutron Diffraction

Neutron interactions in materials are highly energy dependent. As such, it is important when performing characterization experiments involving neutrons to have a monoenergetic neutron beam. Nuclear reactors produce a wide spectrum of energies from the fission process [22-29]. The beamport leakage spectrum for a TRIGA reactor peaks near 0.04 eV as shown in Figure 1.6 [27].

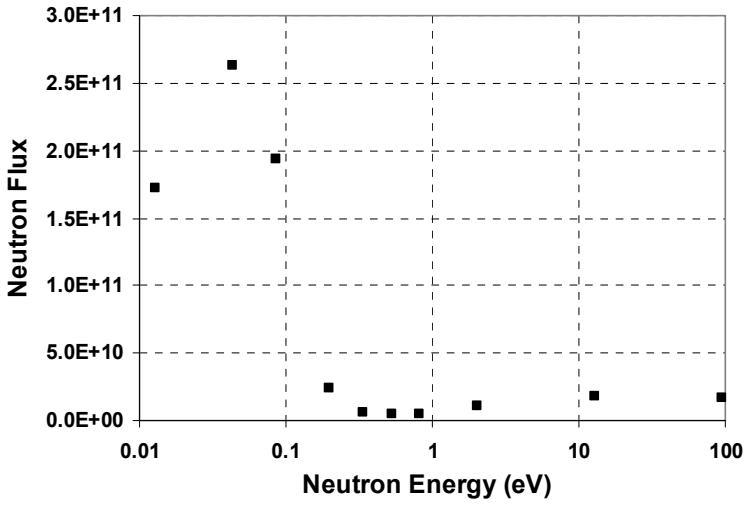

Figure 1.6: 1-D calculated neutron flux located outside graphite reflector, r = 54.2 cm for General Atomics TRIGA reactors [27].

The Maxwellian spectrum can be filtered in a variety of methods (filters, choppers, diffraction, etc.) to produce a monoenergetic neutron beam. Thermal neutron diffraction is an extremely powerful technique used in extracting monoenergetic neutron beams from nuclear reactor beamports [23-26].

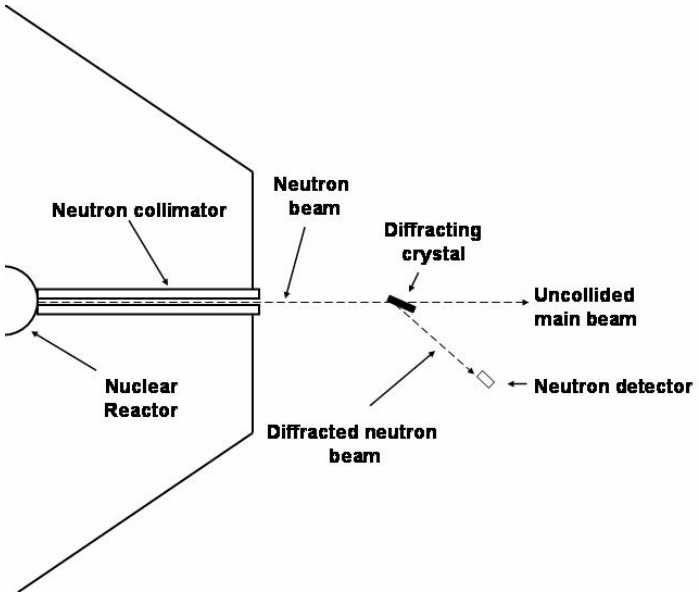

Figure 1.7: Basic components necessary to perform neutron diffraction.

The basic components needed to produce a diffracted neutron beam for a neutron detector testing facility are shown in Figure 1.7. The most important component is an intense neutron source, in this case, the KSU TRIGA nuclear reactor. The beamport opening must have a neutron collimator installed inside to narrow the size of the neutron beam to focus the neutrons on the diffracting crystal (or monochromator). The majority of the incident main neutron beam passes through the monochromator and remains undeviated. However, a small portion of the main neutron beam is diffracted by the monochromator and undergoes a change in direction dependant upon the angular position of the monochromator to the main neutron beam. Thermal neutron diffraction utilized in a neutron detector testing facility acts as a filtering device in which neutrons in a narrow range of energies are diffracted to the neutron detector located at the work station [23-26]. Radiation shielding is not shown in Figure 1.7 because it is not a necessity for neutron diffraction, however proper construction of biological shielding around the

monochromator will allow the undeviated neutrons and gamma rays to be contained within the shielding cavity. The radiological hazards from the main neutron beam will be greatly reduced while still allowing the diffracted neutron beam to escape the shielding [22, 25]. A more in-depth theoretical model for neutron diffraction will be discussed in the following chapters along with the construction of a detector test facility that utilizes neutron diffraction.

1.2.2 2-D Thin Film Semiconductor Neutron Detector

Accurate characterization of neutron detectors is essential for a successful detector testing facility. To achieve this goal, the ability to install an active neutron beam imaging system upstream of the detector testing location was necessary. The type of detector required for upstream imaging is typically referred to as a beamport monitor. The basic design utilizes a low efficiency neutron detector that allows the neutron beam to remain relatively unperturbed as it travels through the beamport monitor to the experimental testing location. The design of the beamport monitor for the detector test facility utilizes a thin film semiconductor neutron detector that groups 25 equally sized and spaced diodes on a single substrate [20]. A more in-depth theoretical model for thin film semiconductor neutron detectors is developed in the following chapters, along with the fabrication and construction of a 2-D neutron detection array.

CHAPTER 2 - Theory

De Broglie postulated that if photons have particle-like properties, then particles must have wave-like properties. Later, in 1927 Davisson and Germer demonstrated the concept that particles have wave-like properties by diffracting electrons off of Ni crystals [30]. The concept of wave-particle duality was later applied to neutrons and the technique of neutron diffraction was born [1]. Neutrons that come into thermal equilibrium with the thermal motion of the surrounding atoms with wavelengths on the order of the atomic spacing are referred to as thermal neutrons [3]. Thermal neutrons can be diffracted and are used in the present work to provide a thermal neutron beam to test thin film semiconductor neutron detectors. A theoretical basis for the detection of thermal neutrons by thin film semiconductor neutron detectors and thermal neutron diffraction is discussed in the following chapter.

2.1 Thin Film Semiconductor Neutron Detectors

Various types of particles can be observed through interactions with matter. Photons in the optical range are measurable because our eyes are sensitive to the light quanta. Gamma rays have no charge, so interactions with electrons are needed for detection. The simplest interaction that can be measured is a result of the Coulomb effect. Neutrons also have zero net charge, so Coulombic forces are generally not measured. However, neutrons can transfer kinetic energy, along with binding energy, to liberate charged particles, alpha particles for instance, that will allow excitation of other particles, such as electrons, through Coulombic forces. The nuclear reaction by-products allow the presence of neutrons to be observed [4-6].

Certain semiconductors are inherently neutron sensitive because the semiconducting material is neutron-reactive [7-9]. Other semiconductors must have a neutron-reactive material added to achieve neutron sensitivity. The KSU SMART Lab specializes in thin-film-coated neutron detectors [10-20]. The following sections

describe a basis for semiconductor neutron detectors, which will be further developed specifically for thin-film ^{6}LiF coatings.

2.1.1 Common Neutron Reactive Materials for Neutron Detectors

Neutron detection is generally based on measuring the reaction products from thermal neutron interactions. There are seven common non-fissile isotopes that are used to produce energetic secondary reaction products, those being ^{10}B, ^{6}Li, ^{157}Gd, ^{155}Gd, ^{113}Cd, ^{199}Hg, and ^{3}He. The reaction products may be charged particles, conversion electrons, or prompt gamma rays. The interactions of the common isotopes are the $^{10}B(n,\alpha)^{7}Li$ reaction, the $^{6}Li(n, t)^{4}He$ reaction, the $^{157}Gd(n, \gamma)^{158}Gd$ reaction, the $^{113}Cd(n, \gamma)^{114}Cd$ reaction, $^{199}Hg(n, \gamma)^{200}Hg$ reaction, and the $^{3}He(n, p)^{3}H$ reaction [7-9, 10-20].

Neutron detectors that rely on secondary gamma-ray emissions have been built and tested with marginal success. The isotopes ^{157}Gd, ^{155}Gd, ^{113}Cd, and ^{199}Hg are chosen because of the large thermal neutron absorption cross sections they possess [8,9, 11]. Purified ^{157}Gd and ^{155}Gd have the highest thermal (2200 m/s) neutron absorption cross sections of 240,000 and 58,000 barns, respectively. However, purified Gd is too expensive to be a practical coating. Natural Gd is not cost prohibitive and still has a reasonably large thermal (2200 m/s) neutron absorption cross section of 46,000 barns. Gadolinium emits various conversion electrons and gamma rays at energies ranging as high as 400 keV, but with small branching ratios. Gd can be incorporated into semiconductor materials (Gd-doped GaN for example), but the typical arrangement utilizes Gd as a coating on a semiconductor diode. Unfortunately only ~65% of absorptions result in conversion electron emissions and of those only a small fraction have energies above 150 keV. Hence gamma-ray background will always be a problem [11].

Much like Gd, ^{113}Cd has a relatively high neutron absorption cross section of 20,000 barns. However, the natural abundance of ^{113}Cd is only 12.26% leading to a 2450 barn cross section for natural cadmium. Purification of ^{113}Cd is cost prohibitive. Cadmium-based neutron detectors most commonly rely on the 558.6 and 651.3 keV prompt gamma ray emissions from a neutron interaction. Cadmium can be used as a coating on a semiconductor diode, however semiconductors that contain cadmium such

as Cadmium Zinc Telluride (CZT) offer high resolution to easily identify the prompt gamma-ray interactions. Still, the absorption efficiency for the prompt gamma rays is high, but since ~50% are radiated out of the device, efficiency can never be more then 50%, however the most recent work achieved ~4% [9].

The neutron absorption cross section of natural Hg (natural abundance of ^{199}Hg is 16.87%) is the lowest of all of the gamma-ray emitters at 374 barns. A 368 keV gamma-ray is emitted 81% of the time a neutron capture occurs. The fact that Hg is a liquid at room temperature will not allow it to be used as a practical coating on a semiconductor diode, however materials such as Mercuric Iodide (HgI_2) can be used to produce a solid state neutron detector [8].

Solid state detectors such as CZT and HgI_2 benefit from the fact that the neutron interactions occur directly in the semiconducting material, however it is possible that only partial energy will be deposited because gamma-rays may leak out of the detector under Compton scattering. Alternatively, natural Gd can be coated on a semiconductor diode to measure the conversion electrons. The conversion electrons can lose energy before entering the semiconductor diode, thereby limiting the effective film thickness. Careful spectral analysis is required for non-neutron-induced gamma-ray discrimination in a mixed radiation field. The fundamental difficulty with the materials that emit a gamma ray or conversion electron (Gd, Cd, and Hg) is that the detecting material also doubles as a gamma-ray detector, hence a low neutron field could be masked in high gamma-ray field [8,9,11].

The most studied neutron absorber films that emit energetic charged particles in recent years are ^{6}LiF and ^{10}B that utilize the ^{6}Li(n, α)^{3}H and ^{10}B(n,α)^{7}Li reaction, respectively. ^{6}Li is hygroscopic and highly reactive; hence a stable compound is used rather than the pure metal. One of the densest such compounds is ^{6}LiF, which can be produced through the following reactions, $2Li + 2H_2O \rightarrow H_2 + 2LiOH$ and $LiOH + Hf \rightarrow LiF + H_2O$. ^{6}Li has a microscopic thermal neutron absorption cross section of 940 barns. When formed in the compound with a mass density of 2.54 g cm^{-2}, pure ^{6}LiF has a macroscopic thermal (2200 m/s) neutron absorption cross section of 57.5 cm^{-1}[11] The charged particle reaction products from the ^{6}Li(n,t)^{4}He reaction are 2.73 MeV tritons and 2.05 MeV α-particles with a Q-value of 4.78 MeV. However, the entire energy of the

charged particle can not be measured by the semiconductor because the charged particle will lose energy as it passes through the film. The transmitted energy of the charged particles in the ^{6}LiF film has been determined by McGregor et. al. and is shown in Figure 2.1 [10, 11].

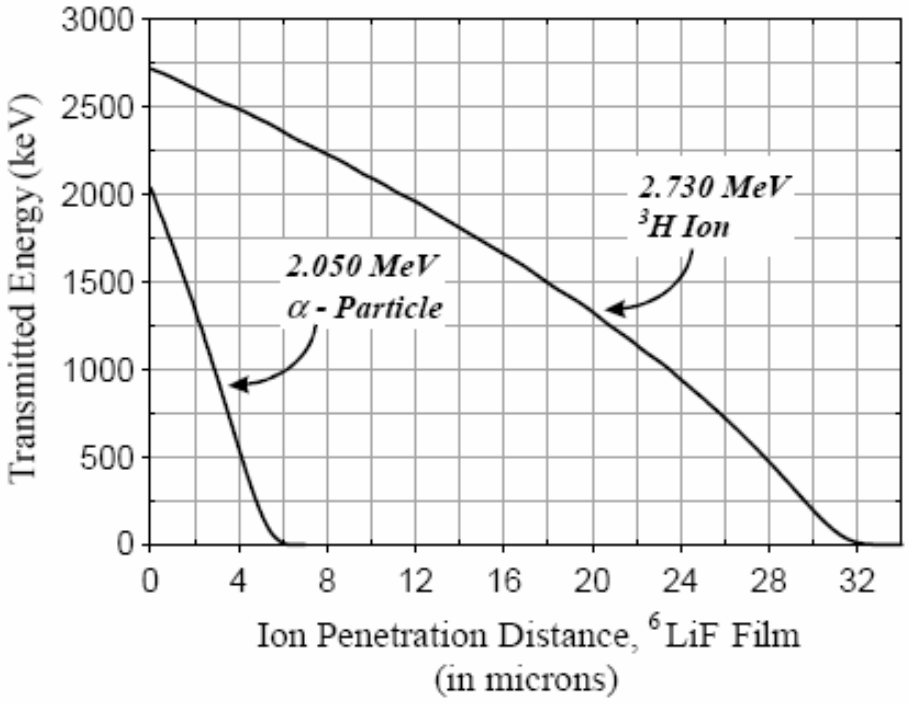

Figure 2.1: Energy deposition in a ^{6}LiF film by the charged particles from the (^{6}Li(n, α)^{3}H) reaction [10].

In contrast to ^{6}Li, ^{10}B can be handled in pure form. The microscopic and macroscopic thermal neutron absorption cross sections for ^{10}B are 3840 barns and 500 cm^{-1}, respectively [10-12, 14]. The secondary reaction products from the ^{10}B(n,α)^{7}Li reaction are 1.47 MeV α particles and 840 keV ^{7}Li ions, which are left in the 1st excited state, with a 94% branching ratio, and 1.78 MeV α particles and 1.05 MeV ^{7}Li ions with a 6% branching ratio. The ^{7}Li ions that are left in the first excited state promptly de-excite and release a 480 keV gamma ray. The overall Q-values for each reaction are 2.792 MeV for the ground state reaction and 2.310 MeV for the 1st exited state reaction. The transmitted energy of the charged particles in the ^{10}B has been determined by McGregor et. al. and is shown in Figure 2.2 [10].

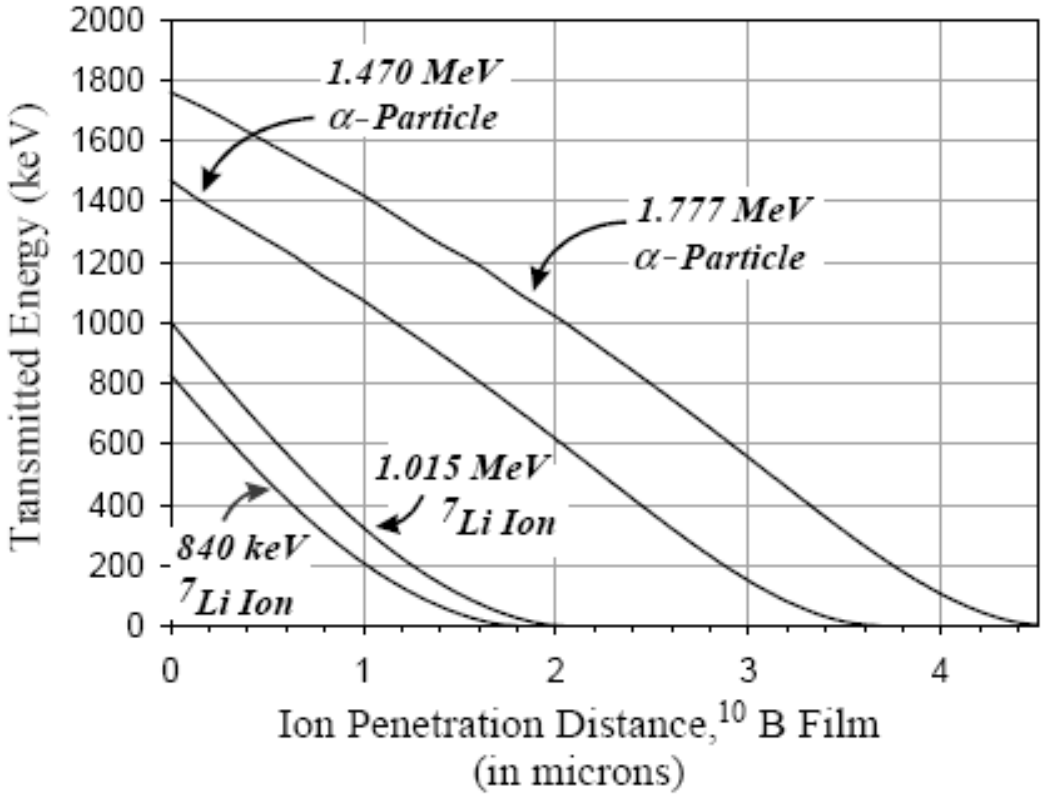

Figure 2.2: Energy deposition in a ^{10}B film by the charged particles from the $^{10}B(n,\alpha)^{7}Li$ reaction [10].

From a neutron absorption standpoint, ^{10}B seems the favorable choice to coat a semiconductor. A detector coated with ^{10}B would require less material to absorb the same amount of neutrons as a detector coated with ^{6}LiF. The detection of neutrons is not solely dependent on the absorption of neutrons; it is dependent on the secondary reaction products emitted from the neutron interaction being detected in the semiconductor diode as discussed in the following section [10,11].

2.1.2 Thin Film Semiconductor Detectors

The most common form of semiconductor neutron detector is the thin-film-coated detector. The construction of such detectors requires a semiconductor substrate, often configured as a diode, and a film of neutron reactive material that is deposited on the surface of the substrate. When the neutron-reactive material absorbs a neutron, ionizing radiation reaction products are spontaneously ejected. The ionizing radiation produces a

multitude of electron-hole pairs, which are subsequently swept from the semiconductor diode active region with an electric field. The charge generated in the active region of the diode can be measured in various electronic counting equipment [10-12, 14].

When the ionizing radiation enters the diode, it excites electron-hole pairs that can be collected in the diode. The energy deposited in the active region of the diode is typically not the full energy of the charged particle. The charged particle will lose some energy as it travels through the neutron-reactive material and front side contact. After the charged particle enters the diode, only the remaining energy can be measured. Once the charged particle is in the diode, it looses its remaining energy through Coulombic scattering that creates electron-hole pairs. An applied-bias or built-in potential is applied to the diode in order to separate the electron-hole pairs and drift the separated charges across the diode to their respective contacts. The motion of the charges to these contacts causes an induced charge to be generated across the diode that can be integrated, amplified, and measured by external circuitry [10-12,14]. The basic concept of a thin-film neutron detector is shown in Figure 2.3 as applied to the $^{6}Li(n, \alpha)^{3}H$ reaction.

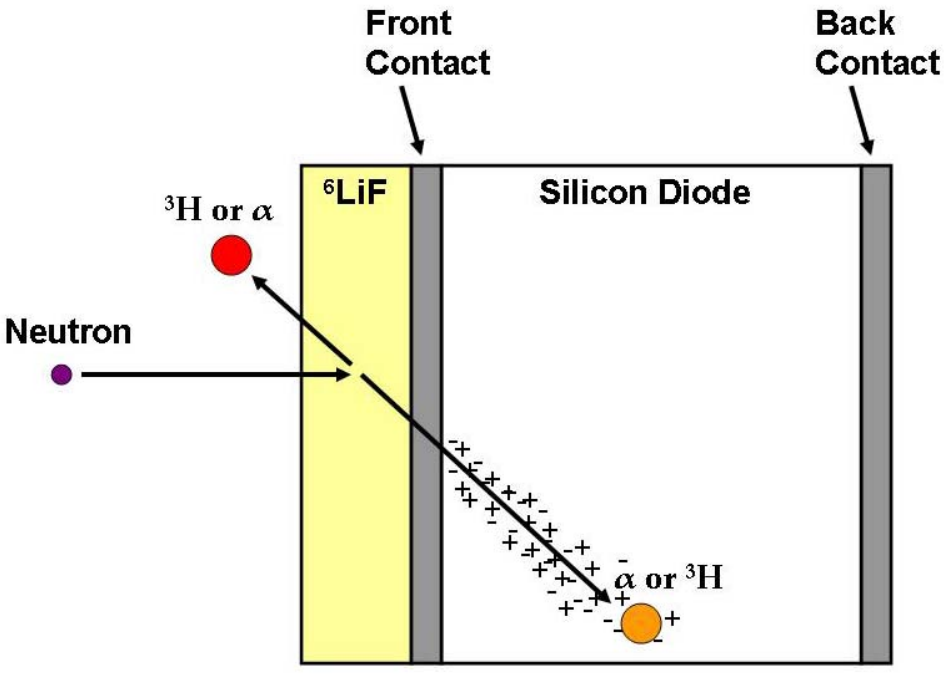

Figure 2.3: The basic concept of a thin film neutron detector with ^{6}LiF used as the neutron reactive material [10-12,14].

Conservation of mass and energy can be applied for the absorption of thermal and low energy neutrons in the various converter films. As a result, the reaction products are ejected in opposite directions (180 degrees apart) such that only one particle is directed toward the diode. The charged-particles produced by the neutron interaction travel a discrete range with some straggling about that range. The range is dependant on the initial energy of the particle and the material the particle is traveling through. As a consequence, the neutron reactive material must be thick enough to absorb a sufficient amount of neutrons, but not so thick that the reaction products lose too much energy before they reach the diode active region. The result is that only a limited amount of usable neutron reactive film can be applied to the surface of the diode. Limiting the amount of neutron absorber therefore limits the overall neutron counting efficiency of the detector [10,11].

The secondary charged particle ranges, or track lengths, in the neutron reactive material play an important role in determining the neutron detection efficiency. However for the reaction products to be detected, they must still have measurable energy when they reach the diode surface. This residual energy will be referred to as the minimum-detection-threshold-energy because it specifies the threshold of the energy required for detection. Thus, the overall particle range is not an accurate representation of the *effective* particle range because the particle energy must be above the threshold energy for detection. For this reason, a minimum-detection-threshold-energy is chosen that instead specifies the average-effective-range L of the particles in the thin-film. The average effective charged particle ranges for various minimum detection threshold energies for the $^{10}B(n,\alpha)^{7}Li$ and $^{6}Li(n, \alpha)^{3}H$ reactions in their respective converter films have been calculated by McGregor et. al. and are shown in Table 2.1 [10].

Table 2.1: Average effective charged particle ranges *L* for various minimum detection threshold energies for the $^{10}B(n,\alpha)^{7}Li$ and $^{6}Li(n, \alpha)^{3}H$ reactions [10].

Minimum detection threshold (keV)	$^{6}Li(n,\alpha)^{3}H$ Reaction, in ^{6}LiF		$^{10}B(n,\alpha)^{7}Li$ Reaction, in ^{10}B			
	2.730 MeV Triton	2.050 MeV α-particle	1.777 MeV α-particle	1.470 MeV α-particle	1.015 MeV ^{7}Li ion	840 keV ^{7}Li ion
	L (μm)	*L* (μm)	*L* (μm)	*L* (μm)	*L* (μm)	*L* (μm)
100	30.754	5.311	4.016	3.139	1.515	1.280
200	29.958	4.943	3.748	2.872	1.253	1.018
300	29.239	4.645	3.523	2.648	1.045	0.810
400	28.523	4.378	3.315	2.439	0.867	0.632
500	27.783	4.217	3.112	2.236	0.706	0.471
600	27.005	3.883	2.909	2.033	0.555	0.320
700	26.185	3.642	2.702	1.826	0.411	0.176
800	25.320	3.401	2.489	1.614	0.272	0.037

The average effective charged particle range is a general indicator of the detection effectiveness of a secondary charged particle. However, a more accurate indication of the overall detection effectiveness is realized when the average effective charged particle range *L* is multiplied by the macroscopic absorption cross section Σ for the neutron reactive coating. A high ΣL product will lead to greater overall neutron detection efficiency. The products ΣL for the $^{10}B(n,\alpha)^{7}Li$ and $^{6}Li(n, \alpha)^{3}H$ reactions in their respective converter films have been calculated by McGregor et.al and are shown in Table 2.2 [10].

Table 2.2: ΣL products for the $^{10}B(n,\alpha)^{7}Li$ and $^{6}Li(n, \alpha)^{3}H$ reactions [10].

Minimum detection threshold (keV)	$^{6}Li(n,\alpha)^{3}H$ Reaction, in ^{6}LiF (Σ = 57.51 cm^{-1} at 0.0259 eV)		$^{10}B(n,\alpha)^{7}Li$ Reaction, in ^{10}B (Σ = 500.00cm^{-1} at 0.0259 eV)			
	2.730 MeV Triton	2.050 MeV α-particle	1.777 MeV α-particle	1.470 MeV α-particle	1.015 MeV ^{7}Li ion	840 keV ^{7}Li ion
	ΣL	ΣL	ΣL	ΣL	ΣL	ΣL
100	0.1769	0.0305	0.2008	0.1570	0.0757	0.0640
200	0.1723	0.0284	0.1874	0.1436	0.0626	0.0509
300	0.1682	0.0267	0.1762	0.1324	0.0523	0.0405
400	0.1640	0.0252	0.1657	0.1219	0.0433	0.0316
500	0.1598	0.0238	0.1556	0.1118	0.0353	0.0235
600	0.1553	0.0223	0.1454	0.1017	0.0277	0.0160
700	0.1506	0.0209	0.1351	0.0913	0.0205	0.0881
800	0.1456	0.0196	0.1245	0.0807	0.0136	0.0187

The counting response of the detector is also dependent on the direction of the neutron irradiation. A front-side irradiation will allow neutrons to be attenuated in the absorber before reaching the thin-film/semiconductor interface. Whereas a back-side irradiation will allow neutrons to reach the thin-film semiconductor interface before reaching the absorber. Careful selection of the substrate can reduce scattering and absorption. The back-side arrangement leads to neutrons that are more likely to be absorbed near the thin-film/semiconductor interface. For this reason, back-side irradiation leads to higher detection efficiencies [10]. The counting efficiencies for the various film thicknesses and irradiation arrangements of ^{10}B and ^{6}LiF has been rigorously determined by McGregor et. al. and are plotted in Figure 2.4 below [10]. The present work utilizes ^{6}LiF as the neutron reactive coating on a front-side irradiated semiconductor substrate. The following section focuses specifically on calculating the thermal neutron detection efficiency as a function of ^{6}LiF film thickness for a front side irradiated detector.

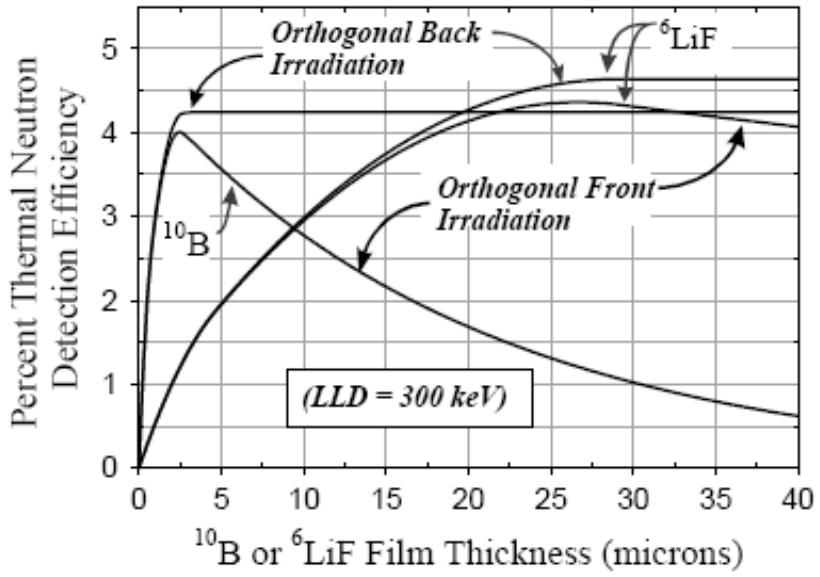

Figure 2.4: Theoretical thermal neutron detection efficiencies for front and back side irradiated thin-film neutron detectors with a minimum detection threshold energy of 300 keV [10].

2.1.3 Detection Efficiency for a ^{6}LiF Coating

The absorption cross-section of the ^{6}Li in the ^{6}LiF compound has a 1/v dependence, meaning the cross section decreases linearly with increasing neutron energy. This 1/v dependence allows the reaction rate to remain constant over a wide range of neutron energies, approximately 10^{-2} to 10^{3} eV, as shown in Figure 2.5 [11, 31].

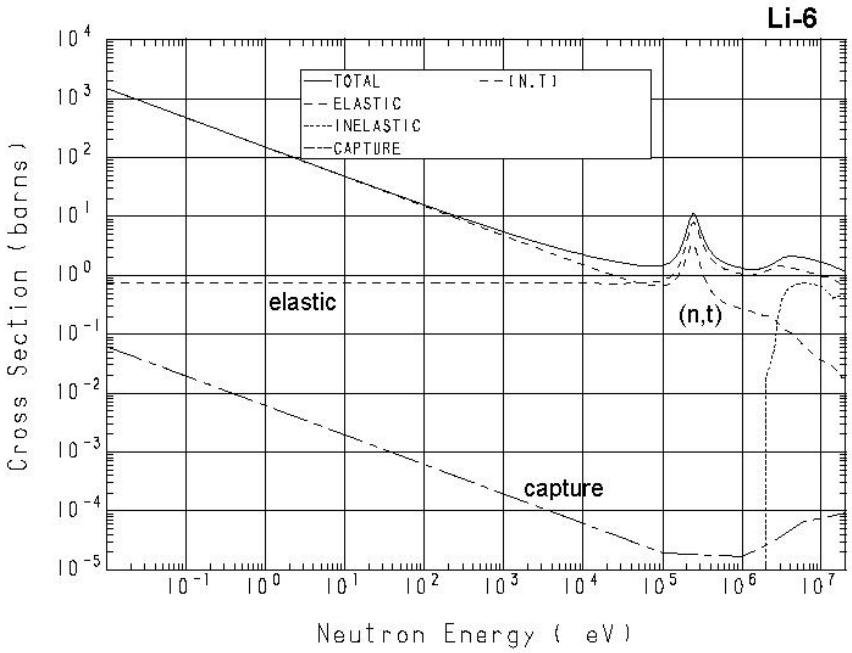

Figure 2.5: Cross section data for ^{6}Li [31].

The amount of ^{6}LiF deposited on the surface of the semiconductor diode coupled with the secondary reaction product track length will determine the neutron detection efficiency of the neutron detector. The track length of the secondary reaction products when traveling in ^{6}LiF compound are 32.1 μm for the ^{3}H and 6.11 μm for the α-particle. A minimum detection threshold energy of 300 keV yields the average effective range of 29.24 μm for the ^{3}H and 4.65 μm for the α-particle [10].

The transmission for an initial neutron flux (I_o) through a film as a function of distance (x) is given by [10],

$$I(x) = I_0 e^{-x\Sigma_F} \quad , \tag{2.1}$$

where $\sum_F$ is the film macroscopic thermal neutron absorption cross section. Solving for the neutrons absorbed in the film is given by [10],

$$1-\frac{I(x)}{I_0}=1-e^{-x\Sigma_F} \quad . \tag{2.2}$$

The neutron absorption probability per unit distance is needed to determine the location of the neutron interaction and is given by [10],

$$p(x)\,dx=\Sigma_F\, e^{-x\Sigma_F}\,dx \quad . \tag{2.3}$$

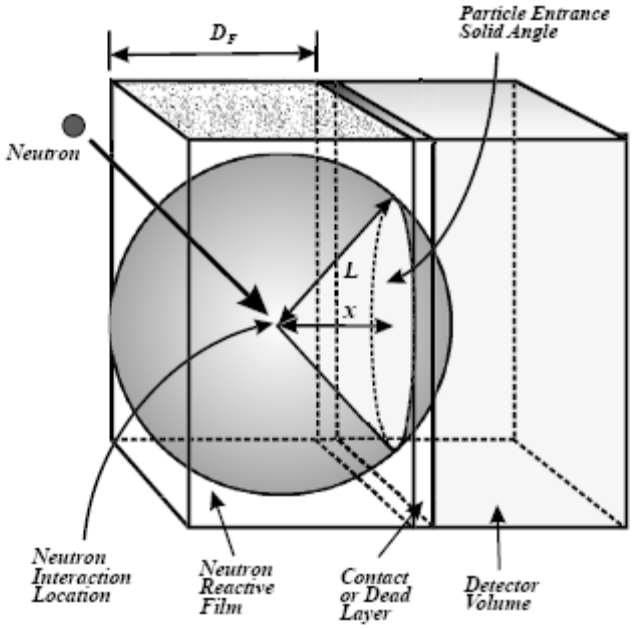

Figure 2.6: Solid angle subtending the surface of the detector [10].

After the neutron absorption at a distance x from the semiconductor surface, the reaction products are emitted with a probability of entering the active detector volume as depicted in Figure 2.6. The solid angle subtending the surface of the detector within the effective range (L) of the particle interaction is given by [10],

$$p_p(x)=\frac{\Omega(x)}{4\pi}=\frac{2\pi}{4\pi}\left(1-\frac{x}{L}\right)=0.5\left(1-\frac{x}{L}\right), \quad x\le L \ , \tag{2.4}$$

where the subscript "p" determines the reaction product. The efficiency for detecting the reaction product particle is found by integrating over the product of the probability for interaction and the fractional solid angle in the film of thickness (D_F).

Hence, the probability that a neutron causes a response in the semiconductor, defined as the neutron detection efficiency, is given by the relationship for each charged particle as a function of ^{6}LiF film thickness (D_F) for front-side irradiation (neutrons

impinging upon the film before the detector). The neutron detection efficiency (S_P) for this case has been derived by McGregor et. al., the result is given here by [10],

$$S_P(D_F) = \frac{F_P}{4\pi I_0}\int_0^{D_f} I_0 2\pi \Sigma_F e^{-\Sigma_F (D_F - x)}\left(1-\frac{x}{L}\right) dx$$

$$= 0.5F_P\left\{\left(1+\frac{1}{\Sigma_F L}\right)(1-e^{-\Sigma_F D_F})-\frac{D_F}{L}\right\}, \qquad (2.5)$$

for $D_F \le L$, and [10],

$$S_P(D_F) = \frac{F_P e^{-\Sigma_F (D_F - L) D_F}}{4\pi I_0}\int_0^{L} I_0 2\pi \Sigma_F e^{-\Sigma_F (D_F - x) D_F}\left(1-\frac{x}{L}\right) dx$$

$$= 0.5F_P e^{-\Sigma_F (D_F - L)}\left\{\left(1+\frac{1}{\Sigma_F L}\right)(1-e^{-\Sigma_F L})-1\right\}, \qquad (2.6)$$

for $D_F > L$, where F_p is the branching ratio of the reaction product emissions, L is the average effective range of the secondary charged particle, and $\sum_F$ is the macroscopic thermal (2200 m/s) neutron absorption cross section of the ^{6}LiF. Then the total efficiency is found by summing each of the reaction product efficiencies [10],

$$S(D_F)\big|_{Total} = \sum_{p=1}^{N=2} S_p(D_F). \qquad (2.7)$$

Applying the constants for a minimum detection threshold energy of 300 keV from Table 2.2 yields the simplified form of Eq. (2.5) and Eq. (2.6) that are then inserted into Eq. (2.7) to yield [10],

$$S(D_F)\big|_{Total} = 22.67(1-e^{-0.005751\ D_F}) - 0.1246\ D_F \quad , \qquad (2.8)$$

for $D_F \le 4.65$, and

$$S(D_F)\big|_{Total} = -3.4666\, e^{-0.005751\ D_F} - 0.0171\ D_F + 3.4734 \quad , \qquad (2.9)$$

for $4.65 < D_F \le 29.24$

$$S(D_F)\big|_{Total} = 0.05124\, e^{-0.005751\ D_F}, \qquad (2.10)$$

for $D_F > 29.24$ where D_F is in units of micrometers. A plot of Eqs. (2.8)-(2.10) is shown in Figure 2.7.

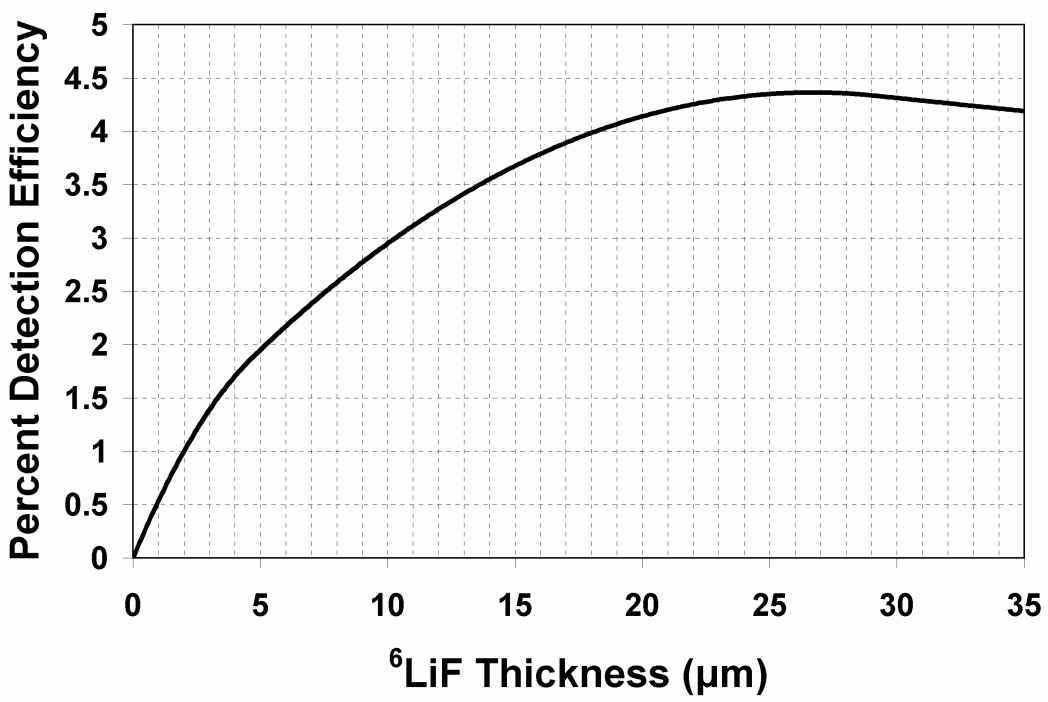

Figure 2.7: Graphical representation of Eqs. (2.8)-(2.10) for front-side irradiated thin film neutron detector.

2.2 Thermal Neutron Diffraction

In 1927 Davisson and Germer demonstrated the concept that particles have wave-like properties by diffracting electrons off of Ni crystals [30]. Neutron diffraction was first reported in March 1936 by W.M. Elsasser as he theorized how a wide range of neutron velocities in a parallel neutron beam could be diffracted by a polycrystalline powder [1,23]. Three months later, H. Halban and P. Preiswerk confirmed the theories by reporting on a neutron diffraction experiment that utilized a radium-beryllium (Ra-Be) neutron source to diffract neutrons from a cylinder of iron and simultaneously measure the direct and diffracted neutron beams [1,23]. One month later, D.P. Mitchell and P.N. Powers reported on a more refined diffraction experiment that also utilized a Ra-Be neutron source, but the diffraction was achieved using a set of large single crystals of magnesium oxide and the diffracted neutron beam was measured separately from the incident neutron beam [1,23].

Theoretically, neutron based research continued with F. Bloch in late 1936 discussing the possibility for magnetic scattering of neutrons and in 1939 O. Halpern and M.H. Johnson further theorized that it should be possible to experimentally demonstrate the magnetic scattering of neutrons with paramagnetic materials. Experimentally however, neutron research had to await the utilization of early nuclear reactors to produce more intense neutron beams for diffraction experiments. The construction of the first large neutron source, known as an 'atomic pile', by E. Fermi and his colleagues in 1942 led to the construction of other 'piles' that were utilized for neutron diffraction experiments. As time went on the 'piles' became known as nuclear reactors and the collection of nuclear cross section data grew rapidly. Scattering experiments are also performed at accelerator-based neutron sources such as the Spallation Neutron Source because of the intense pulsed neutron beam. Today neutron diffraction experiments are much different than those of the past, however the basic physics remain the same [1]. The following sections give a basis for thermal neutron diffraction, which will then be used to develop expression of the reflected intensity of a pyrolytic graphite monochromator.

2.2.1 Basic Theory

The theory that describes matter on the atomic level is known as quantum mechanics. Wave-particle duality is an important concept of quantum mechanics that describes all matter and energy as having both wave-like and particle-like properties. The first discovery in wave-particle duality was proposed with photons. Photons were first thought to only possess the properties of waves, however in 1905 Einstein proposed that photons also possessed particle-like properties. Louis-Victor de Broglie further applied wave-particle duality to all matter by introducing his formula (Eq. 2.11) relating the momentum p of the particle to the de Broglie wavelength λ_b of the particle by a physical constant known as Planck's constant h, 6.6260755 x 10^{-34} Js [32],

$$\lambda_b = \frac{h}{p} . \tag{2.11}$$

For photons, the momentum p of the photon is related to the energy E of the photon by the speed of light c because photons have zero rest mass. The relationship for photons is given by [32],

$$p = \frac{E}{c} \quad . \tag{2.12}$$

For particles that have a rest mass, the momentum p of the particle is related to the mass m of the particle by the velocity v of the particle by [32],

$$p = mv \quad . \tag{2.13}$$

Alternatively the momentum can be written in terms of the particle energy. The kinetic energy E of a non-relativistic particle is related to the particle mass m by the velocity v of the particle by [32],

$$E = \tfrac{1}{2} m v^2 \, . \tag{2.14}$$

Neutrons have a rest mass m_n of 1.6749286 x 10^{-27} kilograms [32] and from Eqs. (2.11)-(2.14) and appropriate unit conversations, the relationship between the wavelength of a neutron λ_n and the kinetic energy E of the neutron is given by [6,32]

$$\lambda_b = \frac{h}{p} = \frac{h}{m_n v} = \frac{h}{\sqrt{2 m_n E}} = \frac{0.286}{\sqrt{E}} \, , \tag{2.15}$$

where the wavelength of the neutron λ_b is in angstroms and the kinetic energy E of the neutron in electron-volts (eV) [6,32].

All matter is made of atoms bonded together with the exception of plasma. Certain materials known as crystals are bonded together in a periodic lattice. More specifically, a crystal is comprised of atomic or molecular structures that are arranged into a unit cell that is repeated in a lattice system. The distances between the lattice points are referred to as the lattice constants. When the unit cell is three dimensional, it is generally defined by three lattice constants a, b, and c. However for hexagonal crystal structures a and b are equal, so only a and c are used to define the lattice constants. Similarly for cubic crystal structures, all of the constants are equal, so only the constant a is used to define the lattice constants. The lattice planes of a 3 dimensional lattice can be defined by Miller indices. Miller indices h,k,l are integers for a notation system that gives the orientation and position in respect to the crystallographic axes of a crystal plane in terms of the lowest common integer of the reciprocal of the lattice vectors the plane intersects. The distance d between crystal planes in a material can be determined if the lattice constants and Miller indices are known by, [30]

$$\frac{1}{d^2} = \frac{h^2}{a^2} + \frac{k^2}{b^2} + \frac{l^2}{c^2} . \tag{2.16}$$

Bragg diffraction relies on the atomic spacing between the planes of a crystalline material to allow waves of discrete wavelengths to be diffracted by the crystal planes. Electrons, X-rays, and neutrons have all been shown to Bragg diffract. The wavelength λ of the diffracted particle is defined by the relationship between the crystal plane spacing *d* of the diffracting material and the elastic scattering angle θ_B as shown in Figure 2.8 and in Eq. (2.17) [6,23-25],

$$n\lambda = 2d \sin\theta_B . \tag{2.17}$$

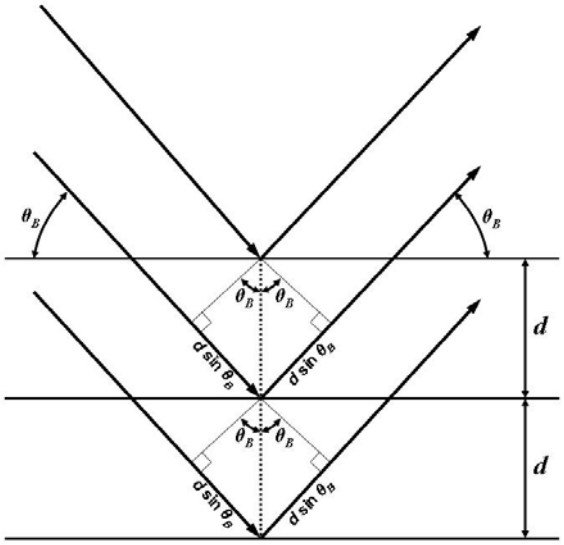

Figure 2.8: Depiction of Bragg diffraction off of crystal planes with spacing *d* and an incident particle angle of θ_B.

Bragg diffraction at a nuclear reactor beamport can be used to produce a monoenergetic beam of neutrons as shown in Figure 2.9. The radial and tangential beamport leakage spectrums from a nuclear reactor contain a Maxwellian distribution of thermal neutron energies [23-27]. When the Bragg condition is satisfied, neutrons of wavelength nλ (*n* = 1, 2, 3 and so on) will be diffracted. The different energies of neutrons that are diffracted in the crystal for a specific Bragg angle are referred to as the crystal harmonics. The harmonics will cause neutrons of different energies to contaminate the refracted neutron beam [23-26].

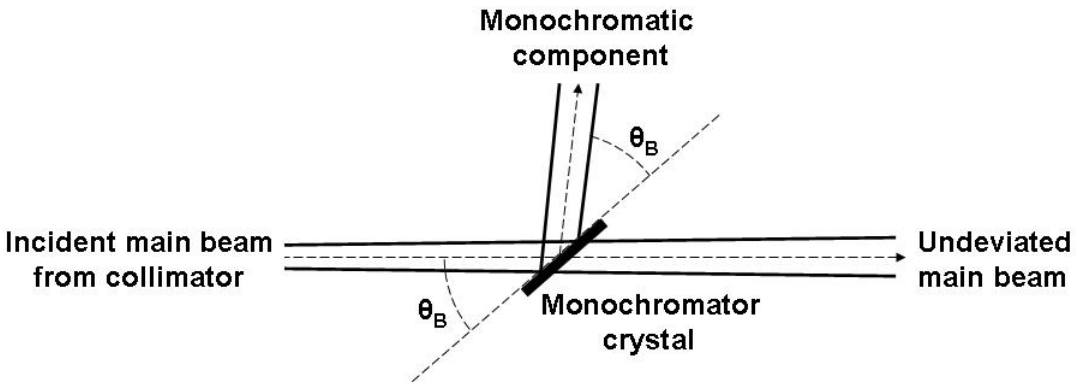

Figure 2.9: Representation of Bragg diffraction at a nuclear reactor beamport.

Neutrons must enter the diffracting material to be diffracted by the crystal planes. When the neutron enters the material there is a probability that it will be absorbed before being scattered. If the neutron is not absorbed and undergoes diffraction off an inner crystal plane, there is a probability that the scattered neutron will get re-diffracted by any crystal plane it must pass through before leaving the crystal as shown in Figure 2.10. The more time a neutron is in the crystal, the greater chance there is for the neutron to be absorbed and not contribute to the refracted neutron intensity [23-26,29].

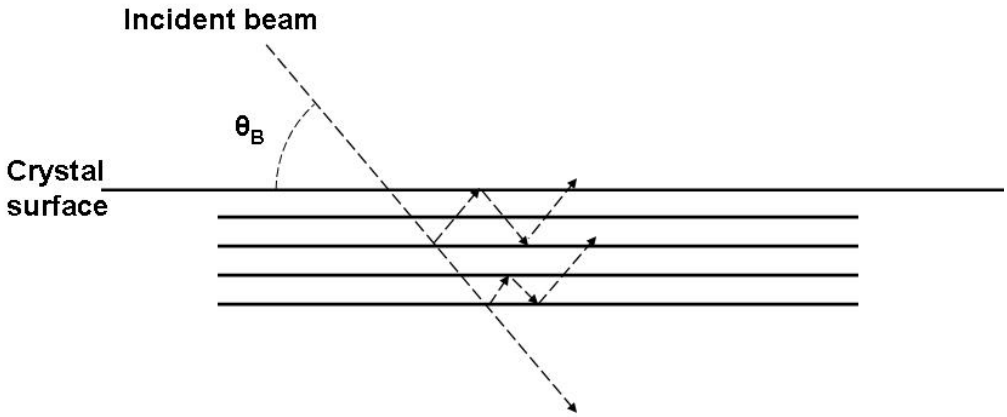

Figure 2.10: Neutron diffraction and re-diffraction from a perfect crystal.

A crystal material with a perfect lattice structure will allow more neutrons to be re-diffracted and absorbed within the crystal than a crystal that does not have a perfect crystal structure. A widely used choice for a non-perfect diffraction material is an ideally *imperfect* mosaic crystal. For a crystal to be described as having a mosaic, it must

be made up of many small mis-oriented perfect crystallites (Figure 2.11). For a crystal to be described as being ideally imperfect, the absorption of the diffracted neutron beam by the individual lattice planes must be negligible. The reflected intensity of an ideally imperfect mosaic crystal is high as compared to a flat perfect crystal in which the absorption of the neutron beam is great due to the perfect crystal structure [23-26,29].

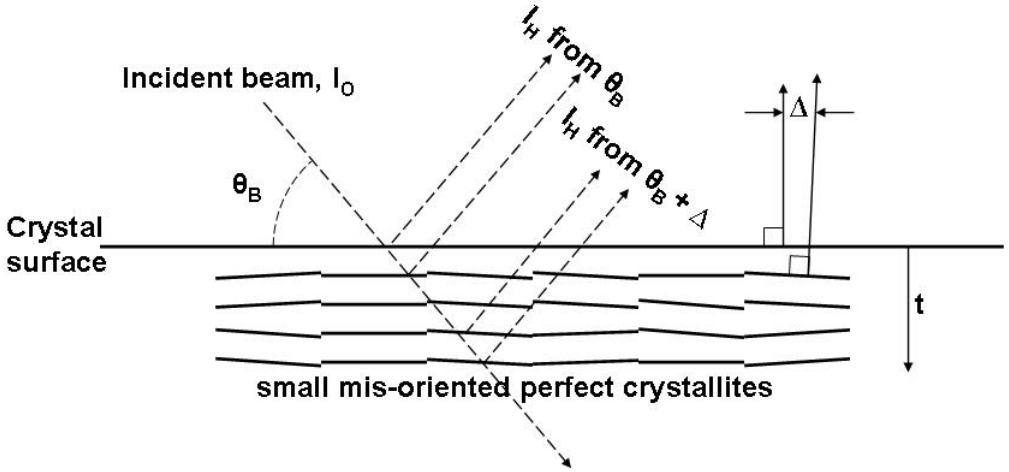

Figure 2.11: Representation of an ideally imperfect mosaic crystal.

The kinematic theory of reflectivity can be used to calculate the reflected intensity of a diffracted neutron beam [29]. To calculate this intensity one must consider the internal absorption, internal diffraction and reflection of a neutron beam across a crystal thickness *dt*. The absorption cross section and Bragg diffraction cross section along with the Bragg angle are necessary to determine the reflected intensity of the diffracted neutron beam. The differential equations for the incident and diffracted beam intensities (I_o and I_H, respectively) of an ideally imperfect crystal are given by [29],

$$dI_O(t) = -\left(\frac{\Sigma_a I_O}{\sin\theta_B}\right)dt \;-\; I_O \Sigma_B\, dt + \;\; I_H \Sigma_B\, dt\,, \tag{2.18}$$

$$dI_H(t) = \left(\frac{\Sigma_a I_H}{\sin\theta_B}\right)dt \;+\; I_H \Sigma_B\, dt \;-\; I_O \Sigma_B\, dt\,, \tag{2.19}$$

where t is the distance below the surface (as shown in Figure 2.11), $\sum_B$ is the macroscopic Bragg diffraction cross section, $\sum_a$ is the macroscopic absorption cross section and θ_B is the Bragg angle (as shown in Figure 2.11). The first terms on the right

side of Eqs. (2.18)-(2.19) represent the intensity decrease due to absorption and diffraction, whereas the third term is the intensity increase due to reflection of the diffracted and incident neutron beam. The macroscopic Bragg diffraction cross section $\sum_B$ is dependent on the Bragg angle, the angular deviation Δ between the plane normal of the diffracting planes within a given crystallite and the surface normal (as shown in Figure 2.11) [29].

To calculate the Bragg diffraction cross section one must first consider the structure factor $F(hkl)$ for a single unit cell of the crystal, a mathematical description of how a crystal scatters incident radiation and accounts for scattering due to all positions of atoms in the unit cell. A Fourier series is used to represent the periodic distribution function of the crystal lattice. The summation is taken over each atomic postition in the unit cell described by the Miller indices (hkl) of the diffracting plane, and their respective coherent scattering lengths. The structure factor is given by [29],

$$F(hkl) = \sum_s b_s \, exp\left[2\pi i\left(\frac{h\,x_s}{a} + \frac{k\,y_s}{b} + \frac{l\,z_s}{c}\right)\right], \tag{2.20}$$

where b_s is the coherent scattering length of the s-th atom, x_s, y_s, and z_s are the coordinates of the s-th atom, and a, b, and c are the dimensions of the cell. For crystalline materials with a hexagonal structure four Miller indicies ($hkil$) can be used to describe the diffracting planes. However, the i index is a redundant index ($i = -h - k$); in most literature regarding neutron diffraction a hexagonal structure is only defined by the 3 necessary Miller indicies. The structure factor is an important quantity for diffraction because it can be used to determine if the presence of harmonics n is not available due to the structure of the diffraction crystal. For example, a material with a diamond structure like silicon will only allow diffraction from the (hhh) planes when h is odd because the structure factor for the even (hhh) planes is zero and will not allow diffraction [25].

The structure factor is then used to calculate the diffracting intensity of a very small perfect crystal also known as the Q value [25]. The Q value is a crystallographic quantity of the diffracting crystal that is dependent on the crystal position, neutron wavelength, and how the incident radiation scatters inside the unit cell. The Q value is a linear reflectivity coefficient with units of cm^{-1} and can be written specifically in terms of the neutron wavelength λ or using Braggs law (Eq. 2.17) the Q value can be defined by

the crystal plane spacing d and the Bragg diffraction angle θ_B (as shown in Figure 2.11) by [29],

$$Q = \frac{|F(hkl)|^2 \lambda^3 N_C^2}{\sin 2\theta_B} = \frac{8|F(hkl)|^2 d^3 \sin^3 \theta_B N_C^2}{\sin 2\theta_B}, \tag{2.21}$$

where $F(hkl)$ is the structure factor for the (hkl) reflection, and N_C is the number of unit cells per cm^3.

However, the crystal is not perfect; hence the angular deviation between slightly mis-oriented crystallites are accounted for by assigning a distribution function to the Bragg diffraction cross section. The angular deviation distribution of the individual diffracting planes is assumed to follow a normalized Gaussian distribution function $W(\Delta)$ of width η; hence the Bragg diffraction cross section is defined in Eq. (2.22) given by [29],

$$\Sigma_B = \frac{Q}{\gamma} W(\Delta) = \frac{Q}{\gamma} \frac{1}{\eta\sqrt{2\pi}} \exp\left(-\frac{\Delta^2}{2\eta^2}\right), \tag{2.22}$$

where $\gamma = \sin\theta_B$, η is the mosaic standard deviation and Δ is the angular deviation between the plane normal of the diffracting planes within a given crystallite and the surface normal. All Δ angle's about the normal plane can be considered in the calculation, however the Bragg diffraction cross section typically nears zero for a $|\Delta|$ greater then 0.05 radians; hence the calculation only needs to be evaluated between $\Delta = \pm 0.05$ radians.

Equations (2.18) and (2.19) can then be evaluated to determine the incident and diffracted beam intensities. The appropriate boundary conditions used to simultaneously solve the first order differential equations, Eqs. (2.18) and (2.19), are that I_o at $t = 0$ is known and I_H at $t = T_o$ is zero, where T_o is the crystal thickness. The ratio of the incident I_o and diffracted I_H beam intensities determine the diffraction intensity of the crystal. The ratio represents the intensities at the surface ($t = 0$ from Figure 2.11) and is given by [29],

$$\frac{I_H(0)}{I_O(0)} = \frac{\Sigma_B + \frac{\Sigma_a}{\gamma} - U}{\Sigma_B} - \frac{U\left[\Sigma_B + \frac{\Sigma_a}{\gamma} - U\right] exp(-UT_o)}{\Sigma_B\left[\left(\Sigma_B + \frac{\Sigma_a}{\gamma}\right) sinh\, UT_o + U\, cosh\, UT_o\right]}, \tag{2.23}$$

where the quantity U is defined as [29],

$$U = \sqrt{\left(\Sigma_B + \frac{\Sigma_a}{\gamma}\right)^2 - \Sigma_B^2} \ . \tag{2.24}$$

Thus, the diffraction intensity R^{θ} of the diffracting crystal is determined by integrating over the angular deviation Δ (from the Bragg diffraction cross section) of the individual diffracting planes at the surface of the crystal (t= 0) [29].

$$R^{\theta} = \int \frac{I_H(0)}{I_O(0)} d\Delta \ , \tag{2.25}$$

Inserting Eq. (2.23) into Eq. (2.25) yields,

$$R^{\theta} = \int \frac{\Sigma_B + \frac{\Sigma_a}{\gamma} - U}{\Sigma_B} - \frac{U\left[\Sigma_B + \frac{\Sigma_a}{\gamma} - U\right] exp\left(-UT_o\right)}{\Sigma_B\left[\left(\Sigma_B + \frac{\Sigma_a}{\gamma}\right) sinh\, UT_o + U\, cosh\, UT_o\right]} d\Delta \ . \tag{2.26}$$

The evaluation of Eq. (2.26) is best performed using numerical integration as the exact analytical solution does not exist [23,25,29]. The numerical integration was performed in an Excel spreadsheet for various Δ's [29].

2.2.2 Pyrolytic Graphite

A nearly ideal material for an ideally imperfect mosaic crystal monochromator in a diffraction system is pyrolytic (or oriented) graphite (PG). Pyrolytic graphite has a hexagonal, layered structure and is produced as a quasi-single crystal in which the long-range ordering is only two dimensional. The (*00l*) planes when *l* is even are used for diffraction because, by comparison, all other (*hkl*) planes are randomly aligned. A zero structure factor for the odd (*00l*) reflection means diffraction from the odd (*001*) plane is not possible [6]. The reflectivity of PG is four to ten times higher then other popular crystal monochromators [25]. The properties of PG used to determine the reflectivity are given in Table 2.3.

Table 2.3: Selected properties of Pyrolytic Graphite (PG) [29,33,34].

Property	Value
Diffraction planes (hkl)	(002)
Mosaic FWHM	1.3°
Mosaic standard deviation, η	0.0097 radians
PG lattice constants	a = 2.4612 Å; c = 6.7079 Å
$\|F(002)\|^2$	7.08×10^{-24} cm^2
Reciprocal cell volume, N_c	2.84×10^{22} cm^{-3}
Crysal thickness, T_0	0.3 cm
Macroscopic absorption cross section, Σ_a	4.00×10^{-4} cm^{-1}

The properties of pyrolytic graphite from Table 2.3 in conjunction with Eq. (2.23)-(2.24) are used to plot the integrand of Eq. (2.26) as a function of Δ, the angular deviation between the plane normal of the diffracting planes within a given crystallite and the surface normal, for various Bragg angles (θ_B = 5, 10, 20, 40, 60, and 80) as shown in Figure 2.12.

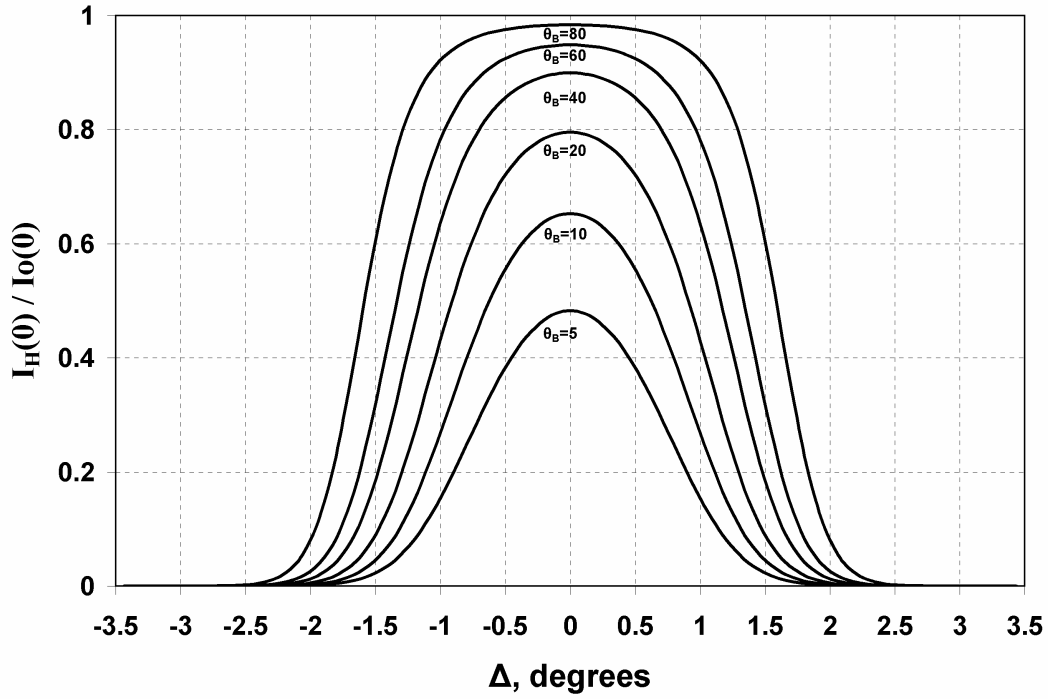

Figure 2.12: Plot of the first order reflection of the (002) plane of 1.3 FWHM pyrolytic graphite as calculated using Eq. (2.26) for various Bragg angles.

The calculation of the diffracting intensity only needed to be carried out between $|\Delta| = 0.05$ radians (2.86 degrees) as the response after these points is near zero. Integrating under the curves of Figure 2.12 yields the diffraction intensity for a given Bragg angle. The diffraction intensity for the first, second, and third order reflections is plotted against various Bragg angles as evaluated using Eq. (2.26) (Figure 2.13) [29]. The plot indicates where higher order contamination is most prevalent to the primary diffracting plane.

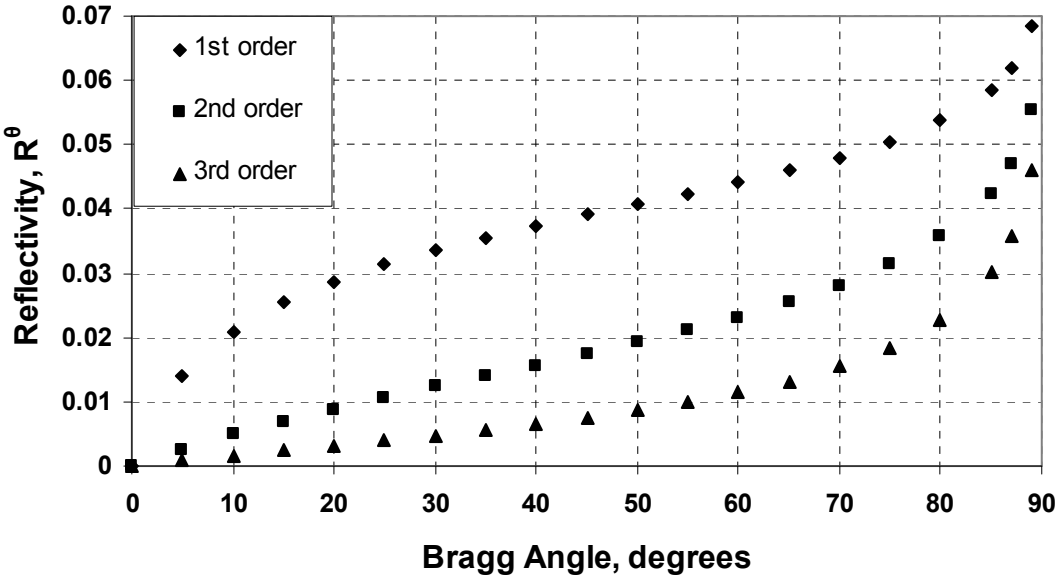

Figure 2.13: Plot of the diffraction intensity for the first, second, and third order reflections using the (002) plane of 1.3 FWHM pyrolytic graphite as a function of Bragg angle.

The diffraction intensity as a function of diffracted neutron energy is another important concept. Bragg's law (Eq. 2.17) can be used to determine the wavelength of the neutron that is diffracted for a specific Bragg angle. After the wavelength is determined, Eq. (2.15) can be used to find the corresponding energy. The (002) planes in PG have a *d* spacing of 3.35 Å, so the diffracted neutron energy can be expressed exclusively for (002) PG as a function the Bragg angle as shown in Eq. (2.27),

$$E_B(eV) = 1.818\ x\ 10^{-3}\ \frac{1}{\sin^2\theta_B}\ . \qquad (2.27)$$

CHAPTER 3 - Detector Construction

The 5x5 2-D neutron detection array was designed and built in the KSU SMART Lab to use as a neutron beam monitor. The thin film semiconductors are fabricated from high resistivity n-type silicon wafers. The wafers are put through various processes in the SMART Lab facilities to yield a semiconductor detector array. After the detector array is made it is then installed onto an amplifier electronics board and connected to a read out sytem with control and interpretation software (LabVIEW) to produce the final operating beamport monitor. The final beamport monitor was checked for uniformity in a neutron beam and each pixel calibrated appropriately [20]. The following sections outline this construction, testing, and characterization process.

3.1 Design and Fabrication

The size of the 5x5 2-D detector array was designed such that the active area of each pixel is approximately 0.25 cm^2 for easy conversion to standard units. A pixel pitch of 5.1 millimeters was needed to allow for the signal output traces. Placing the output trace bond pads along the perimeter of the array yielded an overall area of 8.53 cm^2. The general dimensions are given in Figure 3.1.

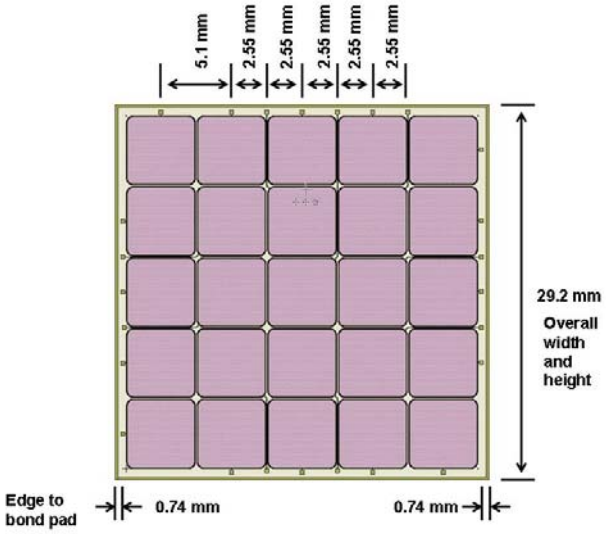

Figure 3.1: Layout of the 5x5 2-D detector array with 25 ^{6}LiF detectors [20].

The semiconductor material and properties chosen for the devices were float-zone, single-side-polished, >10kΩ-cm, n-type silicon wafers 76 mm in diameter and approximately 400 μm thick. Batch processing of wafers was performed for better production efficiency and higher throughput. The wafers were first put through a cleaning process to remove surface impurities. The cleaning process starts by dipping the wafers for 10 minutes in a solution of piranha etch (1:1:1, H_2O:H_2SO_4:H_2O_2) to remove organic residues. The piranha etch solution was heated on a hotplate to 375°C. The wafers were then agitated vigorously for 1 to 2 minutes in the piranha solution to remove bubbles from the wafer surfaces. Once the piranha etch was complete, the wafers were thoroughly rinsed using a dual sided deionized (DI) water cascade for 30 seconds per side. Next the wafers were placed in a buffered oxide etch (BOE) solution for 20 seconds to remove thin films of silicon dioxide (SiO_2) or silicon nitride (Si_3N_4) from the wafer surface. After the BOE etch, the wafers were thoroughly rinsed using the DI water cascade for 20 seconds per side.

A solution of BakerClean (25:5:1, H_2O:BakerClean:H_2O_2) was then used to remove metal contaminants and other particles from the wafer surface. The BakerClean solution was heated to 310°C on a hotplate, and the wafers were dipped in the solution for 10 minutes. After the BakerClean dip, the wafers were thoroughly rinsed using the DI water cascade for 30 seconds per side followed by another 15 second BOE etch to remove any native oxide layers from the surface. Once the final BOE etch was complete, the wafers were thoroughly rinsed in the DI water cascade for 30 seconds per side. As a final step to the cleaning process, the wafers were loaded into a spin-rinse dryer for a final DI rinse and were spun until dry. The wafer cleaning was then complete and the wafer surface was free of surface impurities, as indicated by inspection.

After removal from the spin-rinse dryer, the wafers were loaded onto a quartz wafer boat that allows the wafers to be inserted into a three-zone horizontal tube furnace with a four-inch quartz liner to grow a layer of thermal SiO_2 on the wafer surface. A SiO_2 layer forms a base for a mask pattern to be etched into the wafer for further processes. The three-zones for the tube furnace were set to temperatures of 800°C-700°C-600°C, and dry nitrogen was purged through the furnace for 30 minutes until all zones were stabilized. The wafer boat was pushed into the furnace at 0.1 inches per

second to avoid introducing a thermal shock to the wafers. After the wafer boat was located in the center of the heat distribution, the furnace zone temperatures were raised to 1172°C-1185°C-1171°C, with the dry nitrogen still on. Next, the dry nitrogen was turned off and ultra high purity dry oxygen was turned on and allowed to flow through the tube at 1 liter per minute (lpm) for 5 minutes to grow a dry oxide layer on the wafer surface. A faster growing wet oxide was grown next by flowing the dry oxygen through a heated bubbler at 0.6 liters per minute for 2.5 hours. After the wet oxidation was complete, the furnace zones were turned off (set to 0°C-0°C-0°C) and a dry oxide was grown for 1 hour for a better final oxide surface finish. After the dry oxidation was complete the dry nitrogen was again turned on. The wafers were removed from the furnace and allowed to cool for the next processing step.

Photolithography was needed to produce a protective mask during various processing steps. Photoresist is a light sensitive polymer that is the basis for photolithography. When exposed to light, the photoresist will become chemically altered. If a mask is placed between the photoresist and the light source, the photoresist will take on the image of the mask and a pattern will be developed in the photoresist. The wafers were first dehydrated by placing them on a hot plate at 150°C for 3 minutes. Next, the wafer surface was primed with hexamethyl disilane (HMDS) to promote photoresist adhesion. HMDS was applied with a wafer spinner to achieve a uniform thickness. The wafer was placed on the spinner and carefully blown with nitrogen to remove any particulates from the surface. The HMDS was applied with an eyedropper, and the wafer was spun for 10 seconds at 3000 rpm. After the spin cycle was complete, a final post-bake was performed on a hot plate at 100°C as a final step to promote adhesion. The wafer was returned to the spinner and again blown with nitrogen. The wafer was now ready to have photoresist applied to produce a pattern for dopant diffusion windows.

The photoresist used was AZ nLof 2070, and was applied with an eyedropper. The wafer was spun at 3000 rpm for 30 seconds achieve a uniform surface coating of approximately 5 μm. The wafer was then "soft-baked" on a hot plate set at 100°C for 4 minutes to evaporate the solvent in the photoresist. It was learned that after baking it was best to wait an additional 15 minutes before further processing steps to prevent the wafer

from sticking to the mask aligner. The wafer was then loaded onto a mask aligner and after alignment was exposed for 15 seconds. After the exposure, the wafer was removed from the mask aligner and "hard-baked" on a hot plate set at 115 °C for 2 minutes to crosslink the photoresist polymer chains and harden the photoresist. The wafer was allowed to cool for 20 minutes before the pattern was developed. Development of the pattern was performed by placing the wafer in MIF 300 developer for as long as required to resolve the pattern, typically 3 minutes. A final rinse was performed in the DI water cascade for 1 minute per side. The wafer was then ready to have the SiO_2 removed from the openings in the photoresist, hence allowing for diffusion through those openings. The diffusion windows were needed to create an "active area" for the ionizing radiation to be detected in. The wafers were placed in a solution of BOE for 12-14 minutes to remove the exposed SiO_2 layer. The remaining photoresist was removed using a photoresist solvent solution (KWIK-strip) because photoresist is not compatible with the high temperatures required for diffusion. The KWIK-strip solution was heated to 190°C on a hot plate prior to use. The wafers were dipped in the solution for 15 minutes and afterwards rinsed in 2-propanol until clean.

The surface of the wafer was cleaned again to remove surface impurities by performing another wafer clean (piranha /BakerClean/BOE) as previously discussed. The wafers were placed with boron diffusion sources on each side into a solid source boat and loaded into the boron p-type diffusion furnace (similar size as the oxidation furnace) at 0.1 inches per second. The zones in the diffusion furnace were previously set to 800°C-700°C-600°C and dry pure oxygen was purged through the tube at 1 lpm. The furnace temperatures were increased to 830°C-830°C-830°C over a period of 30 minutes. The furnace was stabilized at these temperatures for 30 additional minutes before being raised to 950°C-950°C-950°C over a period of 30 minutes. After the furnace reached the final temperature, H_2 was purged into the tube for 2 minutes at 1 lpm. Next, the dry O_2 and H_2 were turned off and N_2 was turned on at 1 lpm and maintained for 3 hours. After the 3 hour diffusion was complete, the furnace temperate can be lowered to 400°C-400°C-400°C over the period of 1 hour before the wafers were removed from the furnace.

The wafers were removed from the diffusion furnace and dipped in BOE for 5 minutes to remove the SiO_2 layer that grew on the surface as a result of the diffusion

process. In addition to the SiO_2 layer, the diffusion process leaves a thin nitride layer on the surface. The nitride layer can not be easily removed on its own, so an oxide that penetrates the nitride layer was grown. The wafers were again placed in the oxidation furnace using the process described above and a low-temperature-oxide was grown. A dry oxide was grown for 30 minutes at 1 lpm. Unlike the earlier oxidation step, no wet oxide was grown and the furnace temperatures were held at 830°C-830°C-830°C. After the dry oxidation was complete, the gas was switched to N_2 and the furnace was turned off (set to 0°C-0°C-0°C). The nitride/oxide layer was then removed from the wafer surface using a 2 minute BOE dip.

Photoresist was again applied to the wafers to form a pattern for contact and trace metallization. The procedure used to apply the photoresist for the metal contacts was the same as used for the diffusion windows, but with one major difference; the exposure time was reduced from 15 seconds to 3 seconds to cause undercutting of the photoresist during development to promote metal "liftoff". After the photoresist pattern was developed, the wafers were placed in BOE for 2 minutes to remove the native oxide layer on the wafer surface where the signal traces and contacts were to be deposited.

The signal traces and contacts were deposited on the wafer surface with physical vapor deposition using an electron beam evaporator. The deposition coats the entire front surface of the wafers, including the photoresist, with metal. A thin layer of titanium (500 Å) was first applied to the wafer surface to improve the interface between the aluminum and the silicon. A thicker layer of aluminum (4500 Å) was applied next as for the signal trace. The residual material atop the photoresist was removed by placing the wafers in a heated solution of KWIK-strip, which removes the photoresist and lifts off the excess metal. The wafers were kept in the KWIK-strip until the excess metal was completely removed, typically 2 hours. The metal-contact-deposition process was repeated for the back side of the wafer; however no selective photolithography was required because the entire back side of the wafer was a single metal contact. The front side of the wafer was coated with a protective layer of photoresist. The protective layer shields the front side oxide layer when the wafer was placed in the BOE dip for 2 minutes, as required to remove the native oxide layer from the back side before metal deposition.

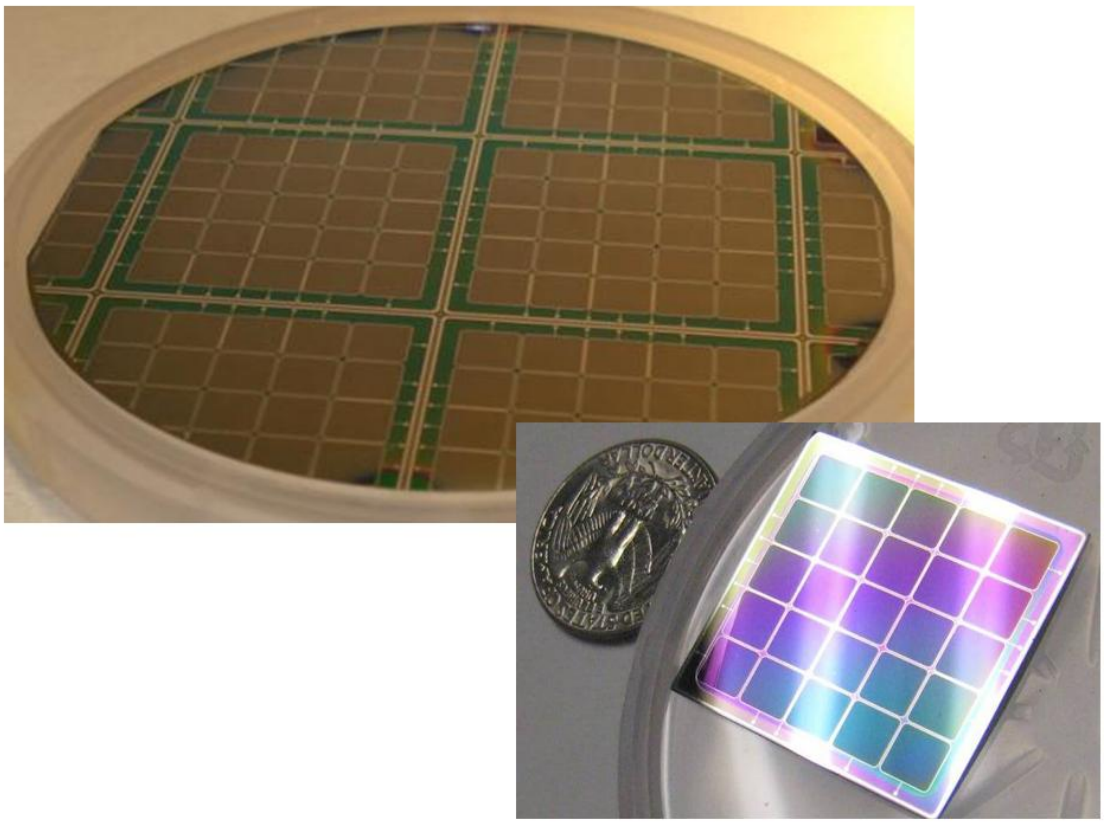

Figure 3.2: Two 2-D arrays on wafer (top) and cut detection array (bottom).

The detection arrays, two positioned on each wafer as shown in Figure 3.2, were separated from the wafer by dicing. A diamond-tipped wheel dicing saw was used to cut the wafer substrate. During dicing, the protective layer of photoresist was kept on the front side of the wafer. After the dicing was finished, the photoresist was removed using a heated solution of KWIK-strip for 15 minutes. Next, the detection arrays were placed back into the electron beam evaporator for deposition of the neutron sensitive material on the diffused regions. The detection arrays were mounted using a mask that covers the output traces on the perimeter of the array. A thin layer of aluminum (500 Å) was first applied to the array to promote surface adhesion of the ^{6}LiF. Next, a 1μm (10,000 Å) thick neutron sensitive coating of ^{6}LiF was applied that yields approximately 0.54% thermal neutron detection efficiency [10]. Finally, the detection arrays were coated with a conformal protective coating (Humiseal) with an aerosol to prevent peeling of the ^{6}LiF coating. The detection arrays were then ready to be mounted on the amplifier board.

3.2 Electronics and LabVIEW

The amplifier board needed to read the signals produced by the 2-D detection array was designed and built at the KSU Electronics Design Laboratory (EDL) (Figure 3.3). The schematics, board layout, and general operating characteristics are in Appendix B. The amplifier board consists of 25 identical amplifier circuits each with an adjustable threshold voltage that allows for individual adjustments of each channel to compensate for different noise levels between channels. The overall threshold voltage for the entire detection array can also be changed with a single potentiometer. The board was also designed to allow a voltage bias to be applied across the array to aid in signal generation. The option to allow for external biasing was needed if the built-in potential of the detector was not enough to produce a measurable signal. The center of the amplifier board was cutout at the detection array location so that the neutron beam will not interact (scatter or activate) with the amplifier board. The board was powered by ±12 volts DC.

The detection array was applied to the amplifier board using silver solder between the board and single back side contact of the array. The front side contacts were wire bonded to their respective traces. The entire detector board was placed in an oven at 100°C for 60 minutes to cure the solder. After the curing process was complete, an epoxy was applied around the wire bonds to protect the fragile wires from damage.

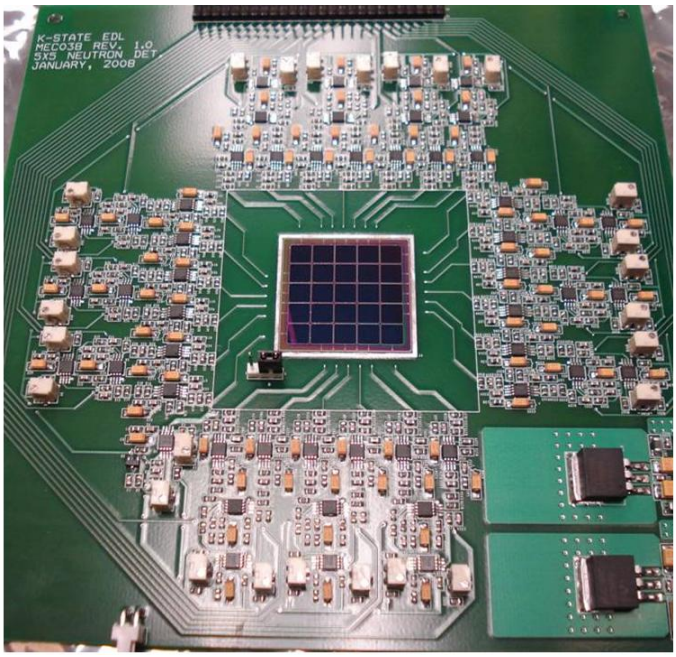

Figure 3.3: Amplifier board with 2-D detection array mounted in the center.

The detector board was then mounted into a light tight aluminum box with cutouts that allow twisted pair ribbon cables and the power connections to pass through. The output of the detector board was wired to a LabVIEW connector block that connected to a LabVIEW field-programmable gate array (FPGA). The FPGA module was configured to continuously count each signal and output to a LabVIEW virtual instrument (VI) that displays the data in 2-D arrays. The data was shown on three 5x5 intensity graphs with accompanying 5x5 matrices where each individual block image represents a pixel on the detector.

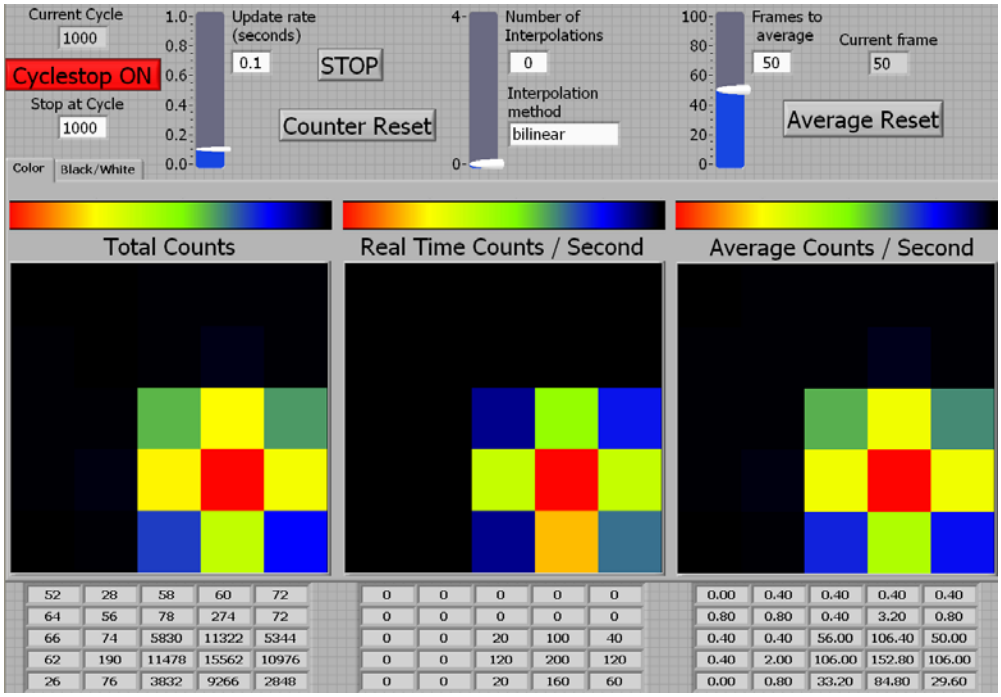

Figure 3.4: LabVIEW VI displaying neutron beam image; color with no interpolation.

The 3 graphs indicate the total counts, the real time counts per second, and the average counts per second as shown in Figure 3.4. The averaging time interval is user selected. The graphs have user adjustable interpolation routines and grey or color scaling for easier interpretation. These routines include nearest neighbor interpolation, bilinear interpolation, bicubic interpolation, and bicubic spline interpolation (Appendix A) [25]. To adjust for any non-uniform response from the detector pixels, scaling factors can be

assigned to each pixel channel and the resulting scaled output will be shown in the VI. After appropriate scaling factors were assigned to each pixel, the final detector configuration can be used to image the diffracted neutron beam at the detector test station.

3.3 Detector Array Testing

The detector array was tested at the detector test facility described in chapter 4. The detector array was attached to the test fixture with two linear stages so that each pixel could be repeatedly positioned in the neutron beam (Figures 3.5 and 4.28). The detector array was first setup such that the center pixel was aligned with the center of the diffracted neutron beam. A measurement at this position was taken and recorded. The detector was then moved 5.1 millimeters horizontally so the neighboring pixel was now in the center of the neutron beam and another measurement was taken and recorded. This process was repeated, horizontally and vertically, until the response for each pixel was determined. The value for each pixel was then input into the VI and appropriate scaling factors were assigned to each pixel so that the observed response across the detector was uniform.

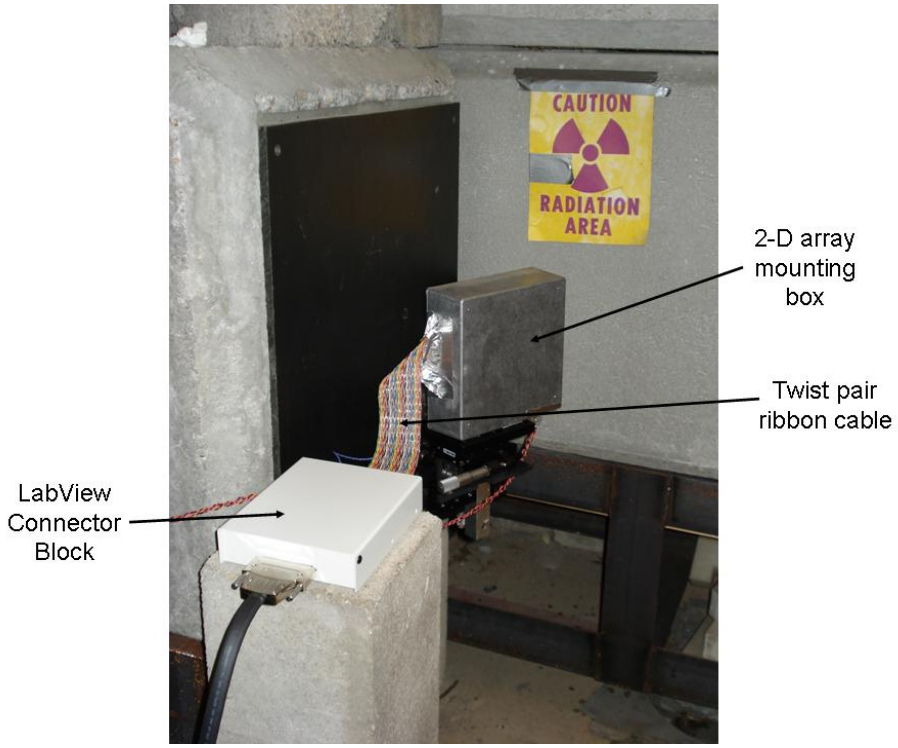

Figure 3.5: 2-D neutron detection array installed at the detector test facility.

CHAPTER 4 - Detector Test Station Construction

A neutron detector test facility was installed at the northwest beamport (NWBP) at the KSU TRIGA Mark II nuclear reactor. The installation requires several specialized pieces of equipment. Furthermore, many steps were needed to insure all equipment was properly installed, aligned and calibrated for the desired diffracted neutron energy. Once the initial setup is complete, shielding and testing equipment were added so that the diffracted neutron beam could be used to calibrate various neutron detectors. The following sections outline the equipment, the experimental arrangement and calibration.

4.1 Elements of the Detector Test Facility

Numerous elements were needed to install a detector test facility at the NWBP. Starting at the reactor core, the first component is a neutron collimator that is installed in the beamport to narrow the neutron beam to focus the neutrons on the diffracting crystal. The next component is a neutron filter that is installed in the neutron collimator. The filter reduces fast neutron and gamma ray background while still allowing a large number of thermal neutrons to be transmitted. After the filtered neutron beam leaves the collimator, a diffracting crystal, or monochromator, is used to diffract neutrons by Bragg diffraction. The monochromator and a neutron detector are positioned accurately to determine the neutron spectrum. High precision rotational stages are used to rotate the detector and monochromator in the neutron beam. Finally, biological shielding that absorbs radiation is needed to protect experimenters from radiological hazards and to reduce the neutron and gamma-ray background.

4.1.1 Collimator

The beamport opening is approximately 20 centimeters in diameter and will diverge as $1/r^2$ from the core. A collimator is needed to reduce the divergence as well as reduce the radiation flux from the beamport opening and also direct the beam to the target location. The collimator (Figure 4.1) was primarily fabricated from aluminum and concrete. The outer shell is made of 14 centimeter and 19 centimeter outside diameter aluminum tubes. Aluminum spacers concentric between the tubes hold the tubes in alignment. The inner tube allows neutrons from the reactor core to stream though. The

ends of the inner tube were designed to be sealed with thin aluminum windows to allow the chamber to be backfilled with Argon to improve neutron transmission. The space between the outer shell and inner tube is filled with high density self consolidating concrete. The completed collimator was bolted to the beamport housing using a watertight seal between the mounting flange and the beamport opening to prevent reactor pool water leaks in the unlikely event of a beamport rupture.

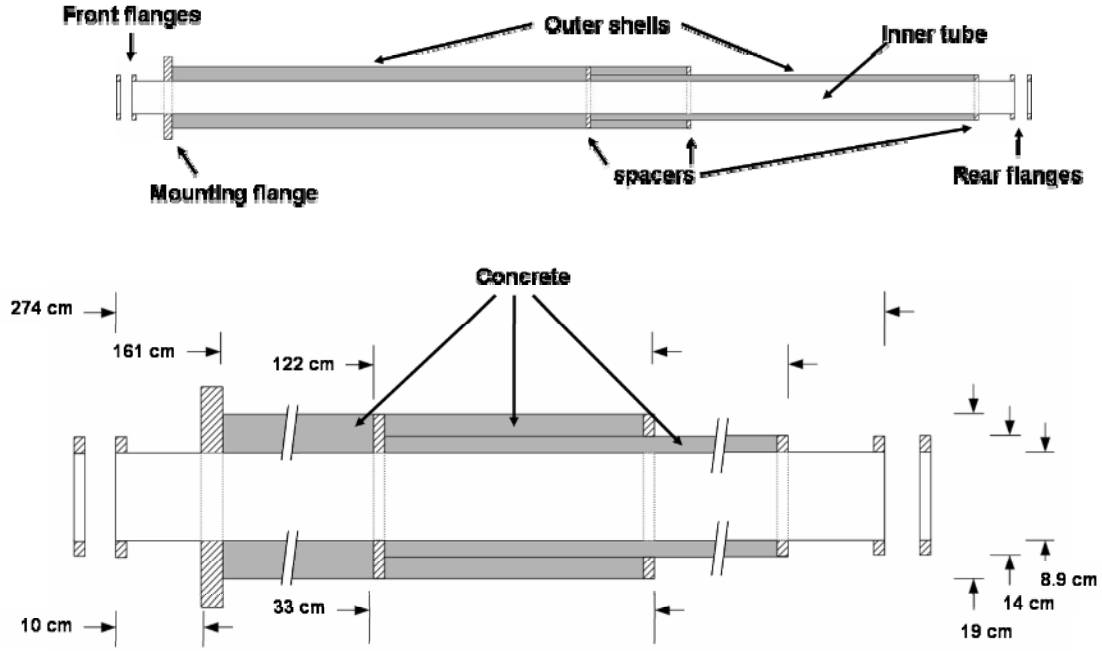

Figure 4.1: Cross-sectional view of 8.9 centimeter collimator installed in the NWBP.

4.1.2 Neutron Filter

A filter was used to improve the effect-to-noise ratio by lowering the fast-neutron and gamma-ray component from the radial beamport. Sapphire was chosen as the filtering material because of the excellent thermal neutron transmission. At neutron energies greater than 1 eV the total neutron cross-section is in the range of a few barns, but at energies less than 1 eV where coherent Bragg scattering is generally disallowed, the effective cross-section is reduced. Also the inelastic scattering cross-section decreases with decreasing neutron energy in sapphire. Experiments by Tennant demonstrate neutron transmission as high as 80%, at room temperature (Figure 4.2) [25]. The filter used is 7.6 centimeter in diameter and 10.2 centimeters long. A piece of 0.635

centimeter thick aluminum tubing was needed to align the sapphire filter in the center of the inner tube of the collimator because of the difference between the ID of the inner tube and the OD of the sapphire as shown in Figure 4.3. The filter is positioned on the reactor side of the collimator.

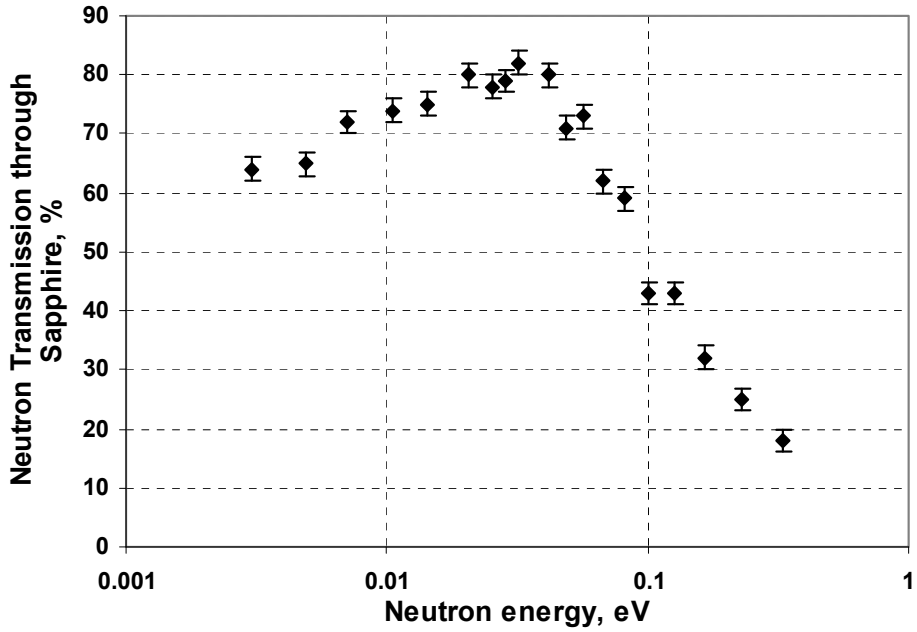

Figure 4.2: Experimental neutron transmission of a 10.2-cm-thick sapphire filter at 300K as a function of neutron energy, Tennant 1988 [25].

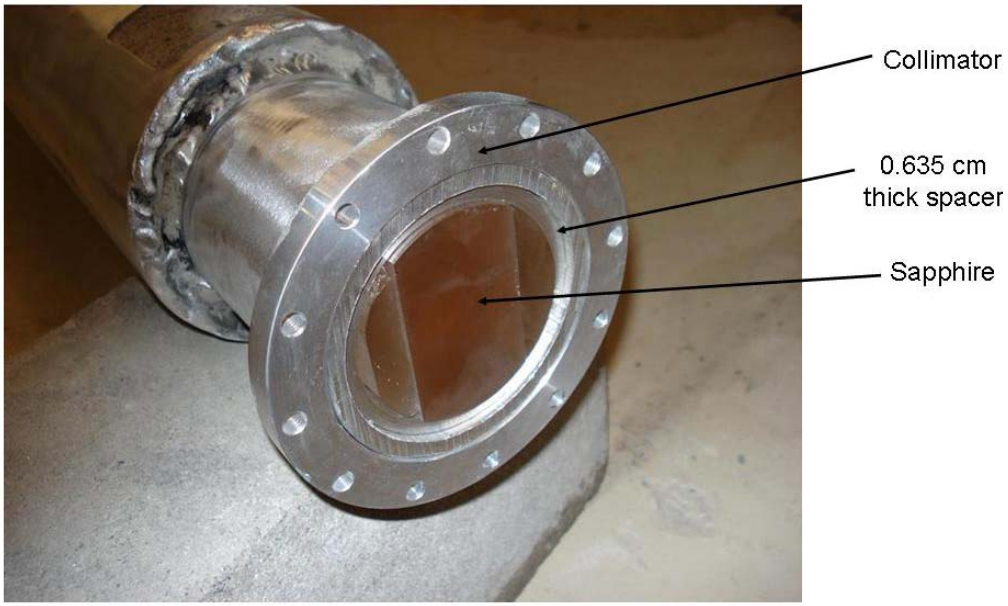

Figure 4.3: Sapphire filter installed in collimator.

4.1.3 Monochromator

A diffracting crystal, or monochromator, with a high neutron reflectivity was needed to produce an intense diffracted neutron beam. Pyrolytic graphite (PG) was utilized because of the large integrated reflectivity and diffraction is only possible from the (00(2n)) crystal planes because the hexagonal crystal structure does not allow other diffractions to occur. The monochromator (Figure 4.4) is composed of PG positioned such that crystal planes with the highest reflectivity, the (002) planes, are the principle diffracting planes. These planes have a spacing of 3.35 Å and a 1.3º FWHM mosaic. The monochromator is comprised of 10 segments of PG each measuring 6.5 cm tall by 1.3 cm wide. The segments are held together with an aluminum block that was machined such that the surface has a radius of curvature of 6.1 meters. The radius of curvature allows more of the diffracted neutron beam to reach the testing location [24].

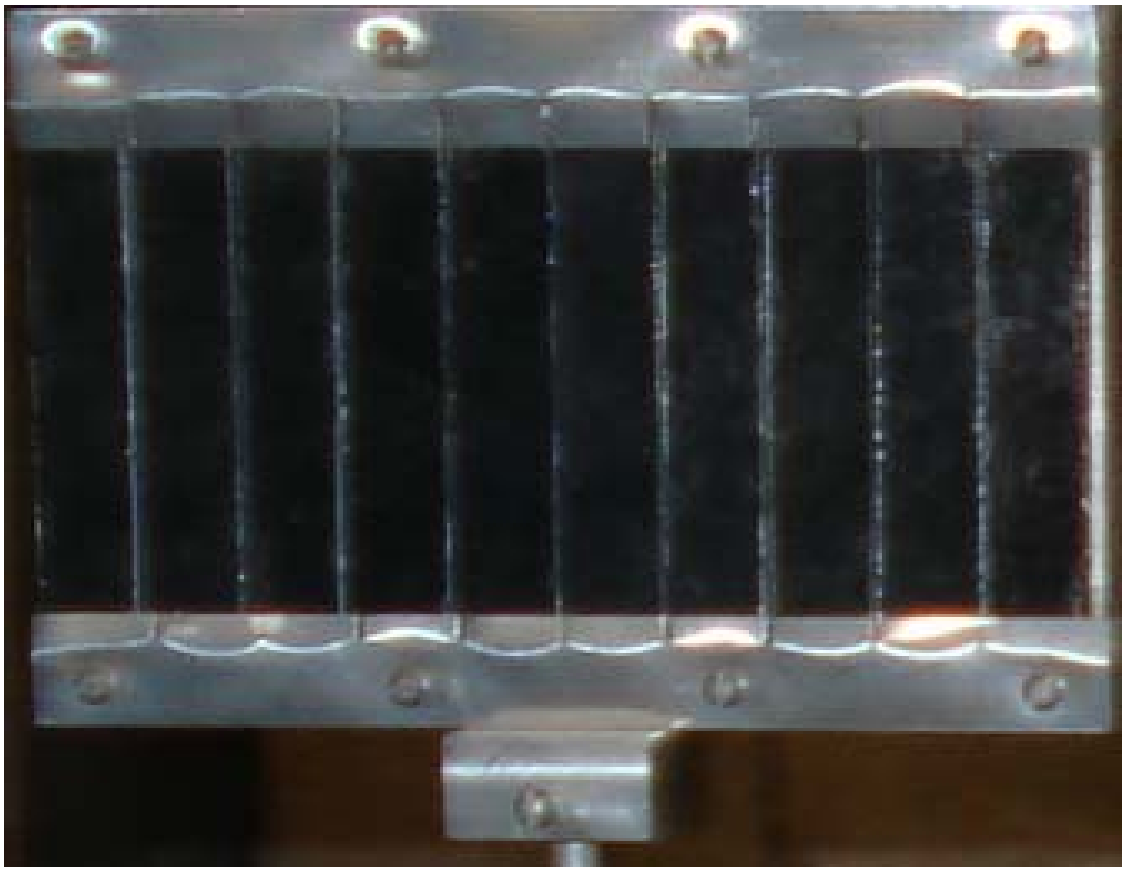

Figure 4.4: Ten segment pyrolytic graphite monochromator and curved aluminum holder.

4.1.4 Neutron Detector

A high efficiency neutron detector with a response that was energy independent was needed to accurately characterize the diffracted neutron beam in a short amount of time. A ^{3}He gas-filled neutron detector was the most suitable choice. The neutron detector used for alignment and calibration is a Reuter Stokes ^{3}He neutron detector (Figure 4.5). The detector has a diameter of 5.08 centimeters, a length of 12.7 centimeters, a manufacturer specified pressure (Appendix C) of 4 atmospheres (60 psia) and is operated at a voltage of 1450 volts. The energy dependent efficiency of the detector was determined by calculating the neutron absorption in the fill gas. The manufacturer pulse height spectrum and operating characteristics are given in Appendix C.

Figure 4.5: Reuter Stokes ^{3}He neutron detector.

The energy dependent thermal neutron detection efficiency of the detector is nearly energy *independent* for energies less than 0.05 eV [29]. However beyond 0.05 eV, the detection efficiency must be taken into account. The cross section of ^{3}He within the energy range of the monochromator has a 1/v dependence. As such, the energy dependent microscopic cross section (Eq. 4.1) can be written as [4],

$$\sigma(E) = \sigma_0 \sqrt{\frac{E_0}{E}}\ , \tag{4.1}$$

where σ_0 is the cross section at some known energy E_0. The ideal gas law (Eq. 4.2) can then be used to calculate the density ρ of the ^{3}He as [32],

$$\rho = \frac{PM}{RT}\ , \tag{4.2}$$

where P is the gas pressure, M is the molar mass, R is the ideal gas constant and T is the temperature. He-3 has a microscopic absorption cross section of 5333 barns at an energy of 0.0253 eV [26]. Equations (4.1)-(4.2) are used to calculate the energy dependent macroscopic cross section $\Sigma(E)$ of a ^{3}He detector pressurized to 4 atmospheres at a temperature of 300K (Eq. 4.3) by [3,6,29, 30,34],

$$\Sigma(E) = 0.083 \frac{1}{\sqrt{E(eV)}} \left[cm^{-1}\right]\ . \tag{4.3}$$

Utilizing the energy dependent result of the ^{3}He macroscopic absorption cross section and the neutron attenuation through the 304-stainless-steel shell [38], the neutron absorption probability of a neutron entering perpendicular to the central axis of a 5.08 cm diameter ^{3}He neutron detector plotted of as a function of incident neutron energy is shown in Figure 4.6.

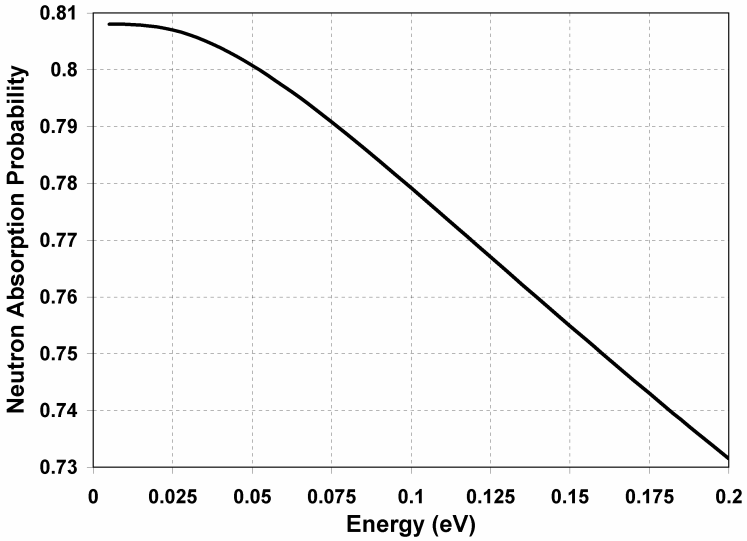

Figure 4.6: Energy dependence of neutron absorption for a 5.08 cm diamter ^{3}He neutron detector pressurized to 4 atm with neutrons moving perpendicular to the central axis of the detector [38].

The detector was acquired as a used instrument and the exact irradiation history was unknown; hence recent work determined the ^{3}He efficiency in a diffracted neutron beam to account for geometric considerations (detector construction and detector position) as well as any detector burnup [38]. The detector was used for studies in small angle neutron scattering at a 1.5 MW research reactor and positioned such that the incident beam had already encountered 3 crystal scatters, so it is suspected that the burnup is likely minimal [33].

4.1.5 Motion Controls

Repeatable positioning of the monochromator and detector is necessary to accurately determine the neutron beamport leakage spectrum. Stages are needed to position the equipment and a control system is need to monitor the equipment. The stage needed for the monochromator can be small in size because it only positions the lightweight monochromator. However, the stage for the detector is larger to allow room for smaller stage to be aligned with the central axis of the larger stage. The larger stage also supports the weight of the detector because it is placed outside of the rotational area of the stage. The stages used to characterize the neutron beam are a 500 mm diameter rotational stage manufactured by Huber for positioning of the neutron detector and a 125 mm diameter rotational stage manufactured by Parker Motion for positioning of the monochromator (Figure 4.7). Both stages have a resolution of 0.001°. The smaller Parker stage is mounted inside the larger Huber stage. The stages are mounted to each other such that the center of the rotational axes are aligned. The stages were placed on a metal table to allow for proper alignment of the monochromator with the center of the neutron beam.

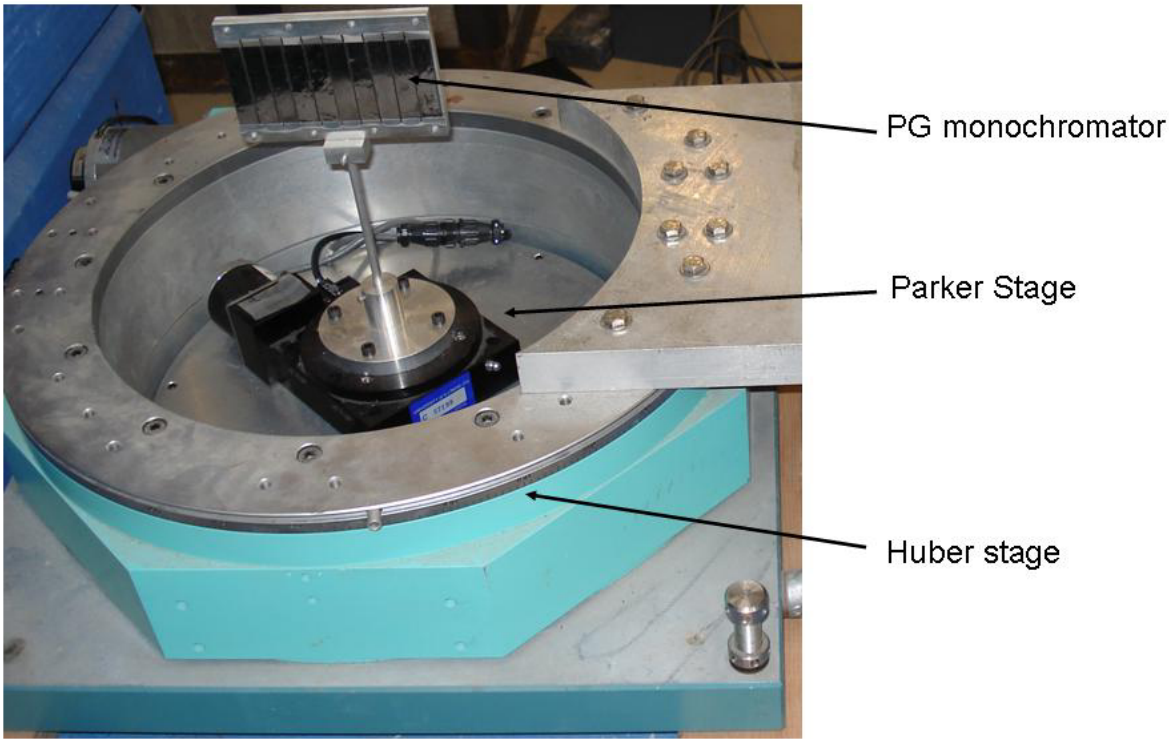

Figure 4.7: Stages used to position monochromator and detector for measuring the neutron leakage spectrum from the NWBP.

The stages' stepper motors are powered by Parker drives. These drives are controlled through a MultiFlex PCI card with programming achieved by LabVIEW virtual instruments (VIs). The VIs (Figure 4.8-9) perform several functions and provide an interface for several pieces of equipment that are needed to characterize the neutron beam. The important functions include positioning of the stages while plotting the detector location and response. The first VI (Figure 4.8) locates the center of the main neutron beam and the center of the diffracted neutron beam. The second VI (Figure 4.9) is used to perform a spectral measurement of the neutron beam from the beamport. Operational notes are provided in Appendix C.

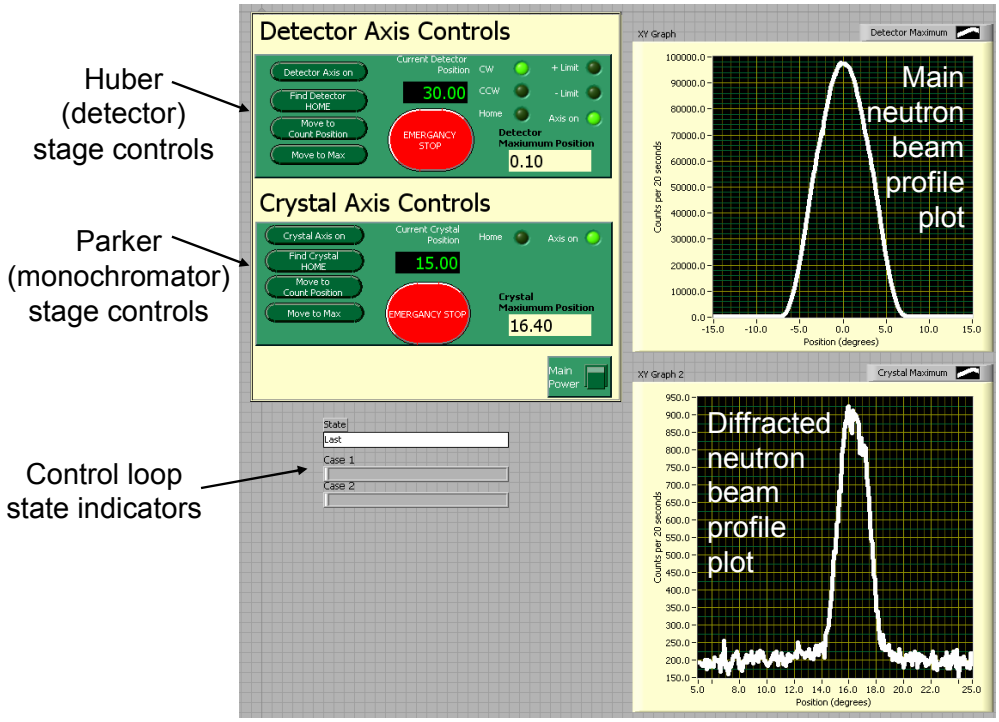

Figure 4.8: LabVIEW VI for aligning the detector and monochromator.

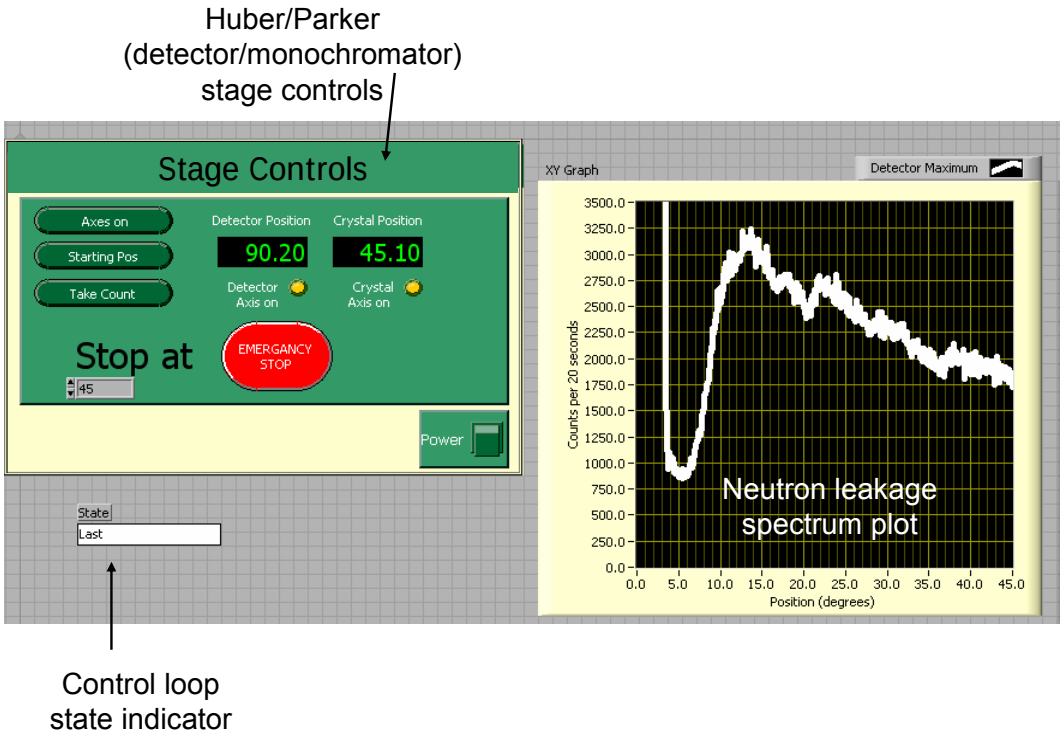

Figure 4.9: LabVIEW VI used for measuring the neutron leakage spectrum from the NWBP.

4.1.6 Shielding

Biological shielding is needed to protect experimenters from the radiological hazards associated with the intense radiation field emanating from the collimator. Concrete was chosen as the primary shielding material because of its low cost, construction ease and high neutron and gamma radiation interaction cross sections. The hydrogen in concrete strongly influences the effectiveness for neutron shielding because the neutrons scatter off hydrogen and quickly loose enough energy to be absorbed in the concrete [22]. Borated polyethylene sheets were also utilized as a neutron shielding material because similar to concrete, they have a high hydrogen content that allows the neutrons to loose energy before being absorbed by the boron. The concrete blocks had to be placed on metal tables to keep overall weight to a minimum so the maximum floor loading of 400 lb/ft^2 was not exceeded. A total of five blocks, which are specially modified roadway construction block barriers; three large blocks 30x30x60 inches (blocks #1-3) (Figure 4.10) and two smaller blocks 16x30x60 inches (blocks #4 and 5) were used. Shielding block #1 was constructed to fit evenly against the reactor wall. Shielding block #2 has a bucket shape formed into the end to act as a beam catcher. The beam catcher was lined with cadmium and borated polyethylene to reduce scattered neutrons. Shielding block #3 has a horizontal slot cut-out that allows the diffracted neutron beam to pass through it. Shielding block #4 was placed over the open space between blocks #1 and #3 to prevent excessive radiation exposure to areas above the shielding; block #5 was placed on top of block #2 for the same purpose (Figure 4.11). One-inch-thick sheets of #210 30% borated polyethylene were stacked above the opening of the collimator keep up-scattered radiation to a minimum [36]. Concrete was not used in this location because the borated polyethylene sheets could span the distance between the blocks and were easily handled compared to concrete blocks.

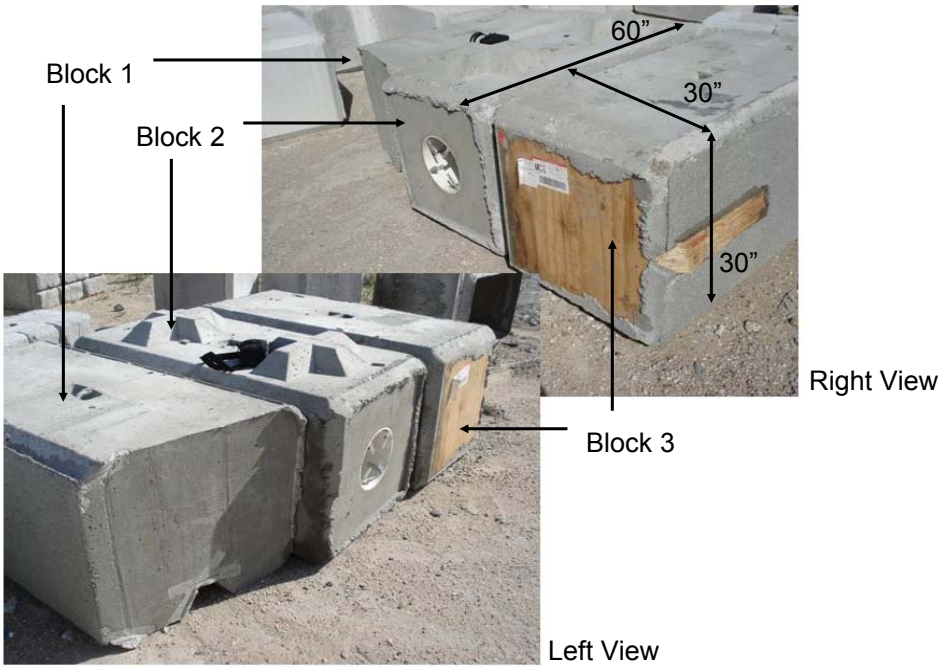

Figure 4.10: Large concrete blocks modified for use as biological shielding; right and left views.

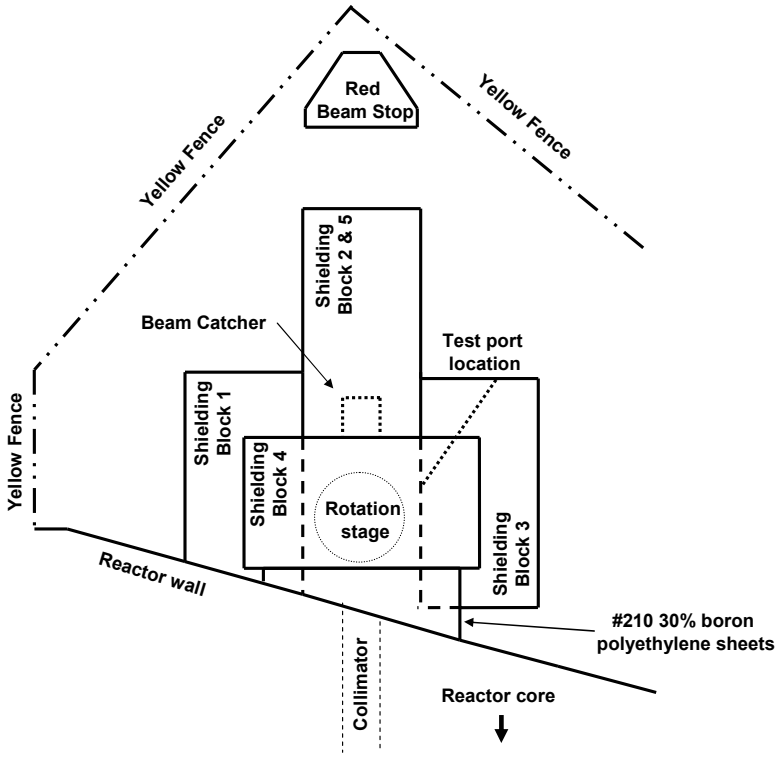

Figure 4.11: Diagram of biological shielding design at the NWBP.

4.2 Initial Setup

Many measurements, alignments and realignments are needed before the diffraction system can be used to test neutron detectors. The process starts with an initial placement of the components with the reactor turned off. After the initial placement is complete the reactor is turned on and measurements are taken that reveal the center of the primary neutron beam and the center of the diffracted neutron beam. Once these procedures are complete, a neutron leakage spectrum of the beamport can be performed. The following section outlines this process. A step by step description of the equipment operation is available in Appendix C.

4.2.1 Initial Alignment of Components

The first step in setting up the equipment involves aligning the central axis of the rotary stages on which the PG monochromator rests with the center of the opening of the collimator, thereby placing the monochromator in the center of the neutron beam (Figure 4.12). With appropriate radiological precautions, a visual alignment is performed with the reactor turned off. The PG monochromator was attached to the Parker 125mm rotational stage and adjusted in both the horizontal and vertical direction while being maintained level to floor. The motion stages are located below the neutron beam so they do not scatter neutrons. After the stages were positioned such that the monochromator could be returned to the proper position in the beam, the monochromator was removed from the Parker stage table. The ^{3}He detector was then used to determine the neutron beam profile by placing it vertically on the Huber 500mm rotational stage. The contribution from diffuse scattered neutrons was minimized by wrapping the detector with cadmium; a 2mm wide vertical slit that ran along the axis of the detector was left to allow the neutrons to enter the detector. The ^{3}He detector was visually positioned in the center of the collimator opening with the cadmium slit facing the beamport . This position is the initial zero-degree position of the detector (Figure 4.12). The visual alignment of the ^{3}He detector is not accurate enough to determine the center of the neutron beam; hence the ^{3}He detector was rotated through the neutron beam to determine the peak location corresponding to the center of the neutron beam.

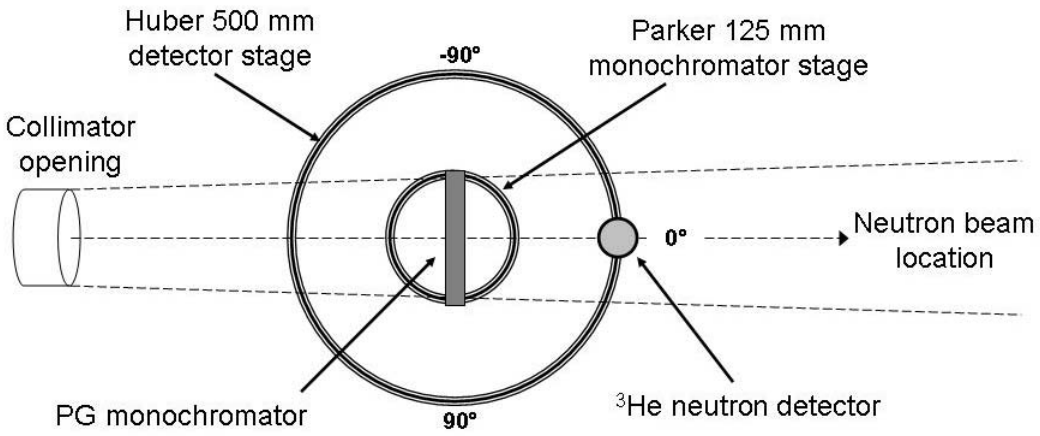

Figure 4.12: Top view of the diffraction configuration indicating position of the detector and monochromator in relation to the neutron beam.

4.2.2 Locating Beam Center

A precise alignment is needed to determine the center of the neutron beam emanating from the collimator. The reactor power was brought to 1kW to perform the alignment, and appropriate radiological precautions were observed in the vicinity of the beamport. The first step is to position the detector stage, the Huber 500 mm rotational stage, at a selected starting position approximately -15 degrees outside the neutron beam. The detector stage is rotated +0.1 degrees and a 3 second measurement from the ^{3}He detector is recorded and plotted with the LabVIEW VI. The process of rotating +0.1 degrees, recording a measurement and plotting the data is repeated through 30 degrees until the detector reaches approximately +15 degrees outside the beam, thereby passing the detector through the neutron flux maximum. The profiling procedure is depicted in Figure 4.13.

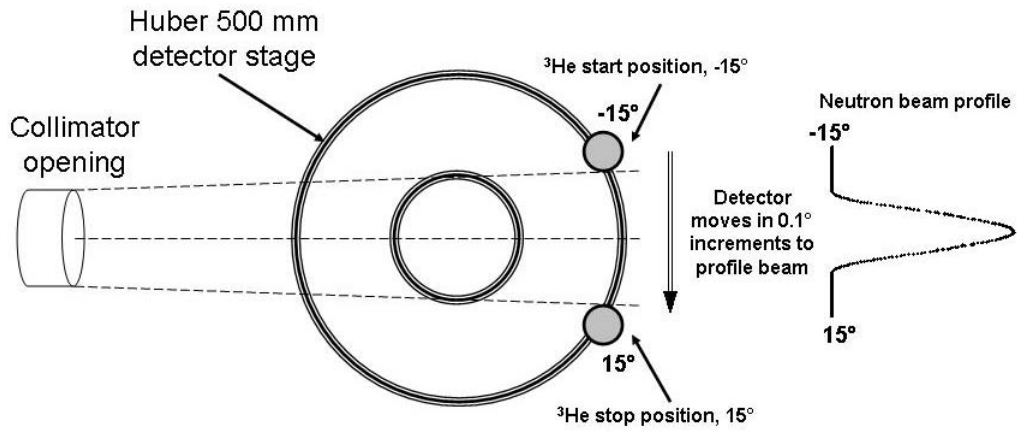

Figure 4.13: Top view of the diffraction configuration indicating the starting and stopping positions used to measure the beam profile.

The center of the count distribution (Figure 4.14) was used to determine the peak location that corresponds to center of the neutron beam. The ^{3}He detector was next rotated back to the peak position and the angular indicator for the detector location was reset to zero. The alignment procedure is depicted in Figure 4.15.

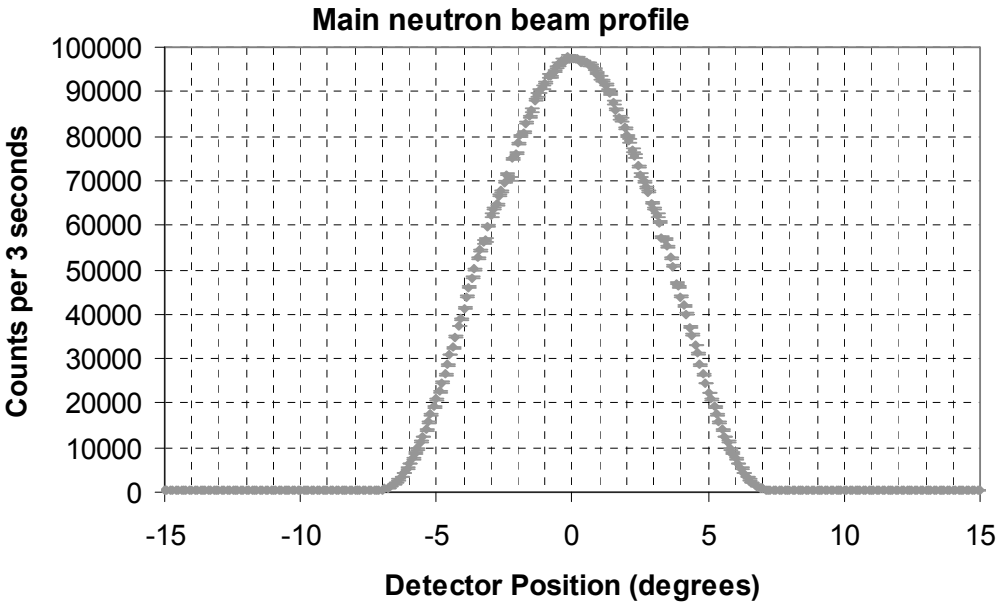

Figure 4.14: Beam profile as plotted in LabVIEW VI used to determine the neutron beam center.

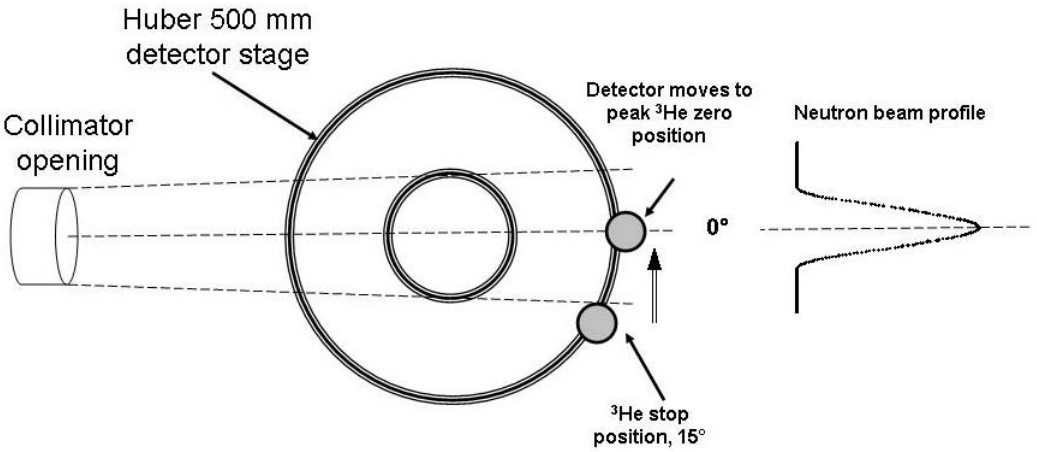

Figure 4.15: Top view of the diffraction configuration indicating the final position of the neutron beam center.

Afterwords, the ^{3}He detector was located and calibrated at the neutron beam center. The next step was to position the monochromator relative to the ^{3}He detector such that the relationship between the two satisfy the Bragg condition.

4.2.3 Diffracted Beam Center

Once the beam center was found, the reactor was shut down so the PG monochromator could be attached to the monochromator stage (the Parker 125mm rotational stage). The monochromator was visually aligned to produce a Bragg angle of approximately zero. After the monochromator was attached, the reactor was returned to power, 1kW. The detector stage was then rotated to +30 degrees such the ^{3}He detector was located outside of the neutron beam as depicted in Figure 4.16.

A ^{3}He detector position of 30 degrees corresponds to a monochromator angle and Bragg angle of 15 degrees when the two stages are calibrated to each other. The monochromator stage was first positioned at approximately 5 degrees relative to the beam and a measurement from the ^{3}He detector was recorded for 3 seconds and plotted by the LabVIEW VI. The process of rotating +0.1 degrees, recording a measurement and plotting the data was repeated up to 25 degrees relative to the beam. The procedure is depicted in Figures 4.17-18.

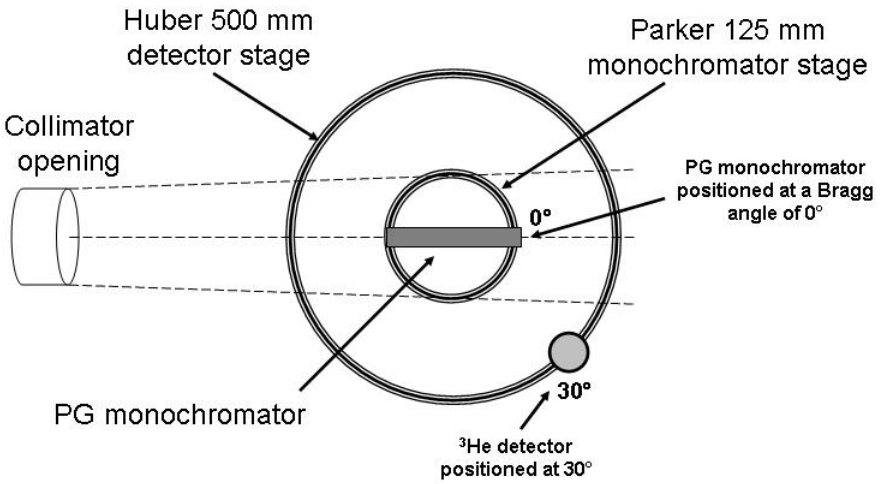

Figure 4.16: Top view of the diffraction configuration indicating the initial position of the monochromator and detector.

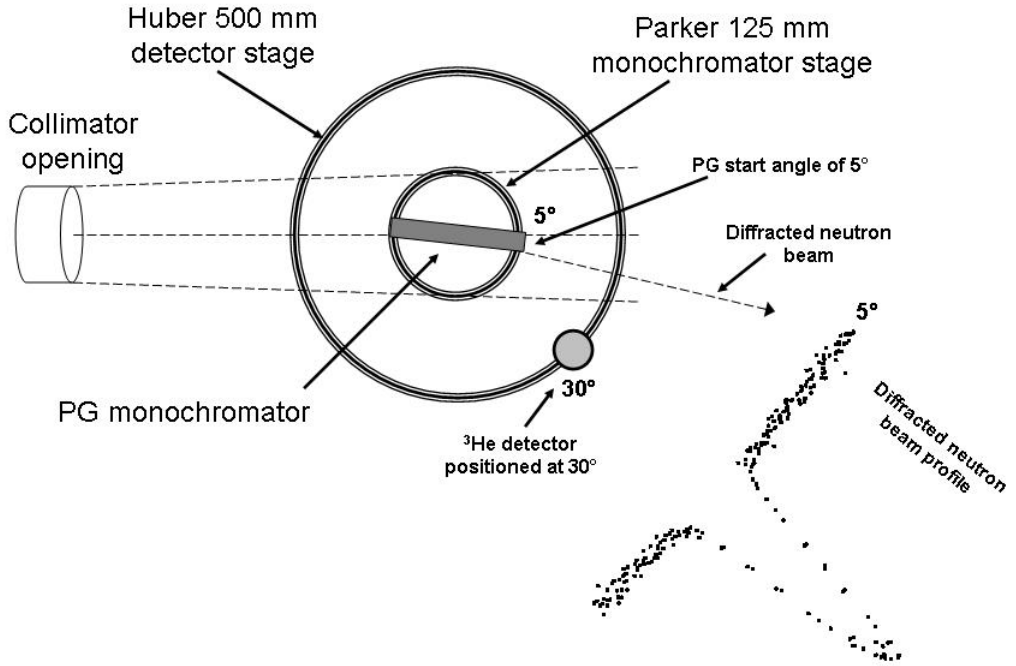

Figure 4.17: Top view of the diffraction configuration indicating the starting position of the monochromator and detector used to determine the diffracted beam profile.

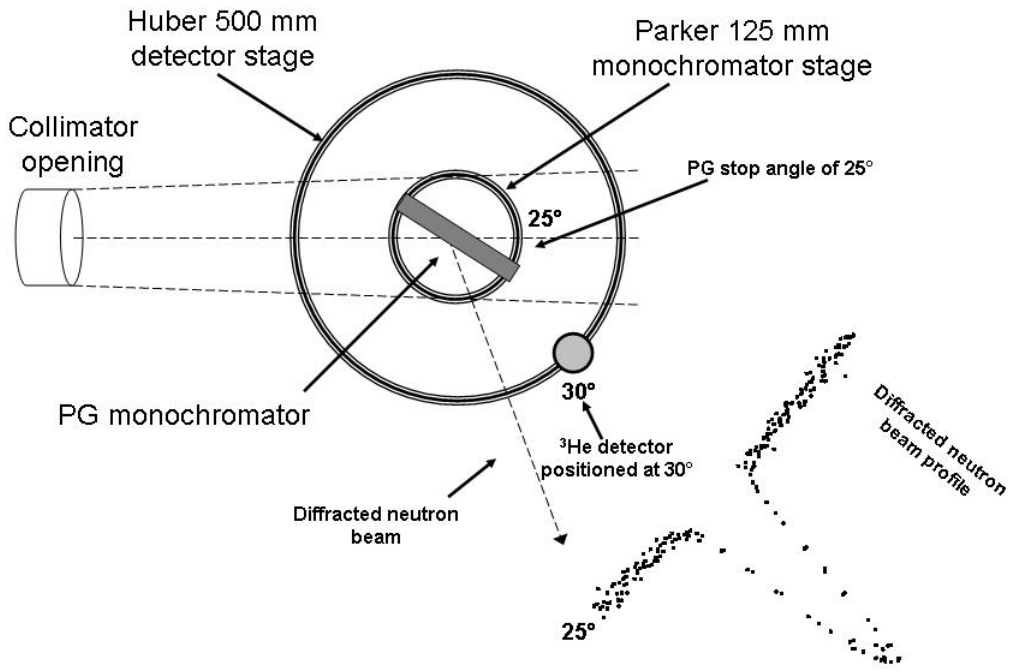

Figure 4.18: Top view of the diffraction configuration indicating the stop position of the monochromator and detector used to determine the diffracted beam profile.

The center of the diffraction peak is located on the LabVIEW plot (Figure 4.19). The peak location corresponds to a 15 degree monochromator angle that satisfies the Bragg condition. The monochromator stage was then rotated back to the Bragg peak position and the angular indicator for the monochromator location was reset to 15 degrees. Afterwords, the ^{3}He detector was calibrated to the diffracted beam center or the "Bragg condition". The procedure discussed above is depicted in Figure 4.20. As long as the stages are jointly rotated such that angular position of the detector is two times the angular position of the monochromator, the two stages will satisfy the Bragg condition. Upon completion of this calibration procedure, the equipment was ready to measure the thermal neutron leakage spectrum from the NWBP. The leakage measurement is sometimes referred to as a θ-2θ measurement because of the specific alignment needed to perform the measurement.

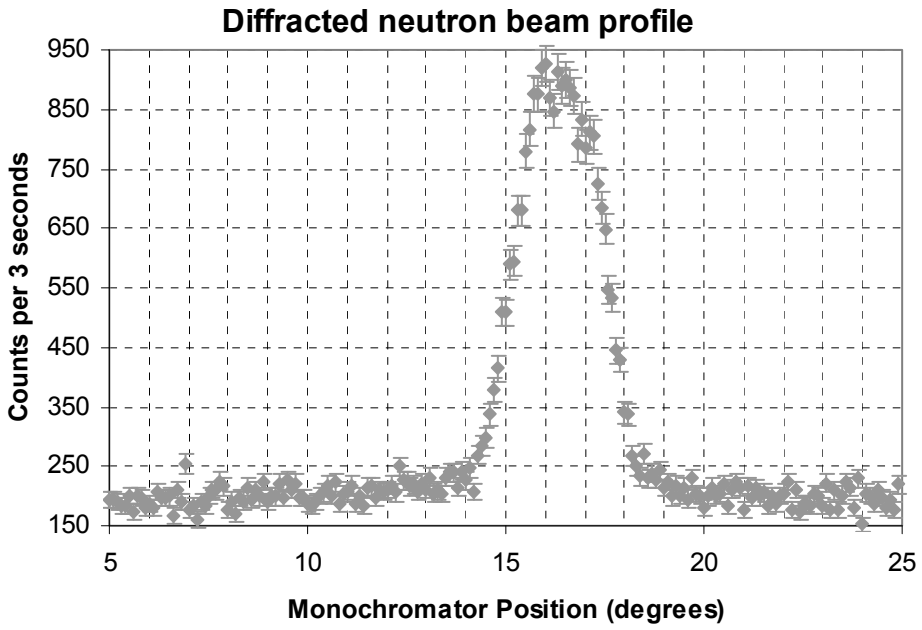

Figure 4.19: Diffracted Beam profile as plotted in LabVIEW VI used to determine the diffracted beam center.

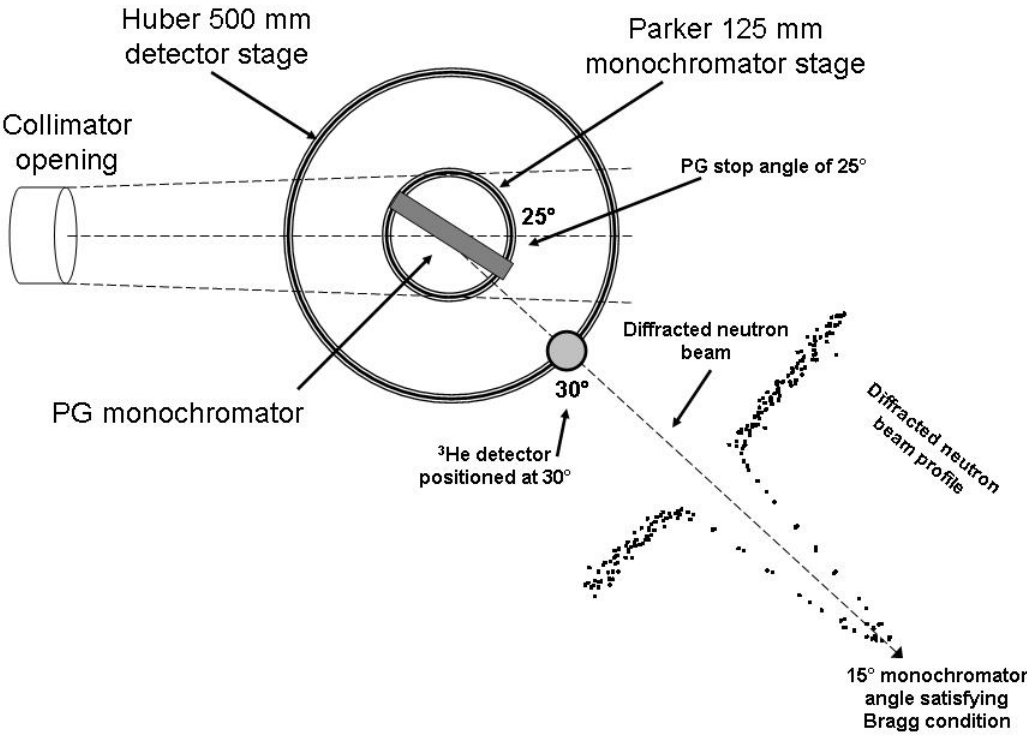

Figure 4.20: Top view of the diffraction configuration indicating the Bragg condition of the monochromator and detector.

4.2.4 NWBP Leakage Spectrum

Once the ^{3}He detector and monochromator stages are aligned, a thermal neutron leakage spectrum from the NWBP can be taken. This procedure requires two measurements; one of the neutron spectrum with background and one of just the background allowing it to be subtracted, hence yielding only the neutron leakage spectrum. The reactor was operated at 1kW for the measurements; hence the measured leakage spectrum is only applicable for 1kW. The ^{3}He detector and monochromator were both set at an angle of zero degrees (Figure 4.21) and a measurement was recorded for 10 seconds and plotted by the LabVIEW VI used for determining the neutron spectrum.

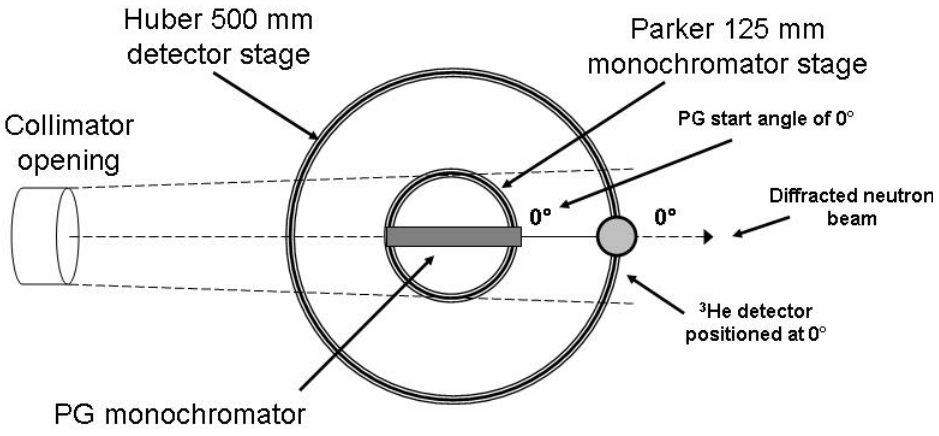

Figure 4.21: Top view of the diffraction configuration indicating the initial position of the monochromator and detector.

The monochromator was then rotated to a position of 0.1 degrees and the ^{3}He detector to a position twice the monochromator angle (0.2 degrees). The process of advancing the monochromator 0.1 degrees and the detector 0.2 degrees, recording a measurement and plotting the data is repeated until the monochromator and ^{3}He detector reach a position of 45 and 90 degrees, respectively as shown in Figure 4.22. The neutron spectrum with background is shown in Figure 4.23. The next step was to measure the background radiation produced from diffuse neutron scattering.

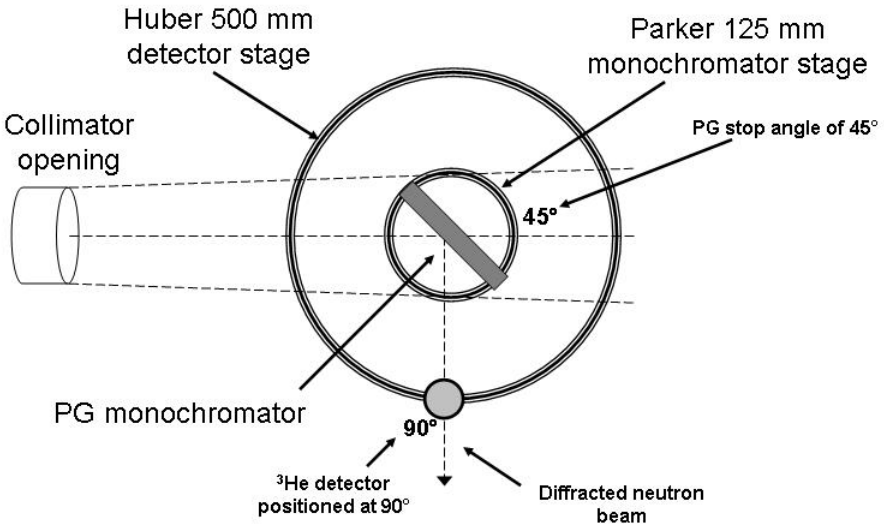

Figure 4.22: Top view of the diffraction configuration indicating the final position of the monochromator and detector in the Bragg condition to determine the beamport leakage spectrum.

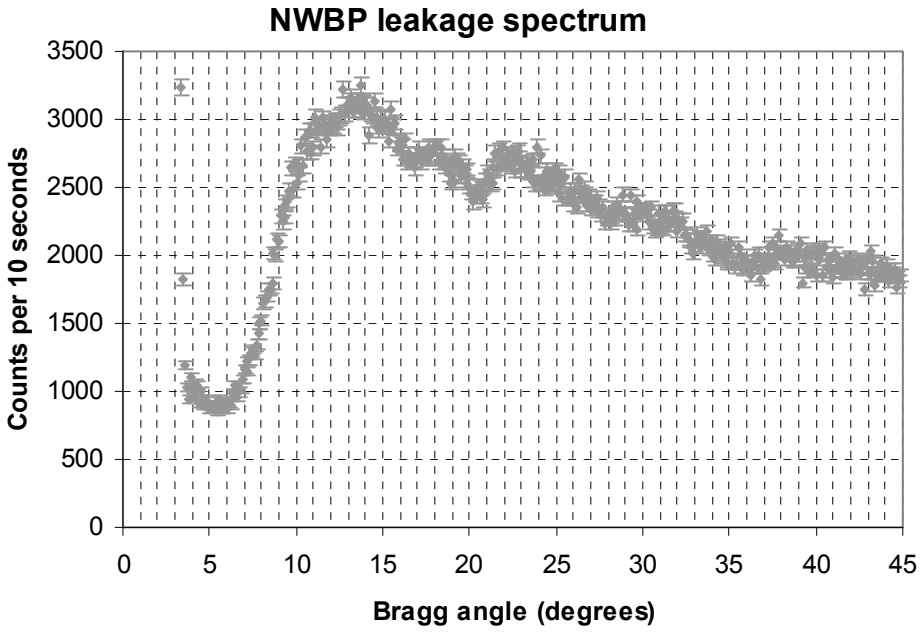

Figure 4.23: NWBP leakage spectrum as plotted in the LabVIEW VI used to determine the neutron spectrum, taken on June 11, 2007 at 1 kW of reactor power.

To perform a background measurement, the ^{3}He detector and monochromator are again returned to a position of zero degrees. However, the monochromator is further rotated such that it does not meet the Bragg condition. To keep the scattering geometry similar between the measurements, the monochromator was rotated only +2 degrees off the Bragg condition. The new position of the monochromator allows the ^{3}He detector to follow the diffracted beam, and thus not measure the diffracted neutrons as shown in Figure 4.24. Only the diffuse scattered neutrons can then enter the ^{3}He detector. With the monochromator positioned at 2 degrees and the ^{3}He detector positioned at zero degrees, a measurement was recorded for 10 seconds and plotted by the LabVIEW.

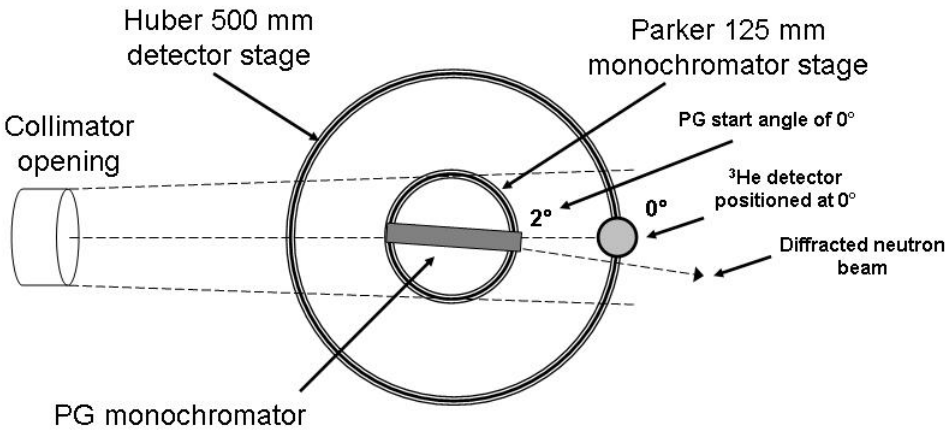

Figure 4.24: Top view of the diffraction configuration indicating the initial position of the monochromator and detector in the Bragg condition + 2 degrees to determine the background spectrum.

The monochromator was then rotated 0.1 degrees to a position of 2.1 and the ^{3}He detector to a position of two times the monochromator increment or 0.2 degrees. The process of advancing the monochromator 0.1 degrees and the detector 0.2 degrees, recording a measurment and plotting the data was repeated until the monochromator and ^{3}He detector reached a position of 47 and 90 degrees, respectively (Figure 4.25). The background neutron spectrum is shown in Figure 4.26.

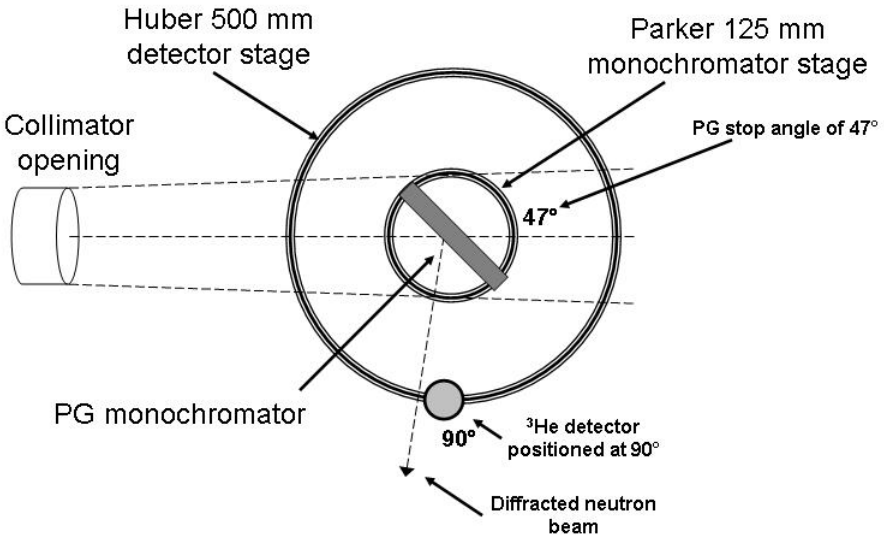

Figure 4.25: Top view of the diffraction configuration indicating the final position of the monochromator and detector in the Bragg condition + 2 degrees to determine the background spectrum.

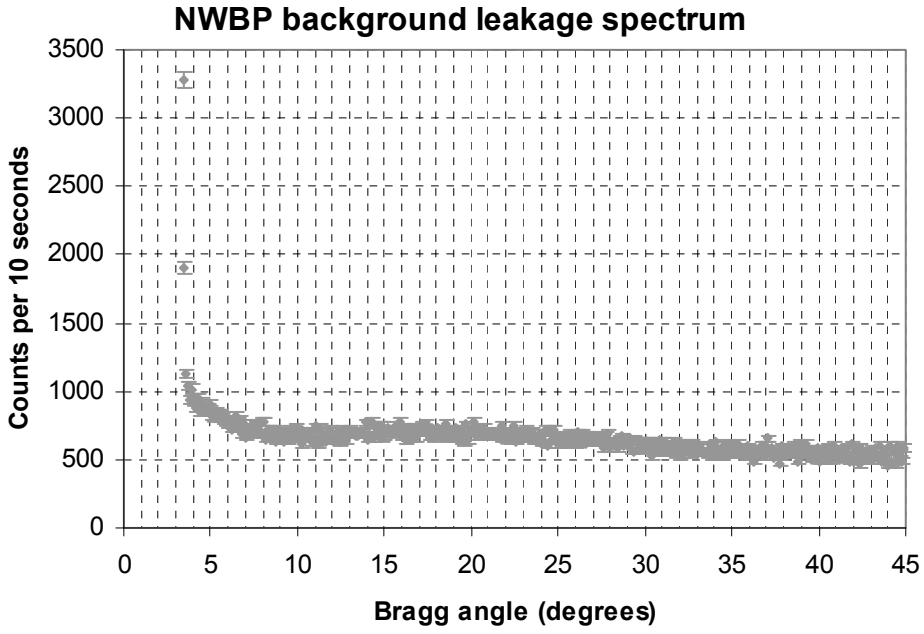

Figure 4.26: NWBP background spectrum as plotted in the LabVIEW VI used to determine the neutron spectrum, taken on June 11, 2007 at 1 kW of reactor power.

4.3 Final Arrangement

After the diffraction equipment was calibrated and a beamport leakage spectrum taken, the equipment was adjusted to an angle that yielded the desired calibration energy, being 15.5 degrees and 0.0253 eV respectively. After the final angle was determined, radiation shielding was carefully constructed to protect experimenters from radiological hazards, yet still allowing the diffracted neutron beam to be accessible. After shielding was in place, a test port was constructed that allowed accurate neutron measurements to be taken. Finally a neutron intensity calibration was performed, thereby allowing the port to be used for detector efficiency calibrations.

4.3.1 Calibration Energy

The thermal neutron energy desired for calibrations at the test port was 0.0253 eV because that was the energy utilized for neutron detector design calculations. With PG as the monochromator, this energy corresponds to a Bragg angle of 15.5 degrees. As such, the monochromator was then rotated to a position of 15.5 degrees and the detector was rotated to a position of 31.0 degrees. The detector was then removed from the Huber rotational stage. The position where the detector was located relative to the central axis of the monochromator was used to determine where the diffracted neutron beam is directed. Once the path of the diffracted neutron beam is determined, shielding can be appropriately placed around the diffracted beam.

4.3.2 Shielding Arrangement

The first large shielding block to be installed at the NWBP was block #2 with the beam catcher built in. Block #2 was placed to align the central axis of the block along the central axis of the collimator. The next large shielding block to be installed was block #1 that fit evenly against the reactor wall. The last large shielding block to be installed was block #3 with the cutout that allows the diffracted neutron beam to escape the shielding. After the large blocks were installed, the two smaller blocks were placed on top of the larger blocks to keep up-scattered radiation to a minimum. Sheets of #210 30% boron polyethylene [36] were also cut and placed on top of the outer blocks against

the reactor wall to further limit exposure from up-scattered radiation (Figure 4.27). A wire fence was installed to limit personnel access to areas not related to the neutron detector test facility.

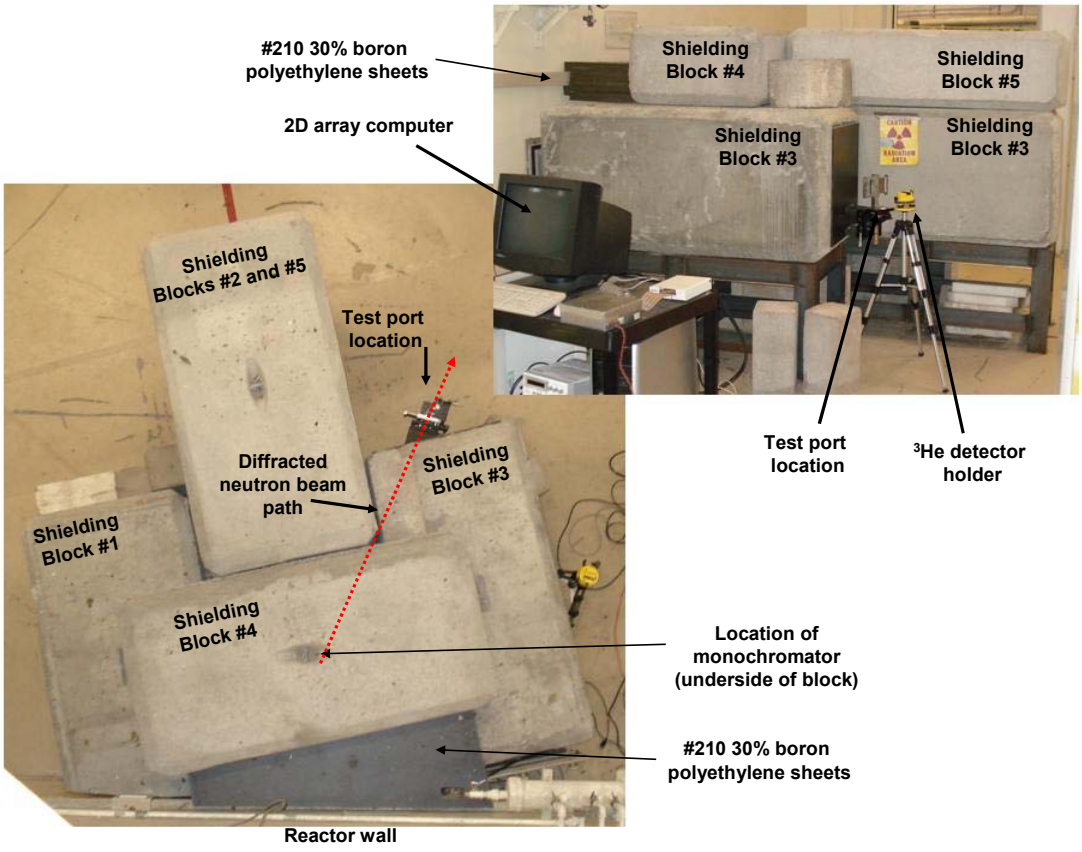

Figure 4.27: Top (left) and side (right) view of biological shielding at the NWBP.

4.3.3 Test Port Arrangement

In order to accurately and repeatability position the neutron detectors at the test location a general purpose mounting fixture (Figure 4.28) was installed at the diffracted beam opening. The mounting fixture was installed on a X-Y linear stage to allow the irradiation position to be adjusted so that the detector can be placed in the most uniform part of the neutron beam. A neutron absorbing shutter was installed on the test fixture to block the beam during detector placement. It also allowed experimenters to distinguish

between the diffracted beam neutron response and the response due to both scattered neutrons and gamma rays. The shutter material chosen was cadmium. The thin sheet of cadmium is flexible, so it was attached to a more rigid sheet of aluminum. The aperture in the cadmium/aluminum shutter is a circular hole 1.27 centimeters (0.5 inches) in diameter. When in the open position, the cadmium shutter aperture aligns with the active area of the detector and allows the diffracted neutron beam to pass through. When in the closed position, the cadmium shutter blocks the diffracted neutrons from entering the active area of the detector. With the shutter closed two observations can be made. First, the cadmium absorbs nearly all of the neutrons from the diffracted beam, so the scattered neutron response can be determined. Second, when the diffracted neutrons are absorbed by the cadmium and aluminum they produce secondary gamma rays that can be measured in the neutron detector. The ideal neutron detector has little measurable response from gamma-ray interactions. Therefore the Cd shutter also allows the experimenter to observe the detector response to gamma rays.

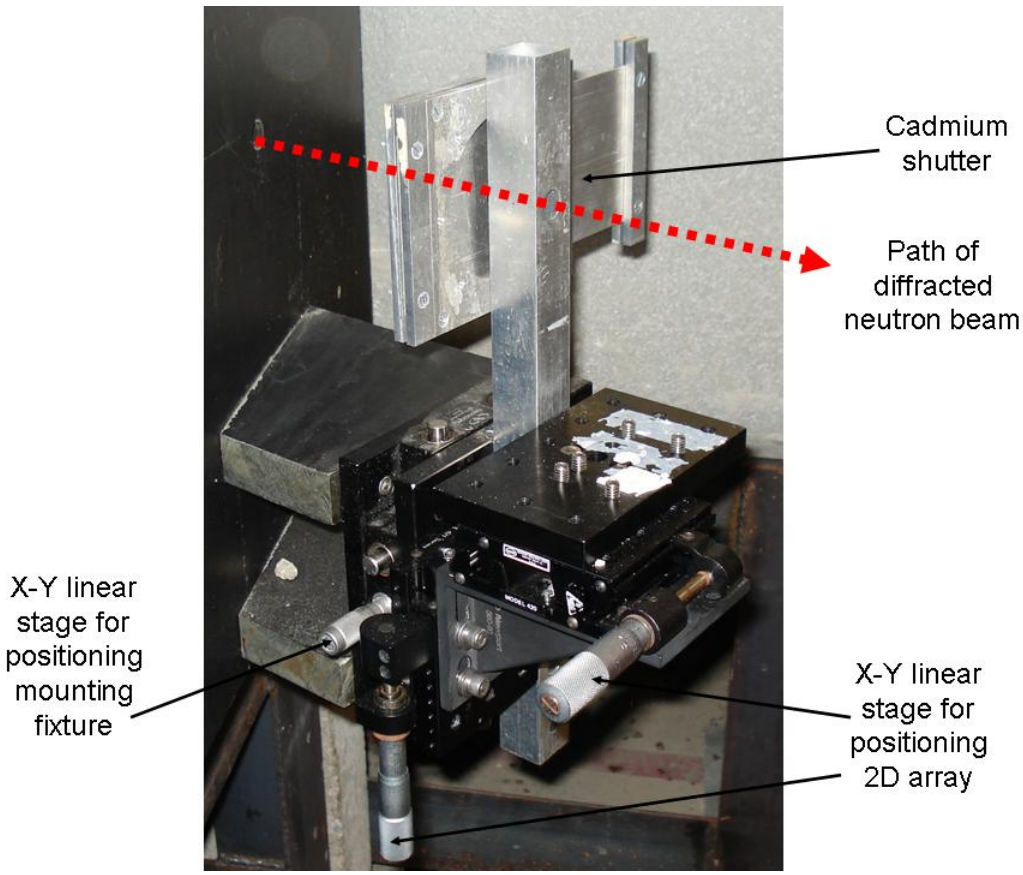

Figure 4.28: Mounting fixture installed at NWBP.

4.3.4 Uniformity and Intensity Calibration

The last step in setting up the detector test facility involved characterizing the uniformity and intensity of the neutron beam at the test port. A Polaroid film cassette was used with a 3" x 4" sheet of NE426, a ^{6}Li-ZnS neutron sensitive scintillator, installed in front of the Polaroid 667 film (Figure 4.29) to characterize the uniformity of the diffracted neutron beam. The cassette was placed on the test port opening and the resulting image was observed.

Figure 4.29: Polaroid film cassette (left) with NE426 (white sheet inside) installed (right) used to measure the uniformity of the diffracted neutron beam at the test port.

After the uniformity was confirmed, the intensity was determined by installing the ^{3}He detector at the test port opening (Figure 4.30) and counting for a specific amount of time. The cadmium shutter was then closed and a background measurement was taken. The measurement with the shutter closed was subtracted from a measurement with the

shutter open to determine the net count due to diffracted neutrons. The net count was then divided by the live count time to determine the net count rate. Finally the net count rate was divided by the shutter aperture area of 1.27 cm^2 to get the neutron intensity in units of $n \cdot cm^{-2} \cdot s^{-1}$. Recent work indicates the ^3He detector is most efficient when the neuron beam enters perpendicular to the central axis of the detector yielding 80.7 $\pm$ 0.50% detection efficiency [38]. Current work places the ^3He detector perpendicular to the neutron beam, not parallel to the neutron beam as shown in Figure 4.30 [38].

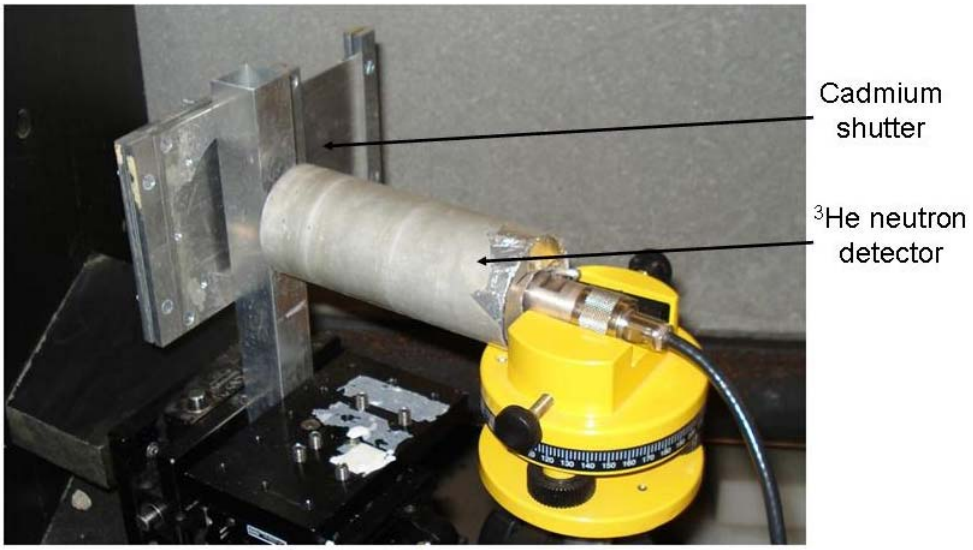

Figure 4.30: ^3He detector used to determine the neutron intensity at the test port opening.

CHAPTER 5 - Results

The construction of a 2-D neutron detector and a neutron detector test facility has been completed. The detector test facility was characterized to provide a calibrated neutron beam to the experimenter by neutron diffraction. A neutron spectrum was measured to determine the diffraction energy utilized for calibrations. The radiological hazards at the detector test facility were minimized by installing a sapphire neutron filter that allowed the majority of the diffracted neutrons to reach the experimenter while minimizing the background gamma radiation. The uniformity and intensity of the diffracted neutron beam was measured to provide a reference for testing of future designs of neutron detectors. Real time monitoring, both uniformity and intensity, of the diffracted neutron beam was achieved by installing a 2-D neutron detection array. The 2-D array was calibrated at the detector test facility for future use as a neutron imaging beam monitor.

5.1 Detector Test Facility

Several tests were used to determine the validity of the setup of the detector test facility. The first test involved observing the neutron leakage spectrum before the biological shielding was in place. The test was performed with and without the sapphire filter installed to determine how the filter affected the diffracted neutron response. The second test involved observing the radiation dose rates with biological shielding in place. This second test was also performed with and without the sapphire filter installed to determine if the filter functioned as intended to reduce radiation exposure. A third test was performed to observe the uniformity of the diffracted neutron beam at the test port. The final test determined the intensity of the diffracted neutron beam at the test port. The results of these tests are discussed in the following sections.

5.1.1 Neutron Spectrum

Two neutron leakage spectra were measured at the NWBP. Before and after spectra were taken with and without the sapphire filter installed in the collimator. The

reactor was operated at 1 kW for both configurations. For clarity, select portions of these two specta are plotted together in Figure 5.1 and normalized in Figure 5.2.

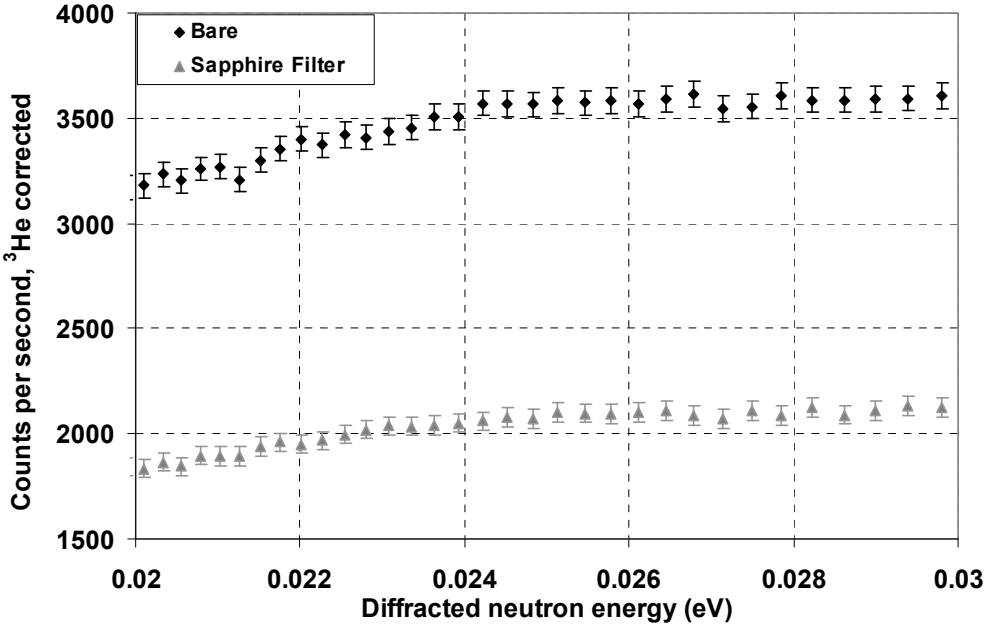

Figure 5.1: Neutron specta from NWBP showing the before and after of installing a sapphire filter.

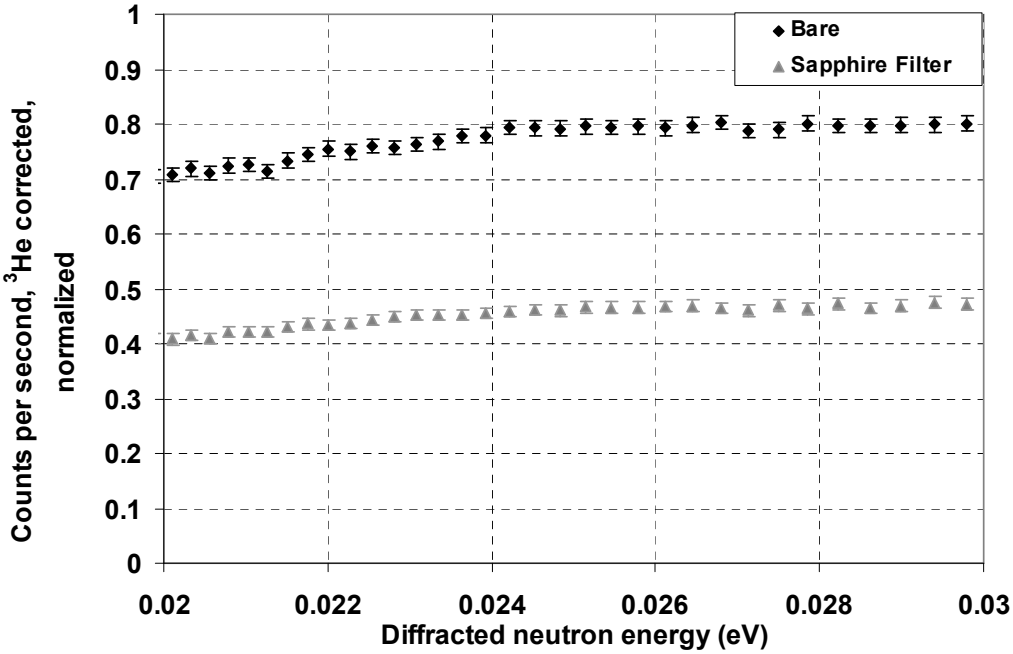

Figure 5.2: Normalized neutron specta from NWBP showing the before and after of installing a sapphire filter.

At 0.0253 eV neutron energy, the ^{3}He detector has a detection efficiency of 80.7 $\pm$ 0.50% when positioned vertically (5 cm diameter). The corrected neutron intensity is 3576 counts $\pm$ 0.72% neutrons per second without the sapphire filter installed verses 2097 counts $\pm$ 0.95% neutrons per second with the sapphire filter installed. It can be concluded that the installation of the filter will reduce the amount of 0.0253 eV neutrons by 41%. The reduction in neutron intensity was expected to be approximately 25% based on the literature (Figure 4.2) [25]. The crystal quality of the sapphire is unknown and is a possible cause for the inconsistency in expected neutron transmission. Impurities in the sapphire would cause more neutrons to be absorbed or scattered before leaving the crystal. The overall shape of the energy spectrum without the sapphire filter was measured as shown in Figure 5.3. The contamination evident by the down-peaks in the spectrum below 0.05 eV are due to the absorption of the thermal neutrons by the graphite reflector surrounding the reactor core and the aluminum reactor pool tank liner that the neutron beam must penetrate before reaching the monochromator. The data was corrected by including the energy dependence (Eq. 4.3) of the vertical ^{3}He detector (5 cm diameter) utilized in the measurement [38]. The harmonic n = 2,3 order contamination for the primary 0.0253 eV diffraction (n = 1) are located at 0.101 eV and 0.227 eV for the second and third order, respectively.

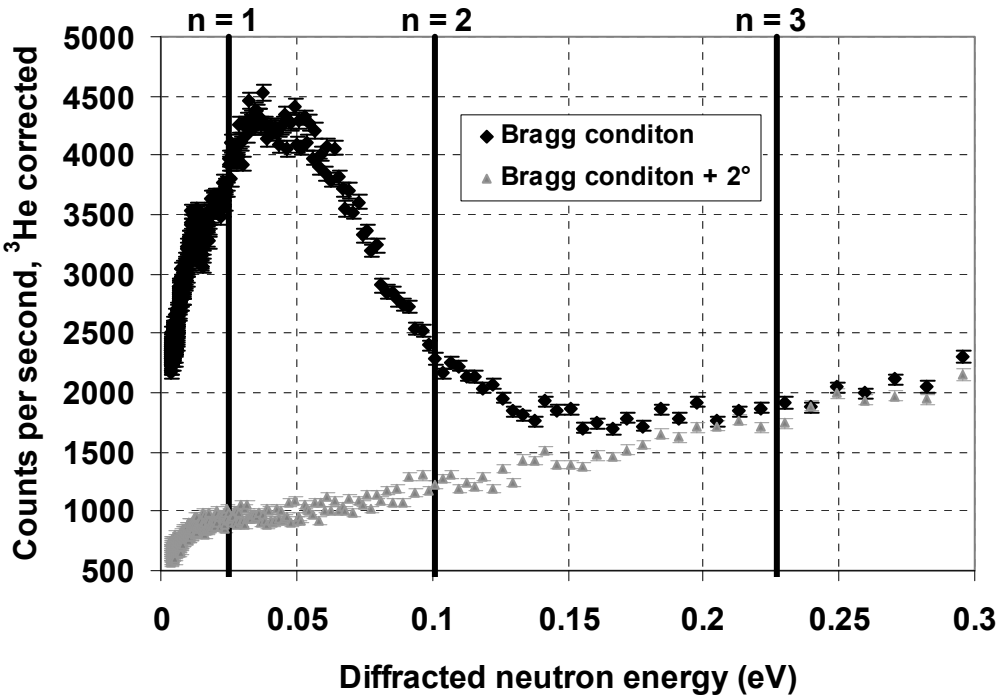

Figure 5.3: Beamport leakage specta using (002) PG.

5.1.2 Dose Rates

The neutron and gamma-ray dose rates around the biological shielding were measured before and after (Table 5.1) installation of the sapphire filter. The reactor was operated at 100 kW for both tests. The testing locations (Figure 5.4) remained the same for each test. A Victoreen Geiger-Müller counter, model number 450P, serial number 1474, was used to measure the gamma-ray dose and a Ludlum Remball, model number 12-4, serial number 47138, was used to measure the neutron dose.

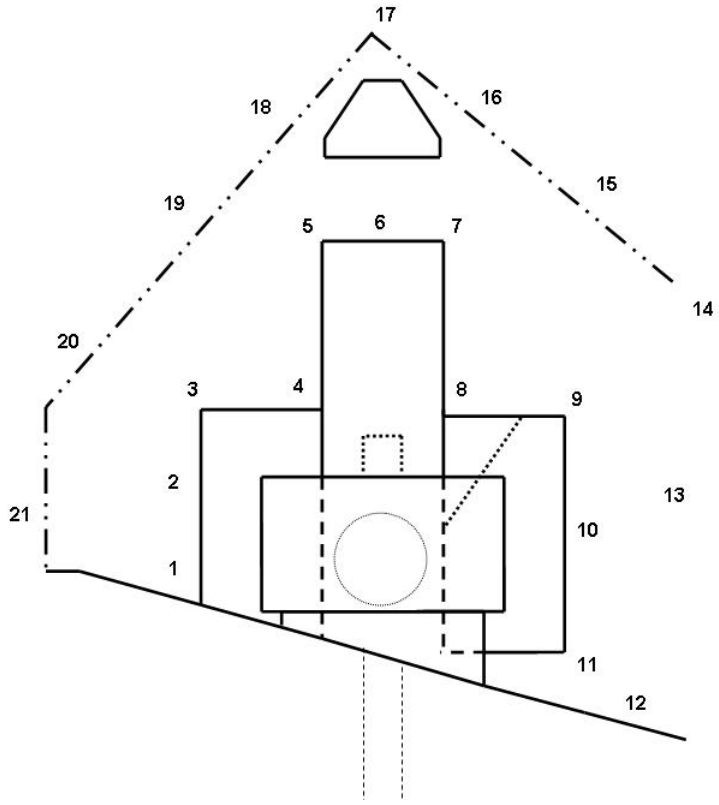

Figure 5.4: Neutron and gamma ray doses locations listed in Table 5.1.

Table 5.1: Dose rates at detector test facility before/after installation of sapphire filter at 100 kW of reactor power.

Position	Gamma-ray Dose (mRh^{-1})	Neutron Dose (mRh^{-1})	Gamma-ray Dose (mRh^{-1})	Neutron Dose (mRh^{-1})
	At Floor Level		At Torso Level	
1	2.6 / 1.13	5 / 1	0.9 / 0.25	1 / 1
2	3 / 1.5	5 / 1	0.4 / 0.2	<1 / <1
3	1.9 / 0.8	3 / 1	4.6 / 2	5 / 2
4	3.2 / 1.09	5 / 1.5	14 / 6.5	35 / 3
5	2.4 / 0.63	4 / 1	1.1 / 0.3	1.5 / 1
6	4.2 / 1.7	5 / <1	17 / 6.6	3 / <1
7	2.8 / 0.7	4 / 1	1.2 / 0.3	2 / 1
8	3.7 / 1.3	20 / 2	39 / 35	100 / 25
9	3.2 / 0.8	5 / 1	1.1 / 0.6	2 / 1
10	4.2 / 1.34	6 / 1	0.5 / 0.3	<1 / <1
11	3.6 / 1.3	8 / 2	2 / 1.3	8 / 1

Position	Gamma-ray Dose (mRh^{-1})	Neutron Dose (mRh^{-1})
	Maximum of Floor and Torso Level	
12	1 / 0.6	4 / <1
13	1.8 / 0.3	4 / <1
14	2.6 / 0.9	3.5 / 1
15	1.8 / 0.4	2 / <1
16	0.8 / 0.5	1 / <1
17	0.3 / 0.1	1 / <1
18	0.3 / 0.1	1 / <1
19	1 / 0.2	2 / <1
20	0.8 / 0.3	2 / <1
21	0.7 / 0.2	1.5 / <1

The installation of the sapphire filter reduced the radiation exposure in all areas around the biological shielding and fenced area. The largest reduction for gamma-ray dose, approximately 83%, is at position 13 (see Fig. 5.4). The largest reduction for neutron dose, approximately 91%, is at position 4 at torso level. The highest doses recorded (position 8) is due to the fact that the diffracted neutron beam passes directly over the location. As stated in section 5.1.1, the diffracted neutron beam flux was also reduced by installation of the sapphire filter, however the reduction was only 41%. The filter improved area dose rates while maintaining a usable neutron beam for detector calibrations.

5.1.3 Neutron Uniformity and Intensity

The uniformity of the neutron beam at the detector test port is shown in Figure 5.5 below. The Polaroid film was in the neutron beam for 60 seconds at a reactor power of 1 kW.

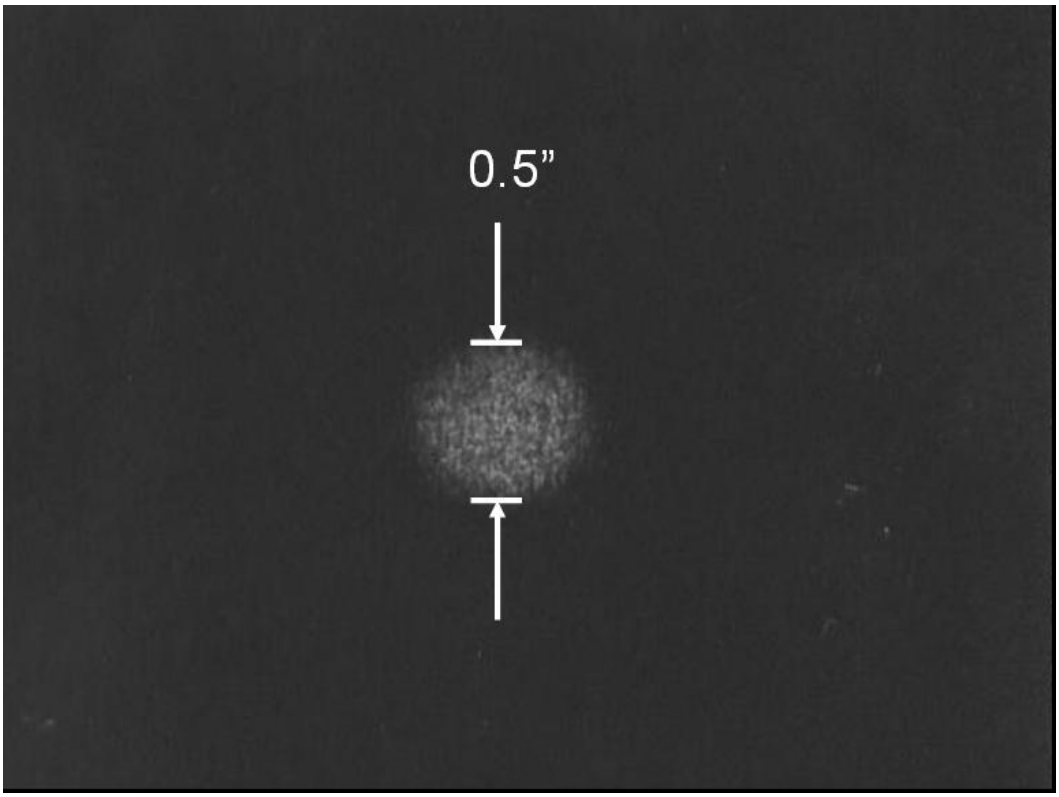

Figure 5.5: Neutron imaged film showing the uniformity of the diffracted neutron beam.

The film was uploaded to GIMP, an image manipulation program to determine the uniformity across the image. The image colors were inverted for easier viewing and the viewing threshold for the grayscale was slowly raised while observing the change in the resulting image (Figure 5.6). The resulting images indicate a slight non-uniformity in the upper right of the beam, but an otherwise uniform beam.

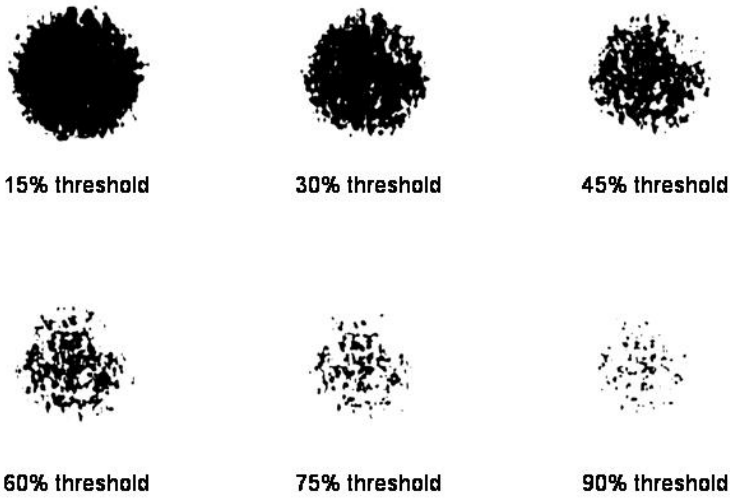

Figure 5.6: GIMP images of various grayscale thresholds for the diffracted neutron beam image.

The intensity of the neutron beam at the detector test port measured with the ^{3}He neutron detector was found to be $1.46x10^{4}$ $n \cdot cm^{-2} \cdot s^{-1} \pm 0.62\%$ [38]. It was in the neutron beam for 300 seconds at a reactor power of 100 kW. The 300 second measurement with the shutter open was 4527337 counts $\pm$ 0.05% and the 300 second measurement with the shutter closed was 43648 counts $\pm$ 0.48% as shown in Figure 5.7. The shutter lowered the neutron response by 99.04% $\pm$ 0.48%.

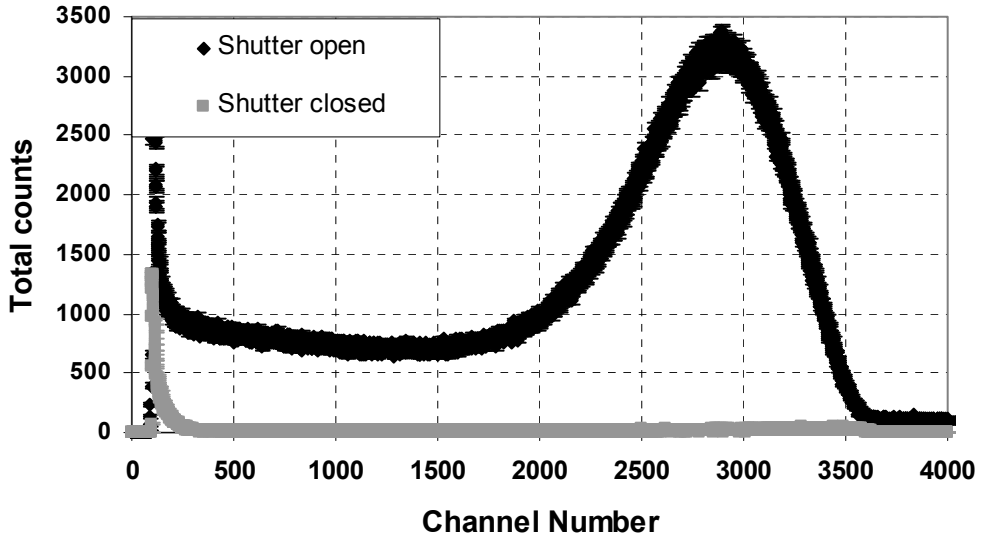

Figure 5.7: Specta from a ^{3}He detector showing 300 second live time measurements for the cases in which the Cd shutter is open and closed.

5.2 Neutron Detector

Each pixel in the 2-D array was tested for response, appropriate scaling factors were assigned to produce a uniform response, and the final overall neutron detection uniformity was verified. The overall detection efficiency was then determined. The results of these tests are discussed in the following sections.

5.2.1 Pixel Response

The response from each pixel with a scaling factor of one is shown in Table 5.2 below. The measurement time for each pixel is 600 seconds with the reactor operated at 100 kW. The response varied from a high of 9149 counts to a low of 3026 counts. The varying detection responses can be due to several factors. Any non-uniformities in the ^{6}LiF coating would directly effect the observed response. The ^{6}LiF coating was applied at 1.0 μm which is a theoretical detection efficiency of 0.54%; a $\pm$10% deviation in thickness (0.9-1.1 μm) would result in a theoretical efficiency range of 0.49% to 0.59%. Coating inconsistencies could explain a small change in the detection efficiency, but not the large change that was observed. A more likely cause of various detection responses could be a result of a small change in the gain or threshold adjustment from channel to

channel. The arrangement of the amplifier board did not allow for individual spectra to be measured; hence the spectra may have been shifted slightly from one detector to another because of varying gain and threshold adjustments. If a spectrum was shifted outside of the measurement window then the resulting response would be drastically different.

Table 5.2: Response from each pixel of 2-D array with a scaling factor of one.

8733	**6873**	**8858**	**8848**	**9149**
8019	**7835**	**6275**	**8087**	**8530**
7869	**7517**	**8138**	**8289**	**8675**
7527	**7584**	**8278**	**8359**	**8803**
3026	**7986**	**8502**	**8713**	**9041**

After operation of the detector, it was discovered that one of the amplifiers on the circuit board was assembled with different components then the other amplifier circuits. The installation of the incorrect components on the amplifier circuit was connected to the same pixel that was responsible for the lowest reading on the entire array, 3026 counts. The misplaced components resulted a lower gain on the channel; hence a lower reading was observed. Installing the correct components fixed the low reading; however the component was not installed prior to the completion of the data to demonstrate that scaling factors could be applied in the software to adjust the observed output arrays.

The initial responses from the pixels were next used to determine the scaling factors needed to produce a uniform response across the detector. The scaling factors assigned to each pixel were implemented to raise the observed response to that of the pixel with the maximum counts. The scaling factors utilized are shown in Table 5.3.

Table 5.3: Scaling factors generated for each pixel from the response shown in Table 5.2.

0.955	0.751	0.968	0.967	1.000
0.876	0.856	0.686	0.884	0.932
0.860	0.822	0.890	0.906	0.948
0.823	0.829	0.905	0.914	0.962
0.331	0.873	0.929	0.952	0.988

With the scaling factors from Table 5.3 added to the VI, another response test was performed under the same testing conditions. The result of the testing yielded a more uniform response as shown in Table 5.4. The response now only varied by a high of 9208 counts to a low of 9036 counts. The scaling factors thus brought the observed pixel responses to within less than 1.87% of each other.

Table 5.4: Response from each pixel of 2-D array with scaling factors from Table 5.3.

9145	9208	9083	9073	9180
9200	9116	9114	9176	9185
9140	9156	9107	9110	9165
9106	9155	9036	9046	9070
9125	9179	9152	9167	9064

.

5.2.2 Efficiency Calibration

The efficiency of the detection array was determined by comparing the response of a ^{3}He detector in a diffracted neutron beam (set at 0.0253 eV) to the response of the detection array in the same neutron beam. The ^{3}He detector was measured to be 80.7 + 0.50% efficient for 0.0253 eV neutrons based on recent work [38]. It was assumed that the beam intensity remained constant between measuring the response from the ^{3}He detector and from the detection array.

The array was tested at the detector test facility for 600 seconds at a reactor power of 100 kW. The efficiency of the array was determined using the overall average of the scaled pixel responses. The observed efficiency across the detector is then assumed to be uniform because each channel had an appropriate scaling factor assigned. The measured efficiency of the detector was found to be 0.412% $\pm$ 0.043% as compared to the ^{3}He neutron detector. A 1.0 μm coating of ^{6}LiF yields a theoretical efficiency of 0.537%; hence the experimental results were 23.3% less then the theoretical result.

CHAPTER 6 - Discussion

Many observations can be made from the design, setup, operation, and characterization of the detector test facility and accompanying 2-D neutron detection array. Both aspects of the neutron diffraction and neutron detection project are operational and work together to yield a valuable tool for testing and characterizing future designs of neutron detectors. Most beam monitors provide a single measurement of the beam flux and must rely on other methods (not real time) to characterize the neutron beam profile. The 2-D neutron detection array measures both the beam flux and the beam profile in real time. All beam monitors must be used as a transmission detector as it is desirable to leave the neutron beam unperturbed. The construction and materials utilized for the 2-D neutron detection array yields a beam monitor that transmits a calculated 99.4% of the neutron flux. Many valuable observations have been noted and improvements for the detector test facility and 2-D neutron detection array have been realized that can be applied to future iterations. The current operation and future recommendations of the detector test facility and 2-D neutron detection array are discussed in the following sections.

6.1 Diffraction

The overall goal of using neutron diffraction to produce the detector test facility has several benefits as compared to performing testing directly in a reactor beamport. The detector testing location was placed in a purely thermal neutron beam that allows a calibration based on thermal neutron response alone. The detector test facility allows researchers to conveniently, easily, and safely test multiple neutron detectors. It is unnecessary to shutdown the reactor to change detectors because the testing facility is away from radiological hazards of the main neutron beam. The reactor can now maintain a steady state power level for all detector testing. The radiation exposure to other experiments in the reactor bay is also minimized because the radiation from the main beam is contained in the shielding. The test facility is dedicated to an otherwise unused beamport and maintains the research capabilities of the other beamports. The specifics

regarding these benefits and how they may be improved are discussed in the following sections.

6.1.1 Detector Test Port

The use of neutron diffraction to produce a detector testing facility yielded a valuable experimental tool for the KSU SMART Lab. The use of pyrolytic graphite at a final Bragg angle of 15.5 degrees diffracts thermal neutrons with a Gaussian average of 0.0253 eV. The energy has negligible harmonic n = 2,3 order contamination based on the measured beamport leakage neutron spectrum coupled with the Maxwellian distribution of the reactor core. Installation of the sapphire filter does reduce the intensity of the 0.0253 eV neutrons by 41%, however the filter also reduces the dose rates in the area by as much as 91%. The filter is a necessary component to the facility to achieve a radiologically safe working environment. The use of the ^{3}He neutron detector for intensity calibration yielded a neutron flux of $1.46x10^{4}$ $n \cdot cm^{-2} \cdot s^{-1} \pm 0.62\%$ [38]. Overall, the detector test facility has met all of the goals set forth, however there are some recommended improvements.

6.1.2 Future Work on Test Facility

Further characterization of the diffracted neutron beam includes an independent determination of the energy of the neutrons at the test port. The typical method involves an experiment that directly measures the velocity of the neutron, referred to as a time of flight (TOF) experiment [17,19,20]. A TOF experiment relies on a measurement of the time it takes a neutron to travel along a flight path. A neutron beam requires a neutron chopper (velocity selector) to separate a pulse of neutrons. A neutron detector is then placed in the pulsed neutron beam a specific distance from the chopper and the time delay associated between the pulse production and the detector response is measured. Accurately measuring the time and distance will enable an operator to determine the velocity, and thus the energy.

The limiting factor in the design of the biological shielding utilized at the detector test facility is the maximum floor loading requirements of the reactor bay floor. Further improvements could be realized with the installation of a floor that would allow for heavier shielding. Also, if the new floor is designed to be optically perfect, air casters

could be utilized that would allow for easily translatable shielding that would maintain the horizontal position of the test port location throughout shielding movements. With easily translatable shielding, the Bragg angle could be changed frequently, yielding a wide range of energies available for neutron calibrations.

6.2 Neutron Detector

The 5x5 neutron detector is the first silicon based, ^{6}LiF thin-film coated, 2-D neutron detector produced and tested by the KSU SMART Lab. The 5x5 array has several benefits as compared to traditional neutron beam monitors. The array is constructed using materials with low neutron absorption so it can be placed before experiments and used to monitor the neutron beam in real time. The detection efficiency can be easily adjusted during construction. The construction of the detector can be easily redesigned to produce a larger or smaller detector with greater or less spatial resolution. The specifics regarding these benefits and how they may be improved is discussed in the following sections.

6.2.1 Detector Performance

The 5x5 neutron detection array demonstrates the usefulness of semiconductor neutron detector for imaging purposes. Initial testing demonstrated non-uniformities between each pixel that could be easily corrected by applying scaling factors in the software. With the scaling factors applied, the response across the device was found to deviate by less then 1.8%. However, the non-uniformity is likely a result of the manufacturing process and amplifier settings that could be easily corrected with proper precautions or by observing the individual spectra from each channel. The theoretical efficiency of a ^{6}LiF coating 1 um thick is 0.53%; the measured result of 0.41% is 23% lower then the theoretical model.

6.2.2 Future Work on 2-D Array

Common VLSI fabrication techniques make silicon based thin-film neutron detector construction straightforward. As such, the basic design demonstrated can be scaled as necessary to produce a neutron detection array ideal for any experimental setup.

A higher or lower spatial resolution is achievable by simply changing the photoresist pattern, or more specifically the pixel size. In the same respect, the overall size of the detector can be made smaller or larger. Depending on the size, larger detectors may require several detection arrays to be placed side by side with careful consideration of placement of the output signal traces. The use of ^{6}LiF as a converter material allows the neutron detection efficiency to be adjusted to as high as 4.3% [5]. However, with use of perforations to hold more converter material and proper design to capture the secondary charged particles, the neutron detection efficiency could be made much higher for experiments that do not require a low perturbation of the neutron beam [10-14].

References

[1] G.E. Bacon, *Fifty Years of Neutron Diffraction*, Bristol: IOP Publishing, 1986.

[2] D.S. McGregor, "NE 612 Radiation Detection" (Class notes), 2004.

[3] J.K. Shultis and R. E. Faw, *Fundamentals of Nuclear Science and Engineering*., New York: Marcel Dekker Inc, 2002.

[4] N. Tsoulfanidis, *Measurement and Detection of Radiation*, 2nd ed. Washington, DC: Taylor and Francis, 1995.

[5] G. F. Knoll, *Radiation Detection and Measurement*, 3rd ed. New York: Wiley, 2000.

[6] L. Dobrzynski and K. Blinowski, *Neutrons and Solid State Physics*, Hertfordshire: Ellis Horwood Limited, 1994.

[7] D.S. McGregor, T.C. Unruh, and W.J. McNeil, "Thermal Neutron Detection with Pyrolytic Boron Nitride," *Nuclear Instruments and Methods*, A591, pp. 530-533, 2008.

[8] Z.W. Bell, K.R. Pohl, and L. Berg, "Neutron Detection with Mercuric Iodide," *IEEE Trans. Nuclear Science*, 51, pp. 1163-1165, 2004.

[9] D.S. McGregor, J.T. Lindsay, R.W. Olsen, "Thermal Neutron Detection with $Cadmium_{1-x}Zinc_x$ Telluride Semiconductor Detectors," *Nuclear Instruments and Methods*, A381, pp. 498-501, 1996.

[10] D.S. McGregor, M.D. Hammig, H.K. Gersch, Y-H.Yang, and R.T. Klann,"Design Considerations for Thin Film Coated Semiconductor Thermal Neutron Detectors" *Nuclear Instruments and Methods*, A500, pp. 272-308, 2003.

[11] D. S. McGregor, R. T. Klann, J. D. Sanders, J.T. Lindsay, K.J. Linden, H.K. Gersch, P.M. De Lurgio, C.L. Fink, and E. Ariesanti, "Recent Results from Thin-Film-Coated Semiconductor Neutron Detectors," Proc. of SPIE, Vol. 4784 pp. 164-182, 2002.

[12] D.S. McGregor, R.T. Klann, H.K. Gersch, E. Ariesanti, J.D. Sanders, and B. VanDerElzen, "New Surface Morphology for Low Stress Thin-Film-Coated

[13] D.S. McGregor and R.T. Klann, US patent 6545281; allowed April 8, 2003.

[14] D.S. McGregor and J.K. Shultis, "Spectral Identification of Thin-Film-Coated and Solid-Form Semiconductor Neutron Detectors," *Nuclear Instruments and Methods*, A517, pp. 180-188, 2004.

[15] W.J. McNeil, S.L. Bellinger, T.C. Unruh, E.L. Patterson, J. K. Shultis, and D.S. McGregor, "Perforated Diode Fabrication for Neutron Detection," IEEE NSS Conf. Record, 3732-3735, 2006.

[16] D.S. McGregor, R.T. Klann, US patent 7,164,138; allowed January 16, 2007.

[17] D.S. McGregor, S. Bellinger, D. Bruno, W.L. Dunn, W.J. McNeil, E. Patterson, B.B. Rice, J.K. Shultis, T. Unruh, "Perforated Diode Neutron Detector Modules Fabricated from High-Purity-Silicon," *Radiation Physics and Chemistry*, 78, pp. 874-881, 2009.

[18] S.L. Bellinger, W.J. McNeil, T.C. Unruh, D.S. McGregor, "Angular Response of Perforated Silicon Diode High Efficiency Neutron Detectors," IEEE Nuclear Science Symposium, Waikiki, Hawaii, Oct. 28-Nov. 3, 2007.

[19] W.J. McNeil, Et al., "Preliminary Tests of a High Efficiency 1-D Silicon Pixel Array for Small Angle Neutron Scattering" , IEEE NSS Conf. Record, Oct. 2007.

[20] T. C. Unruh, S. L. Bellinger, D. E. Huddleston, W. J. McNeil, E. Patterson, Tim J. Sobering, D. S. McGregor, "Design and Operation of a 2D Thin Film Semiconductor Neutron Detector Array for use as a Beamport Monitor" *Nuclear Instruments and Methods*, A604, pp. 150-153, 2009.

[21] Kansas State University TRIGA Mark II Nuclear Reactor Facility Training Manual, September 19, 2002.

[22] J.K. Shultis and R. E. Faw, *Radiation Shielding*., La Grange Park: American Nuclear Society, 2000.

[23] G.E. Bacon, *Neutron Diffraction*, 3rd ed., Oxford: Clarendon Press, 1975.

[24] G.L. Squires, *Introduction to the Theory of Thermal Neutron Scattering*, Cambridge: Cambridge University Press, 1978.

[25] G. Shirane, S.M. Shapiro, and J.M.Tranquada, *Neutron Scattering with a Triple-Axis Spectrometer*, Cambridge: Cambridge University Press, 2002.

[26] J.B. Hoag, *Nuclear Reactor Experiments*, Princeton: D. Van Nostrand Company, 1958.

[27] G.B. West, Calculated Fluxes and Cross Sections for TRIGA Reactors, General Dynamics, 1963.

[28] S. Glasstone and A. Sesonske, *Nuclear Reactor Engineering*, New York: Van Nostrand Reinhold Company, 1981.

[29] B.J. Heuser, "Neutron Diffraction from a Mosaic Crystal and the Measurement of the Characteristic Maxwellian Temperature" (private communication), June 13, 2007.

[30] D.S. McGregor, "NE 860 Semiconductor Radiation Detectors" (Class notes), 2007.

[31] Japan Atomic Energy Agency Nuclear Data Center, "Tables of Nuclear Data", http://wwwndc.tokai-sc.jaea.go.jp/NuC/, 2007.

[32] D. Halliday, R. Resnick, and J. Walker, *Fundamentals of Physics*., New York: John Wiley & Sons Inc, 2001.

[33] D. Monti, "Development of a One-Dimensional Small Angle Neutron Scattering Instrument at the University of Illinois TRIGA Reactor Laboratory," MS Thesis, University of Illinois, 1996.

[34] Neutron scattering lengths and cross sections, Center for Neutron Research, National Institute of Standards and Technology, http://www.ncnr.nist.gov/resources/n-lengths/index.html, October 30, 2003.

[35] R.C. Gonzalez and R. E. Woods, *Digital Image Processing*, 3rd ed., Upper Saddle River: Pearson Prentice Education, 2008.

[36] Thermo Electron Corporation, "30% Boron Polyethylene", http://www.thermo.com/eThermo/CMA/PDFs/Product/productPDF_24116.pdf, May 13, 2003.

[37] D.S. McGregor, US patent 6,921,903; allowed July 26, 2005.

[38] D.S. McGregor, W.J. McNeil, S.L. Bellinger, T.C. Unruh, J.K. Shultis, "Microstructured Semiconductor Neutron Detectors," *Nuclear Instruments and Methods*, A608, pp. 125-131, 2009.

Appendix A - Evenly Spaced 2-D Interpolation

Interpolation routines used in the LabVIEW virtual instrument for the 2-D array image display are described in the following appendix. The original 5x5 matrix is replaced with a larger 5nx5n matrix, where n is the number of interpolations performed. The larger matrix is then populated using any of the following methods.

A.1 Nearest Neighbor Interpolation

Nearest neighbor interpolation performs an intensity-level assignment based on the location of the original pixel in the as compared to the new pixel. The intensity of the new pixel is matched to the largest intensity of the pixel nearest from the original image. None of the other surrounding pixel intensities are considered when using nearest neighbor interpolation. The method is simple to implement, however it is used infrequently because it produces undesirable artifacts that result from non-geometric interpolation [35].

Consider a grid with intensities known at $I(0,0)$, $I(1,0)$, $I(0,1)$, $I(1,1)$. For nearest neighbor interpolation the unknown intensity $I(0.5,0.5)$ for a point that is equally spaced from the boundaries is given by,

$$\boldsymbol{I(0.5,0.5) = \max}\begin{pmatrix} \boldsymbol{I(0,0)} \\ \boldsymbol{I(1,0)} \\ \boldsymbol{I(0,1)} \\ \boldsymbol{I(1,1)} \end{pmatrix}. \tag{A.1}$$

A.2 Bilinear Interpolation

Bilinear interpolation bases the intensity-level assignment of the new pixel on the 4 nearest neighbors from the original image. A weighted average between the 4 surrounding pixels determines the unknown pixel intensity. For evenly spaced pixels, the unknown intensity is simply the average of the 4 surrounding horizontal and vertical pixels. Bilinear interpolation gives much better results then nearest neighbor interpolation with only a small increase in processing power [35].

Consider a grid with intensities known at $I(0,0)$, $I(1,0)$, $I(0,1)$, $I(1,1)$. For bilinear interpolation the unknown pixel intensity $I(x,y)$ at any point in the grid is given by [35],

$$I(x, y) = ax + by + cxy + d \,, \tag{A.2}$$

where the four coefficients $a\ b\ c\ d$ are determined from [35],

$$a = I(1,0) - I(0,0) \tag{A.3}$$

$$b = I(0,1) - I(0,0) \tag{A.4}$$

$$c = I(0,0) - I(1,0) - I(0,1) + I(1,1) \tag{A.5}$$

$$d = I(0,0) \tag{A.6}$$

A.3 Bicubic and Bicubic Spline Interpolation

General bicubic interpolation is an extension of bilinear interpolation, in that instead of using the nearest 4 neighbors, it uses the 16 nearest neighbors. The 16 nearest neighbors each have a different spacing from the unknown pixel, so a weighted average between the 16 nearest neighbors is necessary to perform the intensity-level assignment. Bicubic interpolation guarantees the first derivative of the interpolating surface is continuous. Bicubic interpolation produces sharper images then bilinear or nearest neighbor interpolation, however bicubic interpolation requires more calculations and thus even more processing power. The standard interpolation routine for most image processing software utilizes bicubic interpolation [35].

Bicubic spline interpolation is extension of general bicubic interpolation that requires the surface to be continuous and the surface derivatives to be continuous. The extra calculations required are much more computationally intensive and provide diminishing visual improvement [35].

Consider a grid with intensities known at $I(0,0)$, $I(1,0)$, $I(0,1)$, $I(1,1)$. For general bicubic interpolation the unknown pixel intensity $I(x,y)$ is given by at any point in the grid is given by [35],

$$I(x, y) = \sum_{i=0}^{3} \sum_{j=0}^{3} a_{ij} I(x^i, y^j) \,. \tag{A.7}$$

where the 16 coefficients a_{ij} are determined from the 16 equations [35],

$$I(0,0) = a_{00} \quad , \tag{A.8}$$

$$I(1,0) = a_{00} + a_{10} + a_{20} + a_{30} \quad , \tag{A.9}$$

$$I(0,1) = a_{00} + a_{01} + a_{02} + a_{03} \quad , \tag{A.10}$$

$$I(1,1) = \sum_{i=0}^{3}\sum_{j=0}^{3} a_{ij} \quad , \tag{A.11}$$

$$I_x(0,0) = a_{10} \quad , \tag{A.12}$$

$$I_x(1,0) = a_{10} + 2a_{20} + 3a_{30} \quad , \tag{A.13}$$

$$I_x(0,1) = a_{10} + a_{11} + a_{12} + a_{13} \quad , \tag{A.14}$$

$$I_x(1,1) = \sum_{i=1}^{3}\sum_{j=0}^{3} a_{ij} i \quad , \tag{A.15}$$

$$I_y(0,0) = a_{01} \quad , \tag{A.16}$$

$$I_y(1,0) = a_{01} + 2a_{02} + 3a_{03} \quad , \tag{A.17}$$

$$I_x(0,1) = a_{01} + a_{11} + a_{21} + a_{31} \quad , \tag{A.18}$$

$$I_y(1,1) = \sum_{i=0}^{3}\sum_{j=1}^{3} a_{ij} j \quad , \tag{A.19}$$

$$I_{xy}(0,0) = a_{11} \quad , \tag{A.20}$$

$$I_{xy}(1,0) = a_{11} + 2a_{21} + 3a_{31} \quad , \tag{A.21}$$

$$I_{xy}(0,1) = a_{11} + 2a_{12} + 3a_{13} \quad , \tag{A.22}$$

$$I_{xy}(1,1) = \sum_{i=1}^{3}\sum_{j=1}^{3} a_{ij} ij \quad , \tag{A.23}$$

where the expressions above have the following identities [35],

$$I_x(x,y) = \sum_{i=1}^{3}\sum_{j=0}^{3} a_{ij} i x^{i-1} y^{j} \quad , \tag{A.24}$$

$$I_y(x,y) = \sum_{i=0}^{3}\sum_{j=1}^{3} a_{ij} x^{i} j y^{j-1} \quad , \tag{A.25}$$

$$I_{xy}(x,y) = \sum_{i=1}^{3}\sum_{j=1}^{3} a_{ij} i x^{i-1} j y^{j-1} \quad . \tag{A.26}$$

Appendix B - Amplifier Board Design

B.1 Operational Notes

Operational notes from Tim Sobering of EDL to Troy Unruh of SMART Lab on the operation of the 2-D array amplifier board as emailed on 03-03-08.

Troy,

Attached are the schematics and a layout drawing for the design. You should be able to zoom in to see the reference designators.

Each channel has a threshold adjustment pot which sets the channel threshold from 16.7% to 68.7% of the master threshold. I think they are
currently set fully clockwise so they are at 68.7% right now.

In the corner of the board are two pots. R5 permits the reduction of the external bias voltage, adjustable from 0% to 100% of the external value as you turn it CW. This only has an effect if you jumper pins 1-2
of J3 and apply an external voltage to J2. If you jumper pins 2-3 of J3, the back side of the detector is tied to ground.

The other pot is R232. This sets the master threshold to all of the channels from 0V to 1.5V as you turn it CW. The channel threshold discussed above then reduces this value for each individual channel.

The output connector is configured with signals along the inside and grounds along the outside. The pinout is shown on the schematic, but it
numbers CH 20 - 25 and then CH 1 - 19. A non-sequential pinout was required for routing.

Bias or Threshold ranges are easily changed if necessary. Keep me posted as to your testing.

Tim

--

==========
Tim J. Sobering, Director 785-532-2865 (Voice)
ELECTRONICS DESIGN LABORATORY 785-532-2092 (FAX)
124 Burt Hall
Kansas State University
Manhattan, KS 66506-0400 http://www.ksu.edu/ksuedl

B.2 Amplifier Board Schematics and Board Layout

Amplifier board schematics and amplifier board layout drawing as discussed in Appendix B.1.

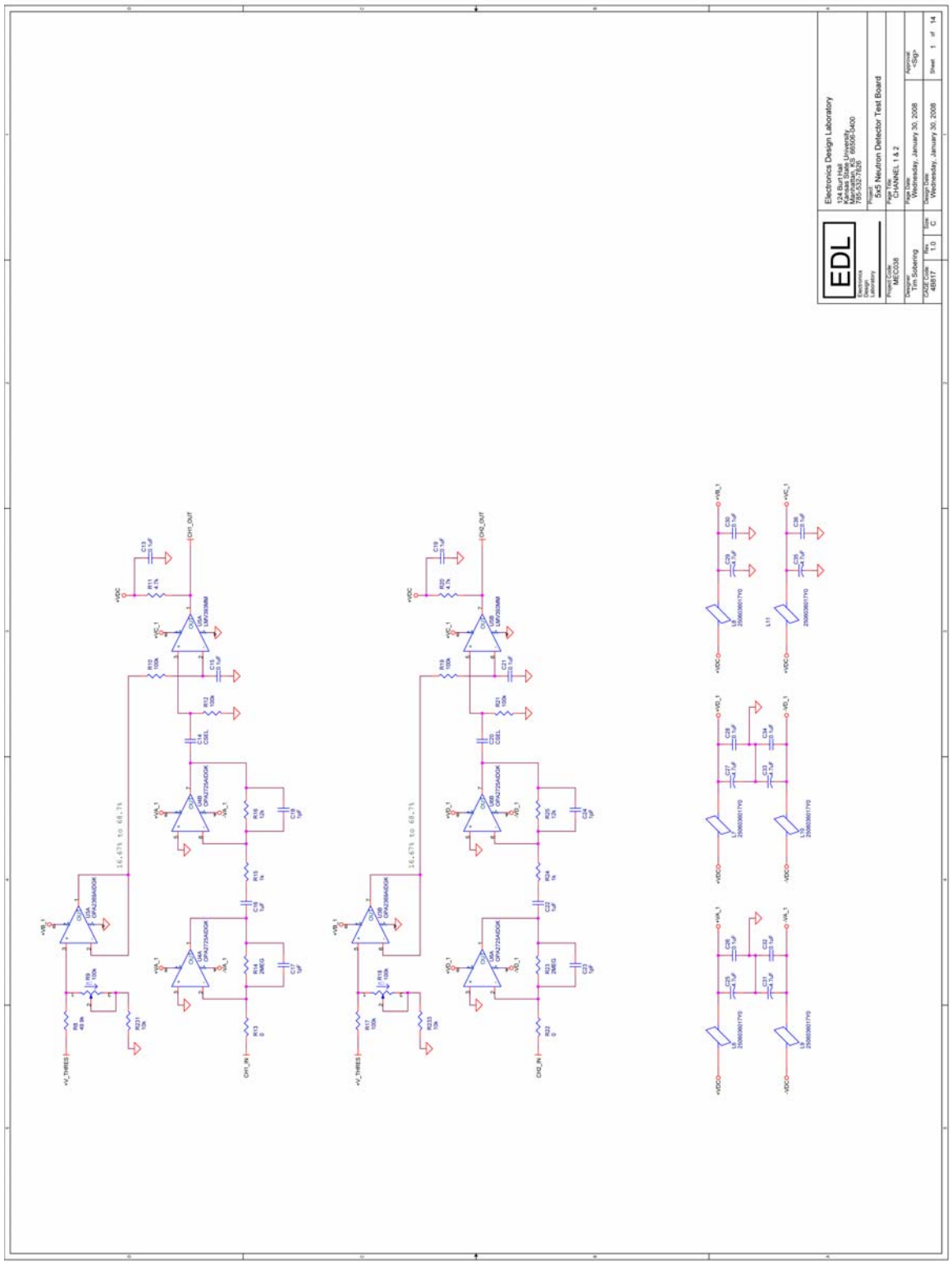

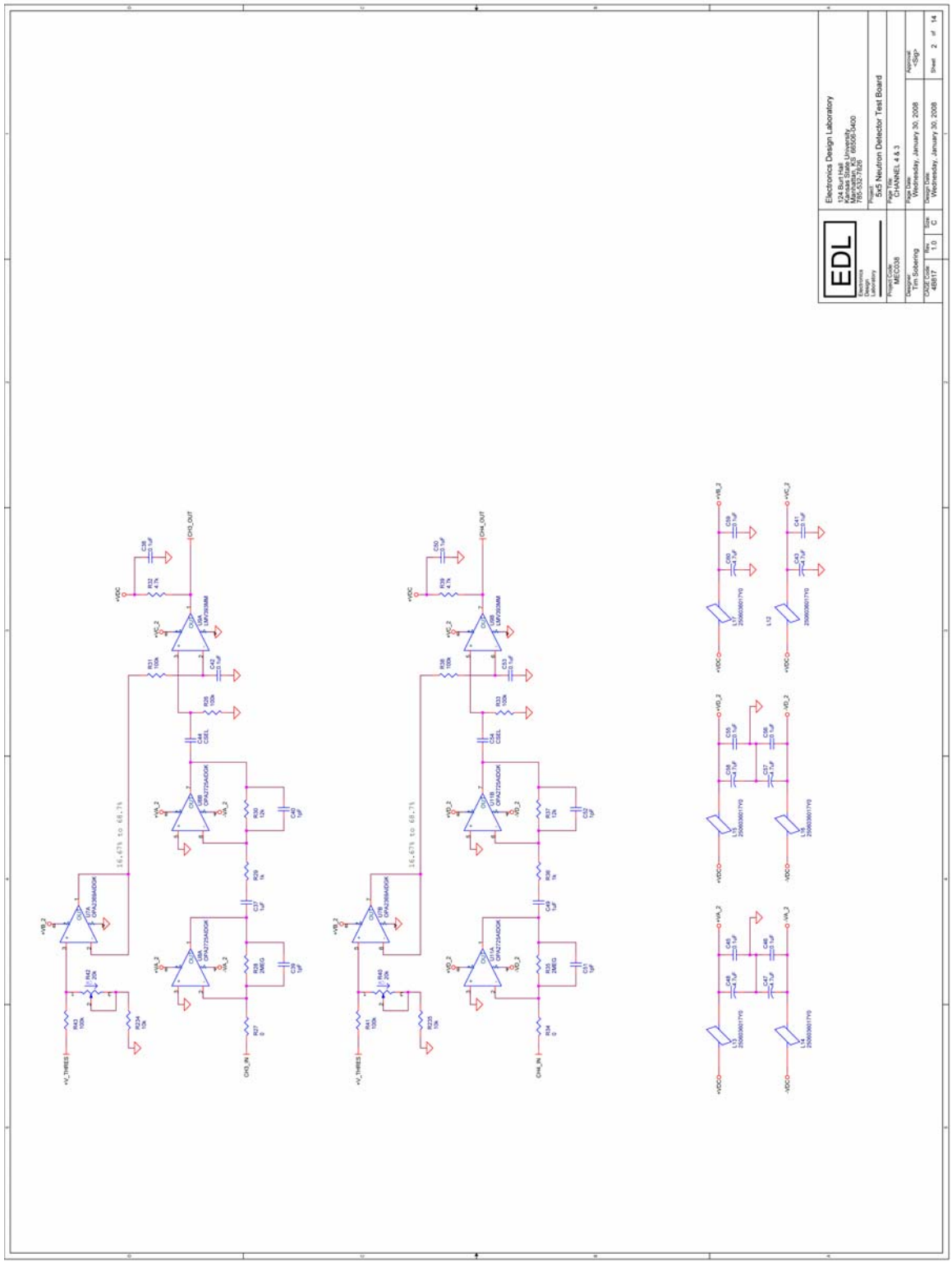
EDL
Electronics Design Laboratory
Electronics Design Laboratory
124 Burt Hall
Kansas State University
Manhattan, KS 66506-5400
785-532-7589
Project Title
5x5 Neutron Detector Test Board
Page Title
CHANNEL 4 & 3
Project Code
MECD38
Page Date
Wednesday, January 30, 2008
Design Author
Eric Sobering
Design Date
Wednesday, January 30, 2008
Assembly Variant
OrCAD Code
48817
Rev
1.0
Size
C
Sheet 2 of 14
16.67% to 68.7%
16.67% to 68.7%

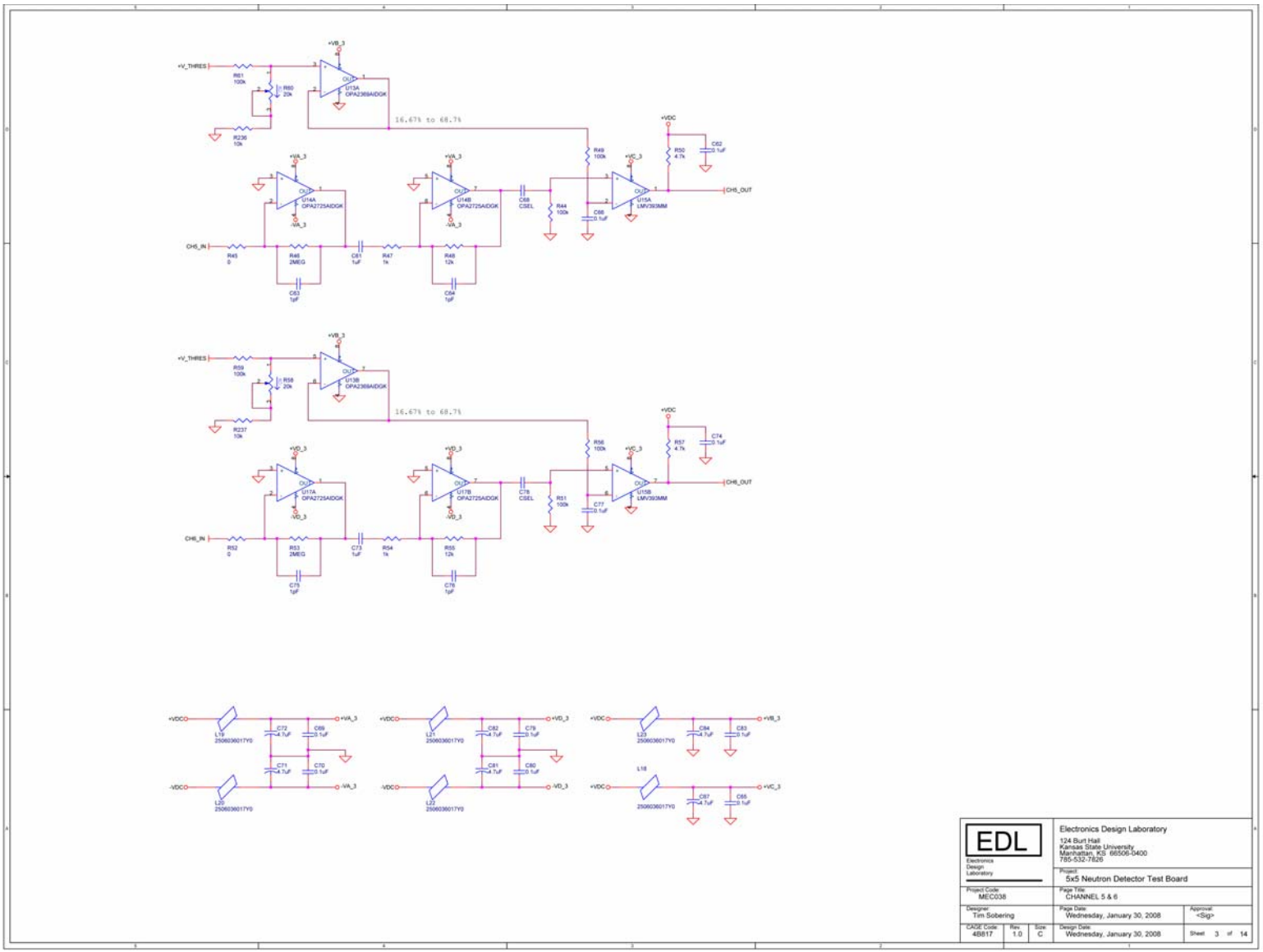
+V_THRES
R61 100k
R60 20k
R236 10k
+VB_3
U13A OPA2369AIDGK
16.67% to 68.7%
+VDC
R50 4.7k
C62 0.1uF
+VA_3
U14A OPA2725AIDGK
-VA_3
U14B OPA2725AIDGK
C68 CSEL
R49 100k
R44 100k
C66 0.1uF
+VC_3
U15A LMV393IMM
CH5_OUT
CH5_IN
R45 0
R46 2MEG
C63 1pF
C61 1uF
R47 1k
R48 12k
C64 1pF
R59 100k
R58 20k
R237 10k
U13B OPA2369AIDGK
R56 100k
R57 4.7k
C74 0.1uF
+VD_3
U17A OPA2725AIDGK
-VD_3
U17B OPA2725AIDGK
C78 CSEL
R51 100k
C77 0.1uF
U15B LMV393IMM
CH6_OUT
CH6_IN
R52 0
R53 2MEG
C75 1pF
C73 1uF
R54 1k
R55 12k
C76 1pF
L19 2506036017Y0
C72 4.7uF
C69 0.1uF
C71 4.7uF
C70 0.1uF
L20 2506036017Y0
L21 2506036017Y0
C82 4.7uF
C79 0.1uF
C81 4.7uF
C80 0.1uF
L22 2506036017Y0
L23 2506036017Y0
C84 4.7uF
C83 0.1uF
L18 2506036017Y0
C87 4.7uF
C85 0.1uF
EDL
Electronics Design Laboratory
Electronics Design Laboratory
124 Burt Hall
Kansas State University
Manhattan, KS 66506-0400
785-532-7826
Project
5x5 Neutron Detector Test Board
Project Code: MEC038
Page Title: CHANNEL 5 & 6
Designer: Tim Sobering
Page Date: Wednesday, January 30, 2008
Approval: <Sig>
CAGE Code: 4B817
Rev: 1.0
Size: C
Design Date: Wednesday, January 30, 2008
Sheet 3 of 14

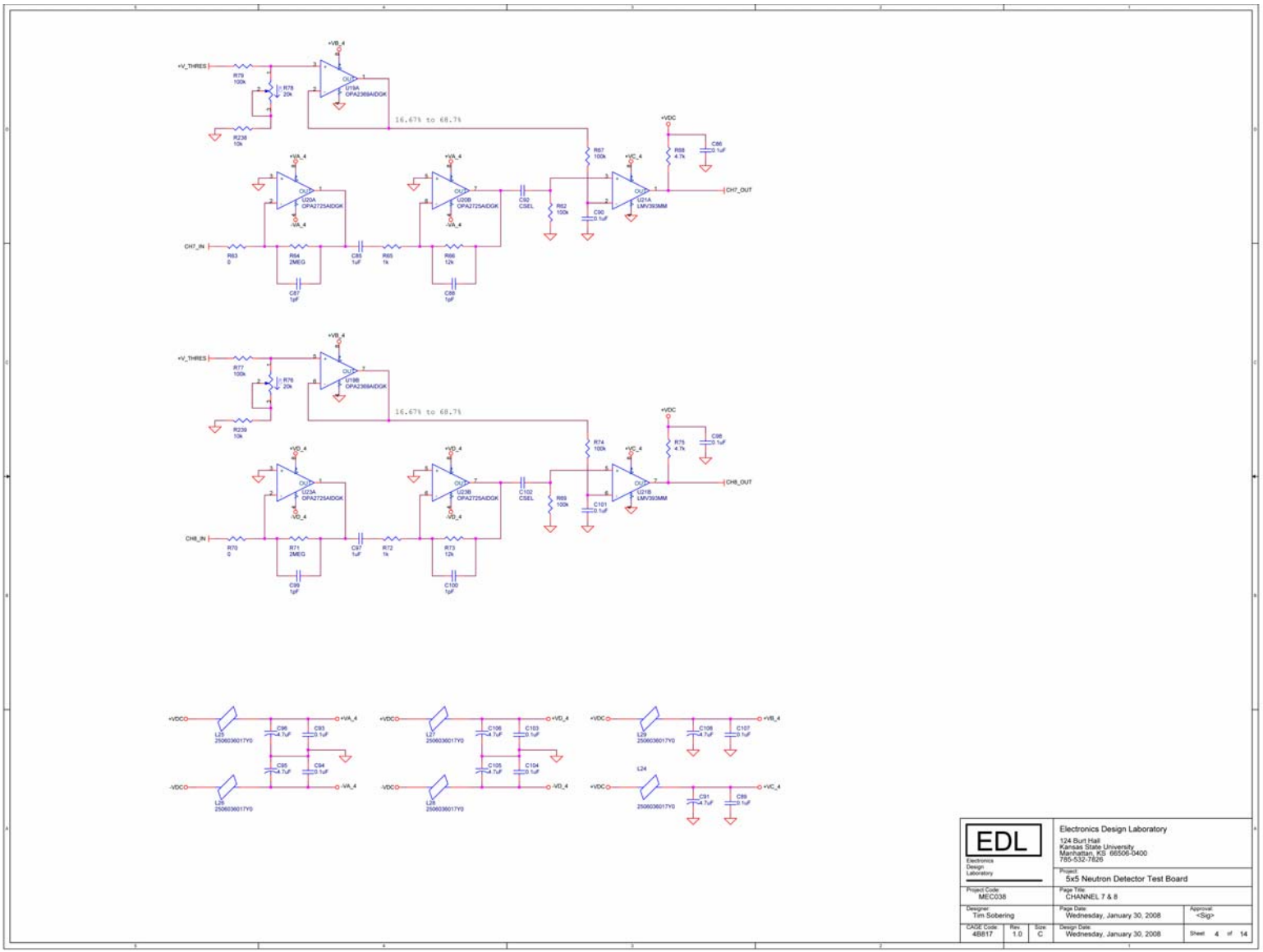
+V_THRES
R79 100k
R78 20k
R238 10k
+VB_4
U19A OPA2368AIDGK
16.67% to 68.7%
+VDC
R67 100k
R68 4.7k
C86 0.1uF
+VA_4
U20A OPA2725AIDGK
-VA_4
U20B OPA2725AIDGK
C92 CSEL
R62 100k
C90 0.1uF
+VC_4
U21A LMV393MM
CH7_OUT
CH7_IN
R63 0
R64 2MEG
C85 1uF
R65 1k
R66 12k
C87 1pF
C88 1pF
+V_THRES
R77 100k
R76 20k
R239 10k
+VB_4
U19B OPA2368AIDGK
16.67% to 68.7%
+VDC
R74 100k
R75 4.7k
C98 0.1uF
+VD_4
U23A OPA2725AIDGK
-VD_4
U23B OPA2725AIDGK
C102 CSEL
R69 100k
C101 0.1uF
+VC_4
U21B LMV393MM
CH8_OUT
CH8_IN
R70 0
R71 2MEG
C97 1uF
R72 1k
R73 12k
C99 1pF
C100 1pF
+VDC
L23 2506036017Y0
C96 4.7uF
C93 0.1uF
+VA_4
C95 4.7uF
C94 0.1uF
-VDC
L25 2506036017Y0
-VA_4
+VDC
L27 2506036017Y0
C106 4.7uF
C103 0.1uF
+VD_4
C105 4.7uF
C104 0.1uF
-VDC
L26 2506036017Y0
-VD_4
+VDC
L29 2506036017Y0
C108 4.7uF
C107 0.1uF
+VB_4
L24 2506036017Y0
C91 4.7uF
C89 0.1uF
+VC_4
EDL
Electronics Design Laboratory
Electronics Design Laboratory
124 Burt Hall
Kansas State University
Manhattan, KS 66506-0400
785-532-7826
Project
5x5 Neutron Detector Test Board
Project Code
MEC038
Page Title
CHANNEL 7 & 8
Designer
Tim Sobering
Page Date
Wednesday, January 30, 2008
Approval
<Sig>
CAGE Code
4B817
Rev
1.0
Size
C
Design Date
Wednesday, January 30, 2008
Sheet 4 of 14

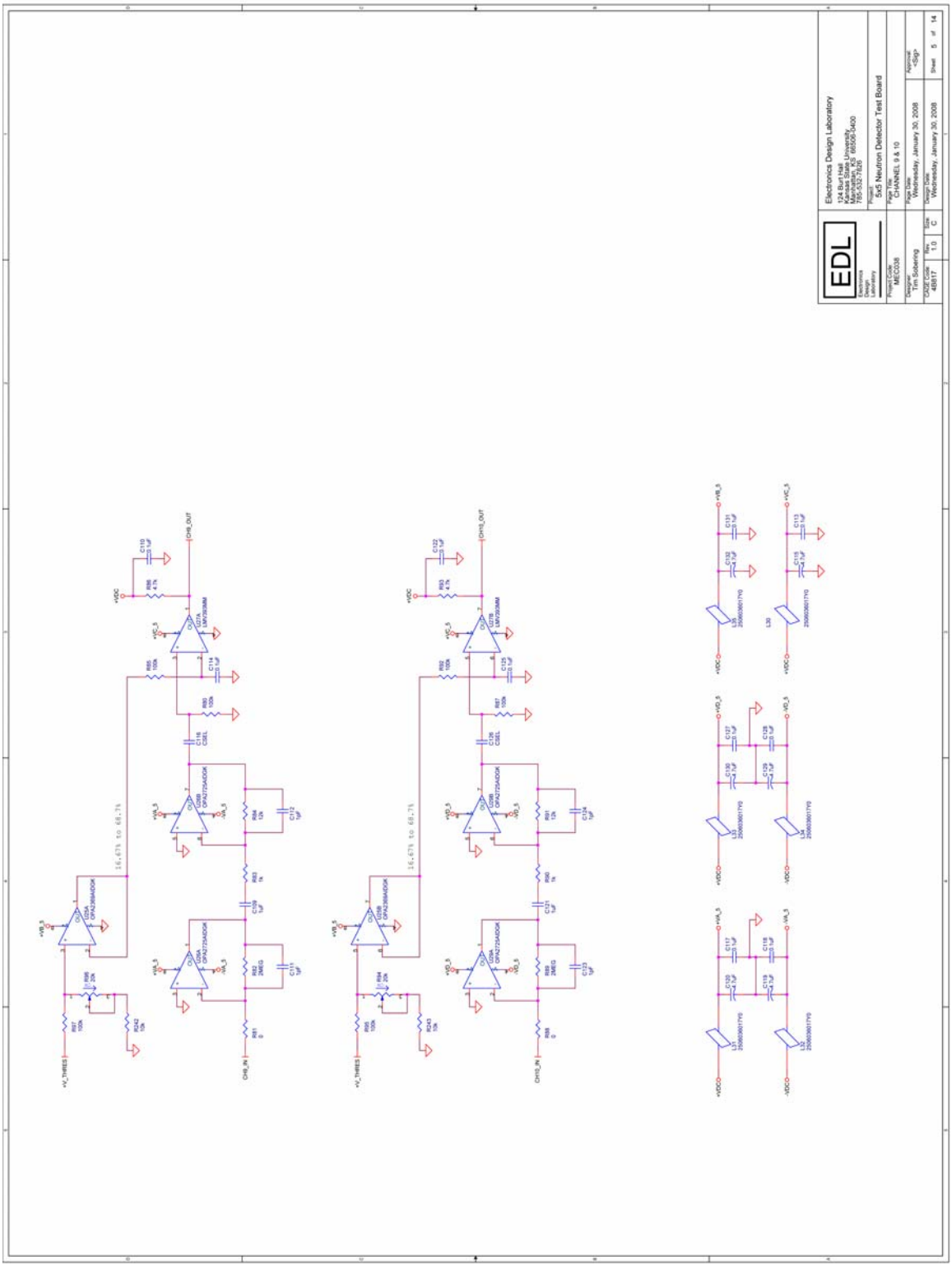
Electronics Design Laboratory
124 Burt Hall
Kansas State University
Manhattan, KS 66506-5400
785-532-7589
5x5 Neutron Detector Test Board
CHANNEL 9 & 10
Wednesday, January 30, 2008
Wednesday, January 30, 2008
Sheet 5 of 14
MEC038
No Soldering
48817
1.0
C
16.47k to 68.7k

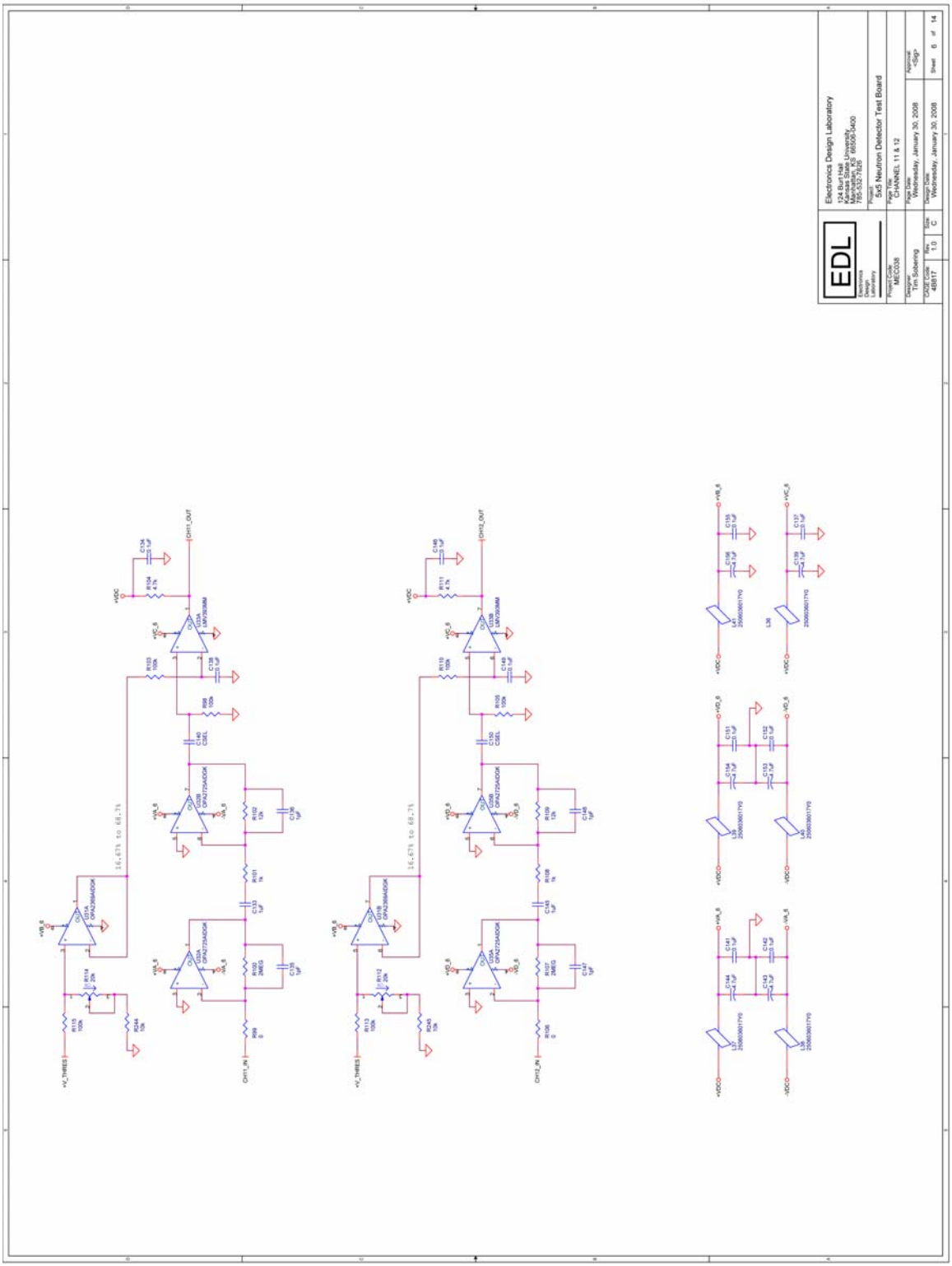
EDL
Electronics Design Laboratory
Electronics Design Laboratory
124 Burt Hall
Kansas State University
Manhattan, KS 66506-5400
785-532-7589
Project Title
5x5 Neutron Detector Test Board
Project Code: MEC038
Page Title: CHANNEL 11 & 12
Page Date: Wednesday, January 30, 2008
Design Owner: Tim Sobering
Revision: 1.0
Size: C
Design Date: Wednesday, January 30, 2008
Sheet 6 of 14
CAGE Code: 4B617
16.67% to 68.7%
CH11_OUT
CH12_OUT
CH11_IN
CH12_IN
+V_THRES
+VDC
+VDCO
-VDCO

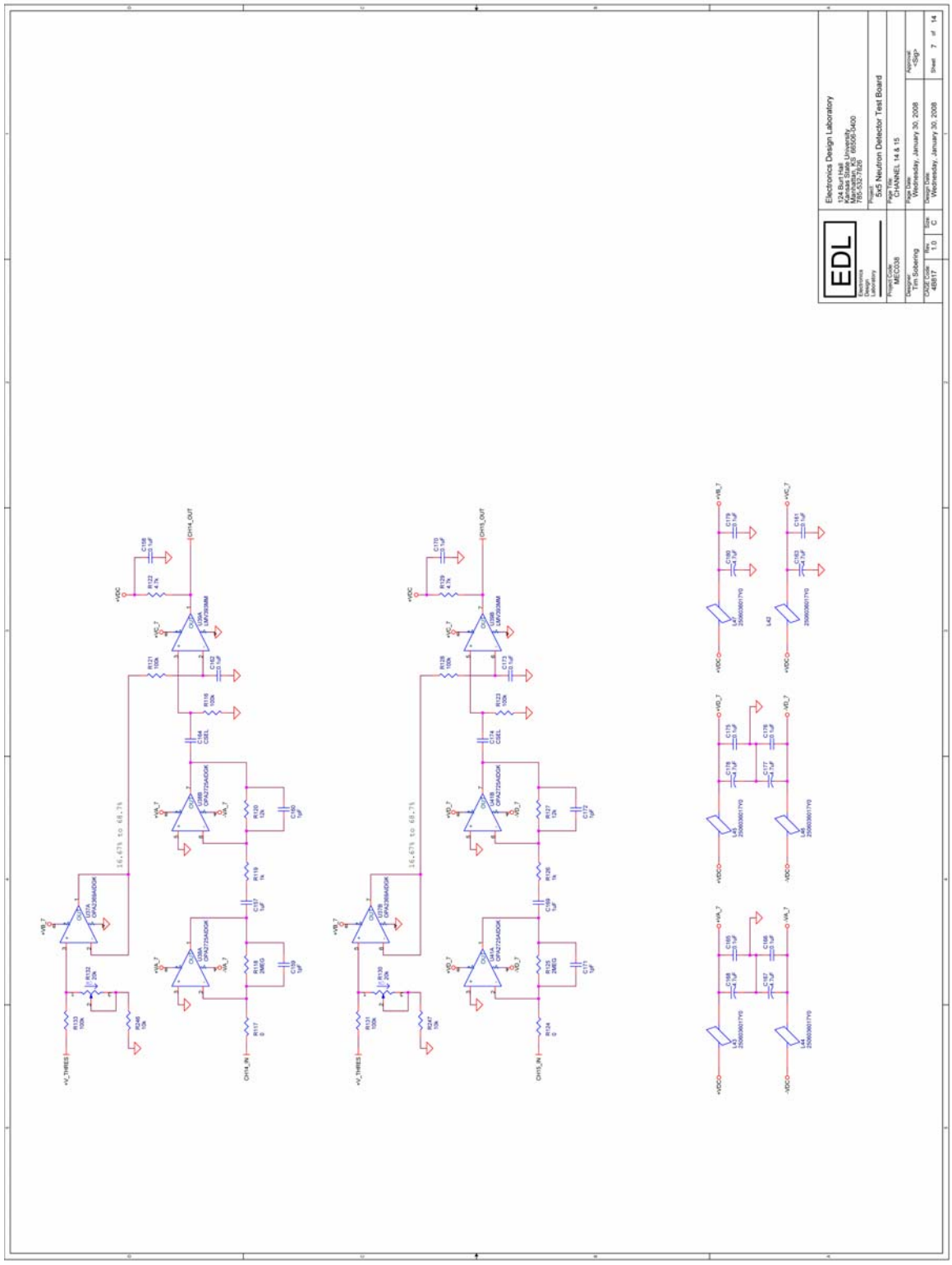
EDL
Electronics Design Laboratory
Electronics Design Laboratory
124 Burt Hall
Kansas State University
Manhattan, KS 66506-5400
785-532-7589
5x5 Neutron Detector Test Board
CHANNEL 14 & 15
Wednesday, January 30, 2008
Wednesday, January 30, 2008
Project Code: MECO38
Degree of Soldering: Thru Soldering
CAGE Code: 4B617
Rev: 1.0
Size: C
Sheet 7 of 14
16.67% to 68.7%
16.67% to 68.7%
+VDC
-VDC

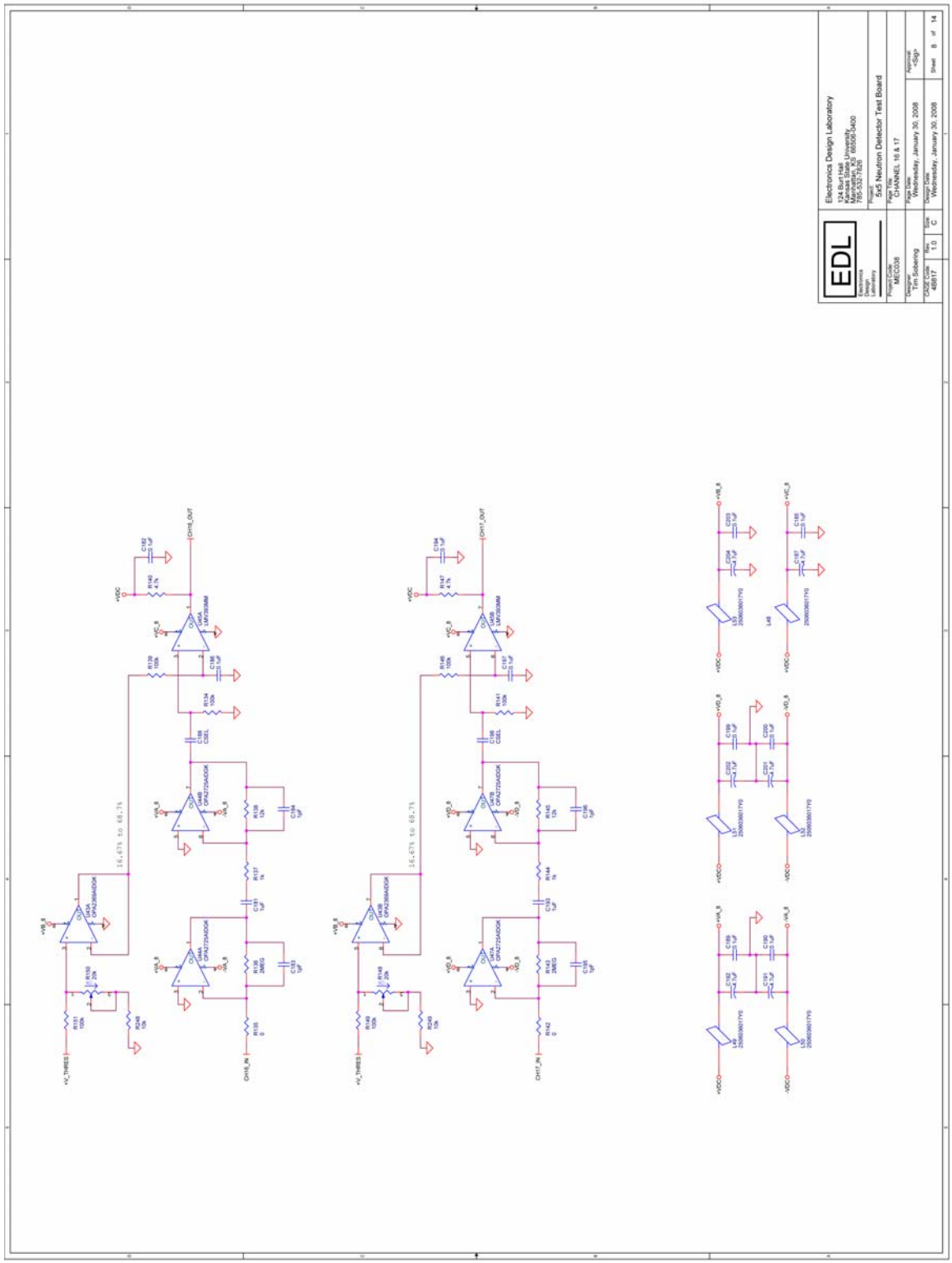
Electronics Design Laboratory
124 Burt Hall
Kansas State University
Manhattan, KS 66506-5400
785-532-7589
5x5 Neutron Detector Test Board
CHANNEL 16 & 17
Wednesday, January 30, 2008
Wednesday, January 30, 2008
MECO38
Tim Sobering
48817
1.0
C
Sheet 8 of 14
16.47k to 68.7k
CH16_OUT
CH17_OUT
+VDC
+V_THRES
CH16_IN
CH17_IN
+VB_8
+VC_8
+VA_8
+VD_8
-VDC

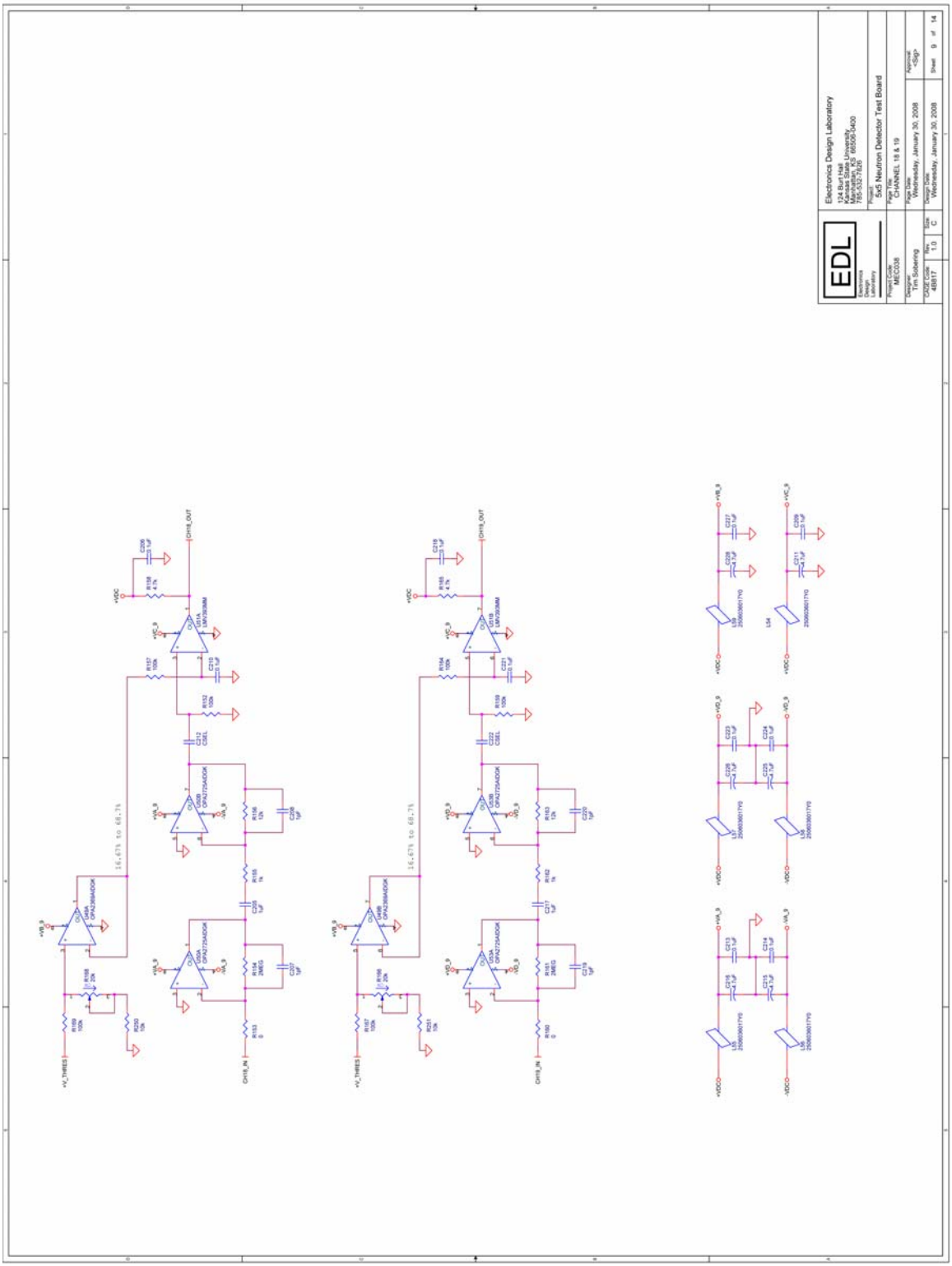
Electronics Design Laboratory
124 Burt Hall
Kansas State University
Manhattan, KS 66506-5400
785-532-7589
5x5 Neutron Detector Test Board
CHANNEL 18 & 19
Wednesday, January 30, 2008
Wednesday, January 30, 2008
MEC038
Thru Soldering
48817
1.0
C
9
14
16.47% to 68.7%
CH18_OUT
CH18_IN
+V_THRES
+VDC
+VA_9
+VB_9
+VC_9
+VD_9
-VDC
-VA_9
-VB_9
-VC_9
-VD_9

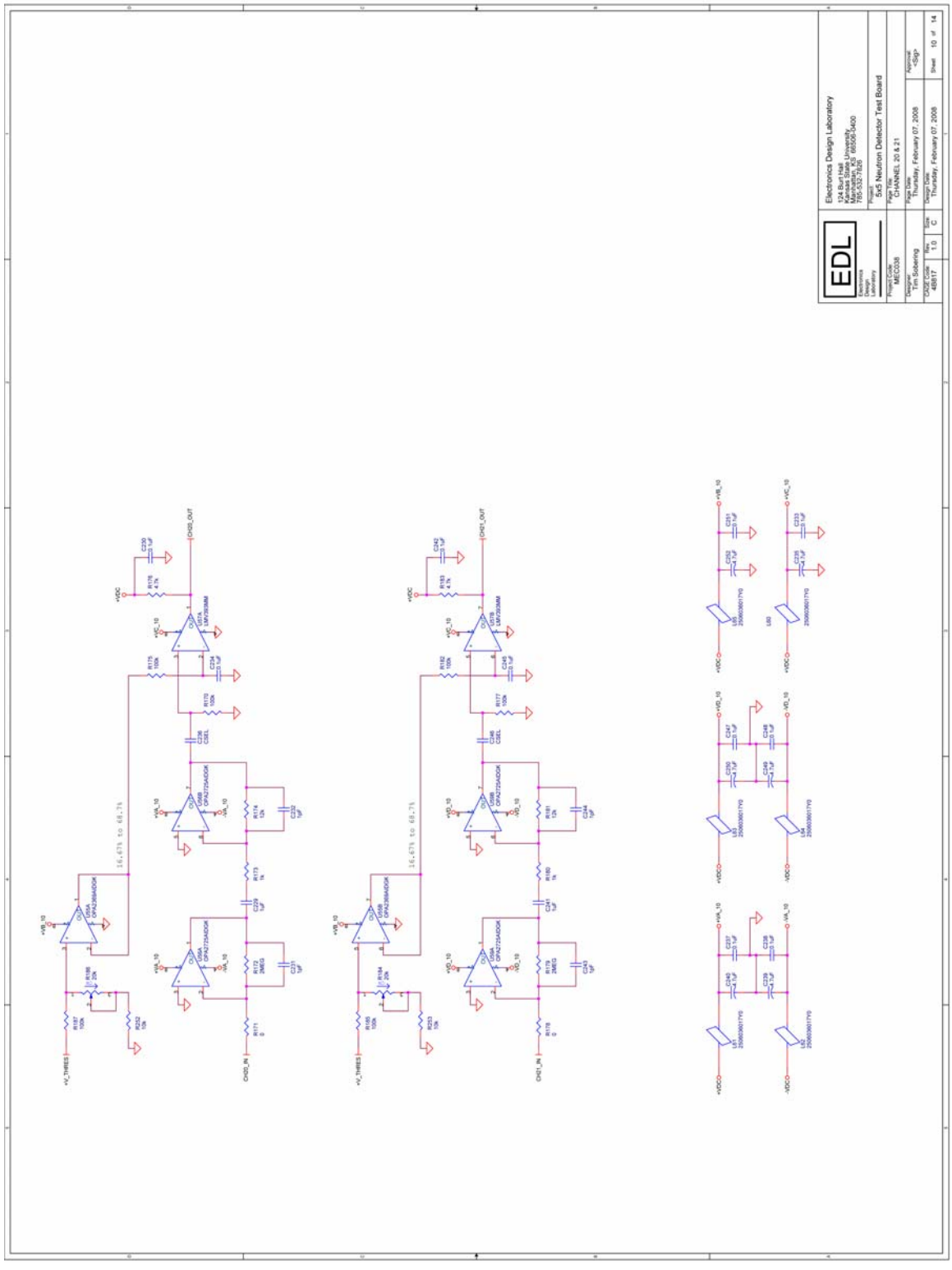
Electronics Design Laboratory
124 Burt Hall
Kansas State University
Manhattan, KS 66506-5400
785-532-7589
5x5 Neutron Detector Test Board
CHANNEL 20 & 21
Thursday, February 07, 2008
Thursday, February 07, 2008
Sheet 10 of 14
16.67% to 66.7%
CH20_OUT
CH20_IN
CH21_OUT
CH21_IN
+V_THREE
+VDC
+VB_10
+VC_10
+VA_10
+VD_10
-VDC

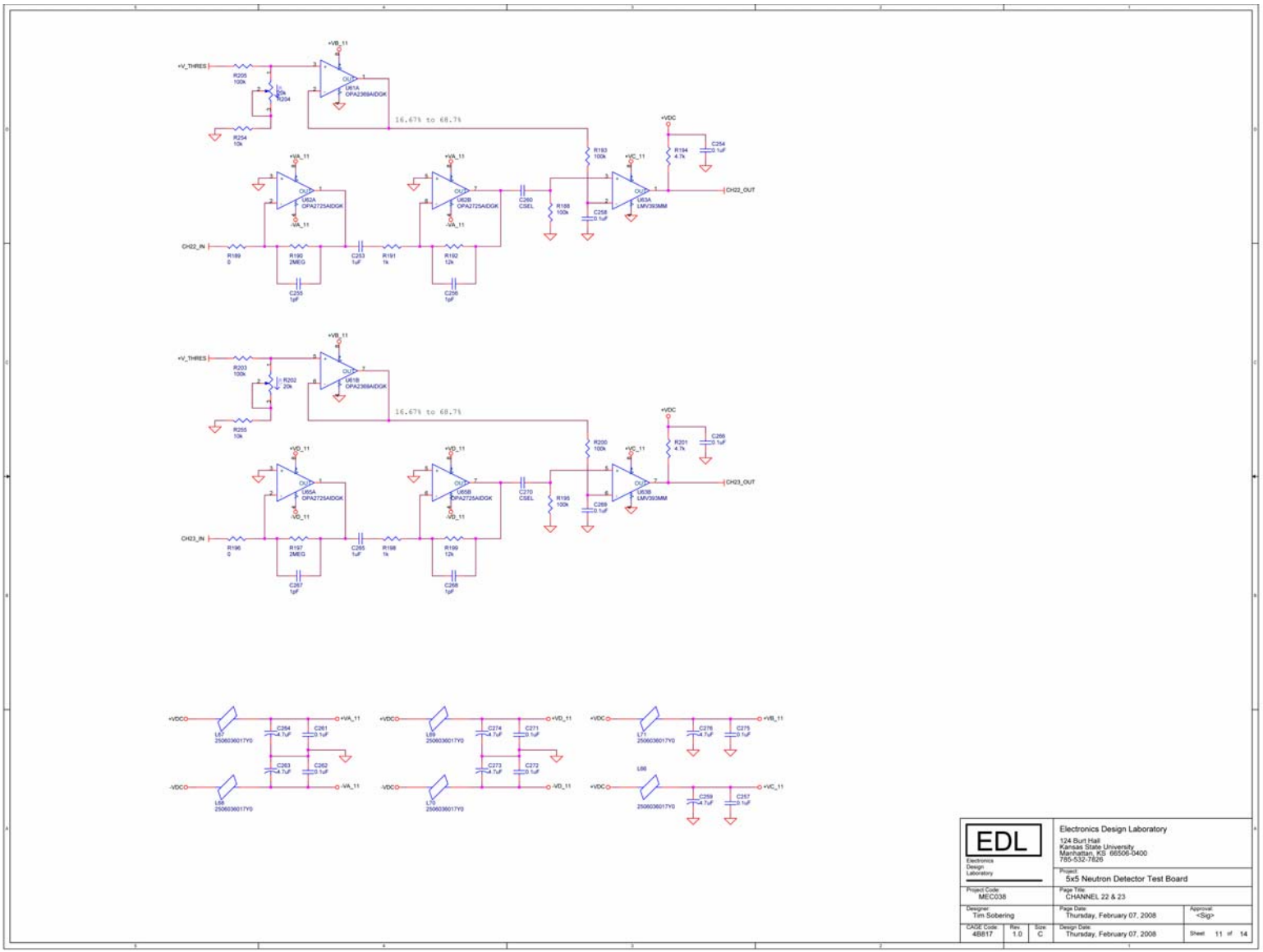
+V_THRES
R205 100k
R204 20k
R254 10k
+VB_11
U61A OPA2368AIDGK
16.67% to 68.7%
+VDC
R183 100k
R194 4.7k
C254 0.1uF
+VA_11
U62A OPA2725AIDGK
U62B OPA2725AIDGK
-VA_11
+VC_11
U63A LMV393MM
CH22_OUT
CH22_IN
R189 0
R190 2MEG
C253 1uF
R191 1k
R192 12k
C255 1pF
C256 1pF
C260 CSEL
R188 100k
C258 0.1uF
+V_THRES
R203 100k
R202 20k
R255 10k
+VB_11
U61B OPA2368AIDGK
16.67% to 68.7%
+VDC
R200 100k
R201 4.7k
C268 0.1uF
+VD_11
U65A OPA2725AIDGK
U65B OPA2725AIDGK
-VD_11
+VC_11
U63B LMV393MM
CH23_OUT
CH23_IN
R196 0
R197 2MEG
C265 1uF
R198 1k
R199 12k
C267 1pF
C268 1pF
C270 CSEL
R195 100k
C269 0.1uF
+VDC
L67 2506036017Y0
C264 4.7uF
C261 0.1uF
C263 4.7uF
C262 0.1uF
+VA_11
-VDC
L68 2506036017Y0
-VA_11
L69 2506036017Y0
C274 4.7uF
C271 0.1uF
C273 4.7uF
C272 0.1uF
+VD_11
L70 2506036017Y0
-VD_11
L71 2506036017Y0
C276 4.7uF
C275 0.1uF
+VB_11
L66 2506036017Y0
C259 4.7uF
C257 0.1uF
+VC_11
EDL
Electronics Design Laboratory
Electronics Design Laboratory
124 Burt Hall
Kansas State University
Manhattan, KS 66506-0400
785-532-7826
Project
5x5 Neutron Detector Test Board
Project Code
MEC038
Page Title
CHANNEL 22 & 23
Designer
Tim Sobering
Page Date
Thursday, February 07, 2008
Approval
<Sig>
CADE Code
4B817
Rev
1.0
Size
C
Design Date
Thursday, February 07, 2008
Sheet
11 of 14

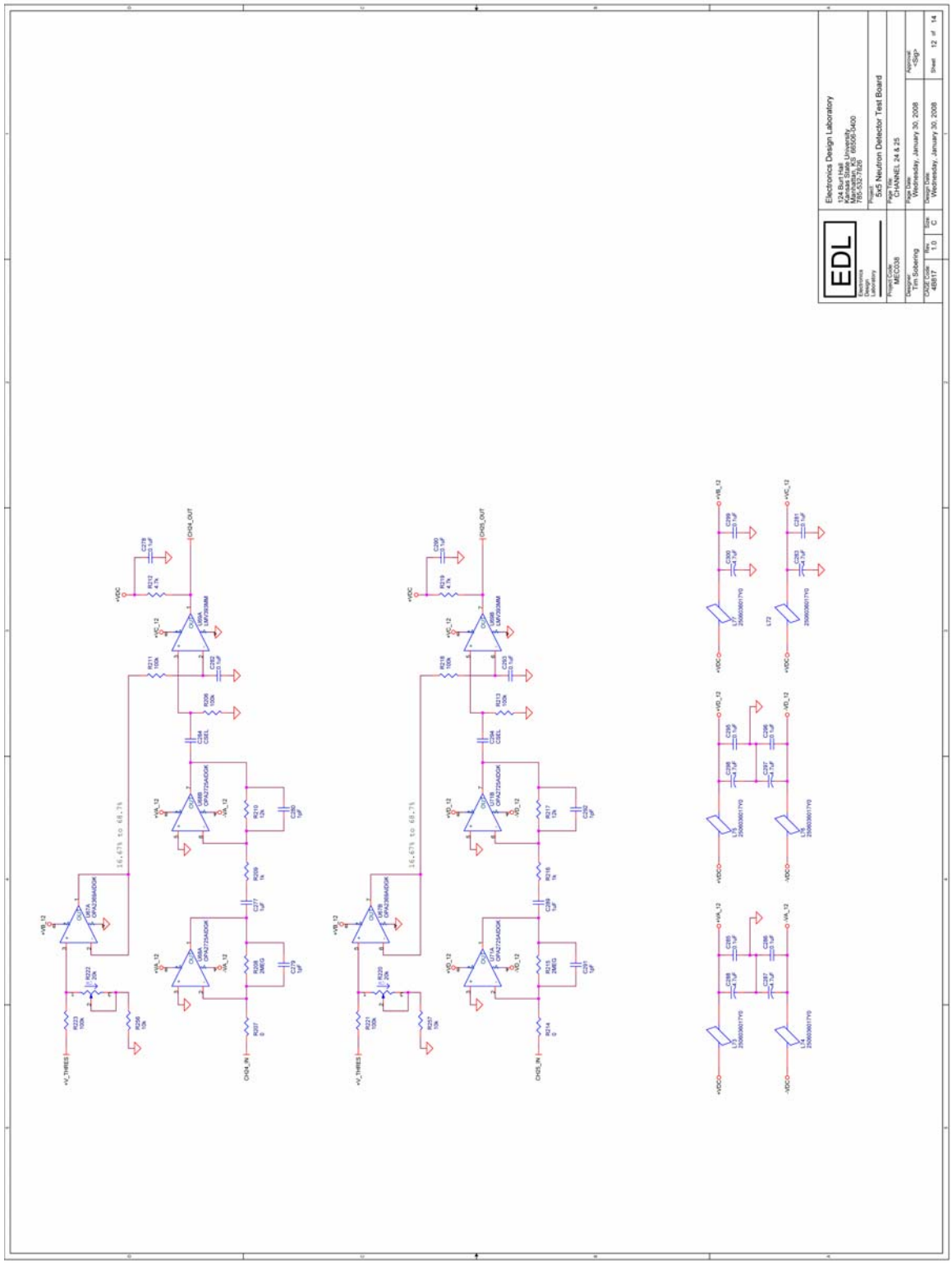
Electronics Design Laboratory
124 Burt Hall
Kansas State University
Manhattan, KS 66506-5400
785-532-7589
5x5 Neutron Detector Test Board
CHANNEL 24 & 25
Wednesday, January 30, 2008
Wednesday, January 30, 2008
MEC038
1.0
C
48817
12 of 14
16.67% to 66.7%
CH24_OUT
CH25_OUT
CH24_IN
CH25_IN
+V_THREE
+VDC
+VDCO
-VDCO

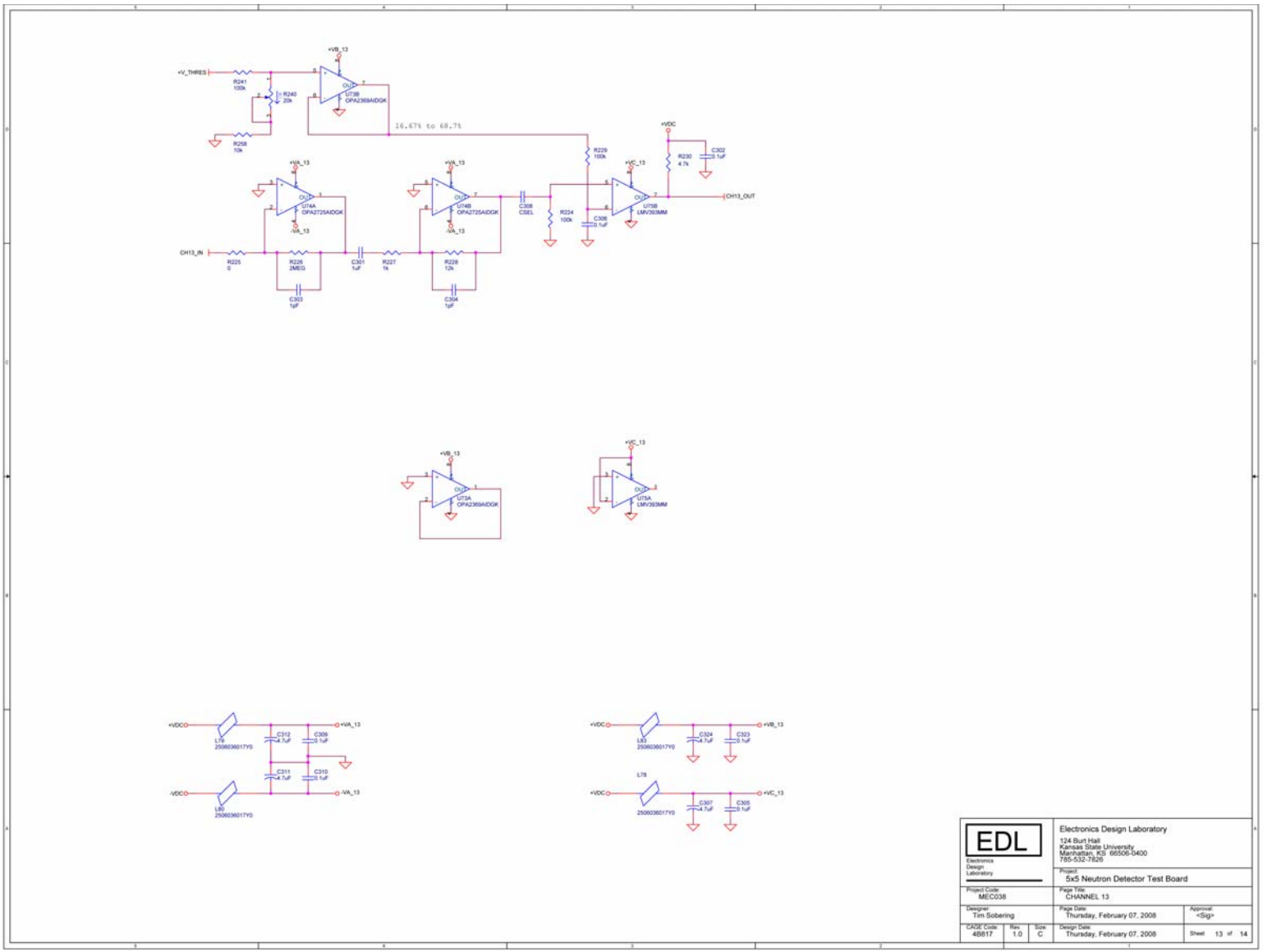

EDL Electronics Design Laboratory	Electronics Design Laboratory 124 Burt Hall Kansas State University Manhattan, KS 66506-0400 785-532-7826		
	Project: 5x5 Neutron Detector Test Board		
Project Code: MEC038	Page Title: CHANNEL 13		
Designer: Tim Sobering	Page Date: Thursday, February 07, 2008		Approval: <Sig>
CADE Code: 4B817	Rev: 1.0	Size: C	Design Date: Thursday, February 07, 2008
			Sheet 13 of 14

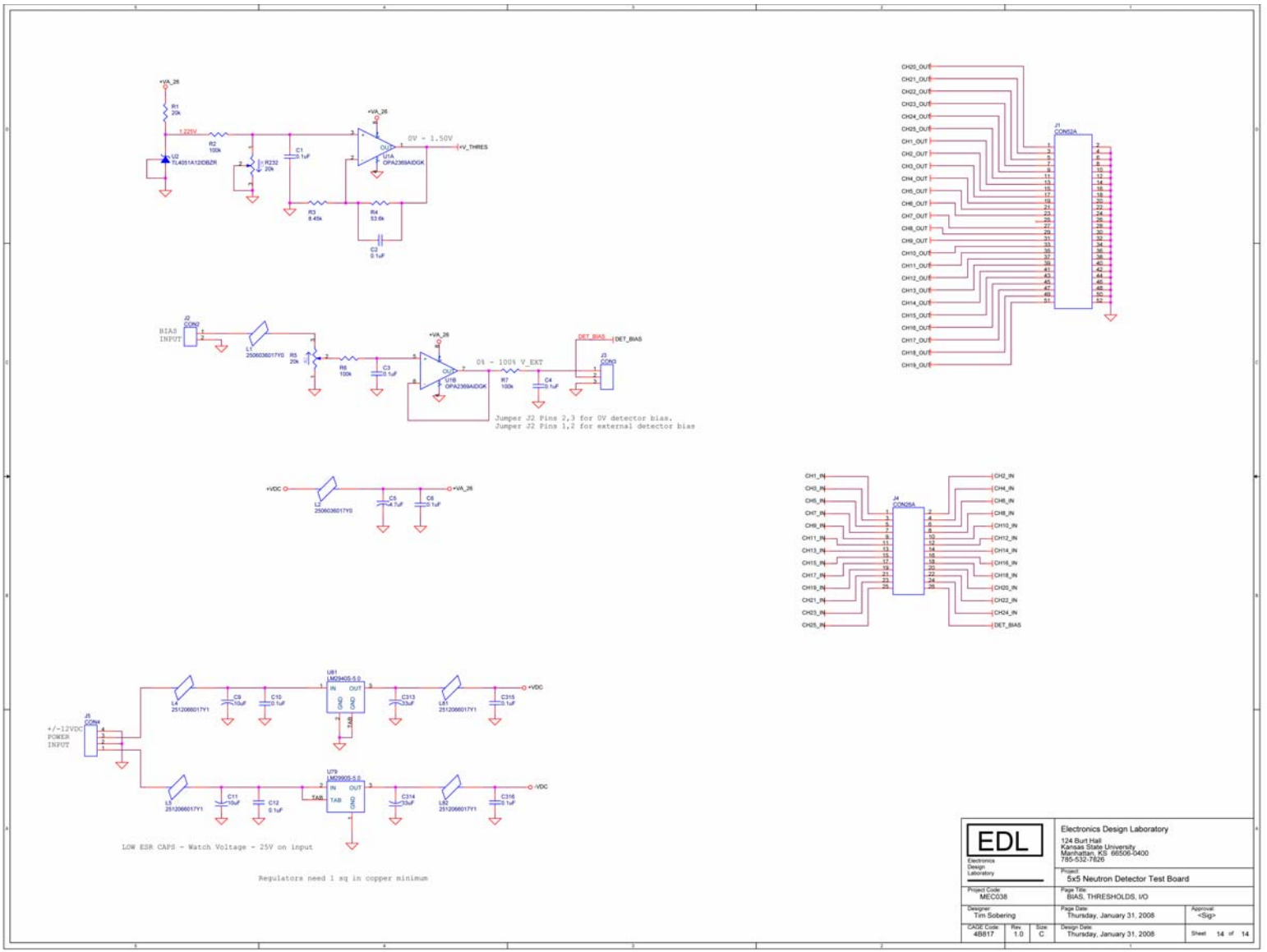
+VA_2S
R1
20k
1.225V
U2
TL4051A12IDBZR
R2
100k
R232
20k
C1
0.1uF
R3
8.45k
R4
53.6k
C2
0.1uF
U1A
OPA2369AIDGK
0V ~ 1.50V
+V_THRES
J2
CON2
BIAS
INPUT
L1
2506036017Y0
R5
20k
R6
100k
C3
0.1uF
U1B
OPA2369AIDGK
0% ~ 100% V_EXT
R7
100k
C4
0.1uF
J3
CON2
DET_BIAS
Jumper J2 Pins 2,3 for 0V detector bias.
Jumper J2 Pins 1,2 for external detector bias
+VDC
L2
2506036017Y0
C5
4.7uF
C6
0.1uF
+VA_2S
J1
CON52A
CH20_OUT
CH21_OUT
CH22_OUT
CH23_OUT
CH24_OUT
CH25_OUT
CH1_OUT
CH2_OUT
CH3_OUT
CH4_OUT
CH5_OUT
CH6_OUT
CH7_OUT
CH8_OUT
CH9_OUT
CH10_OUT
CH11_OUT
CH12_OUT
CH13_OUT
CH14_OUT
CH15_OUT
CH16_OUT
CH17_OUT
CH18_OUT
CH19_OUT
J4
CON26A
CH1_IN
CH3_IN
CH5_IN
CH7_IN
CH9_IN
CH11_IN
CH13_IN
CH15_IN
CH17_IN
CH19_IN
CH21_IN
CH23_IN
CH25_IN
CH2_IN
CH4_IN
CH6_IN
CH8_IN
CH10_IN
CH12_IN
CH14_IN
CH16_IN
CH18_IN
CH20_IN
CH22_IN
CH24_IN
DET_BIAS
J5
CON4
+/-12VDC
POWER
INPUT
U81
LM2940S-5.0
L4
2512066017Y1
C9
10uF
C10
0.1uF
C313
33uF
L61
2512066017Y1
C315
0.1uF
+VDC
U79
LM2905-5.0
L3
2512066017Y1
C11
10uF
C12
0.1uF
C314
33uF
L62
2512066017Y1
C316
0.1uF
+VDC
LOW ESR CAPS - Watch Voltage - 25V on input
Regulators need 1 sq in copper minimum
EDL
Electronics Design Laboratory
Electronics Design Laboratory
124 Burt Hall
Kansas State University
Manhattan, KS 66506-0400
785-532-7826
Project
5x5 Neutron Detector Test Board
Project Code
MEC038
Page Title
BIAS, THRESHOLDS, I/O
Designer
Tim Sobering
Page Date
Thursday, January 31, 2008
Approval
<Sig>
CAGE Code
4B817
Rev
1.0
Size
C
Design Date
Thursday, January 31, 2008
Sheet 14 of 14

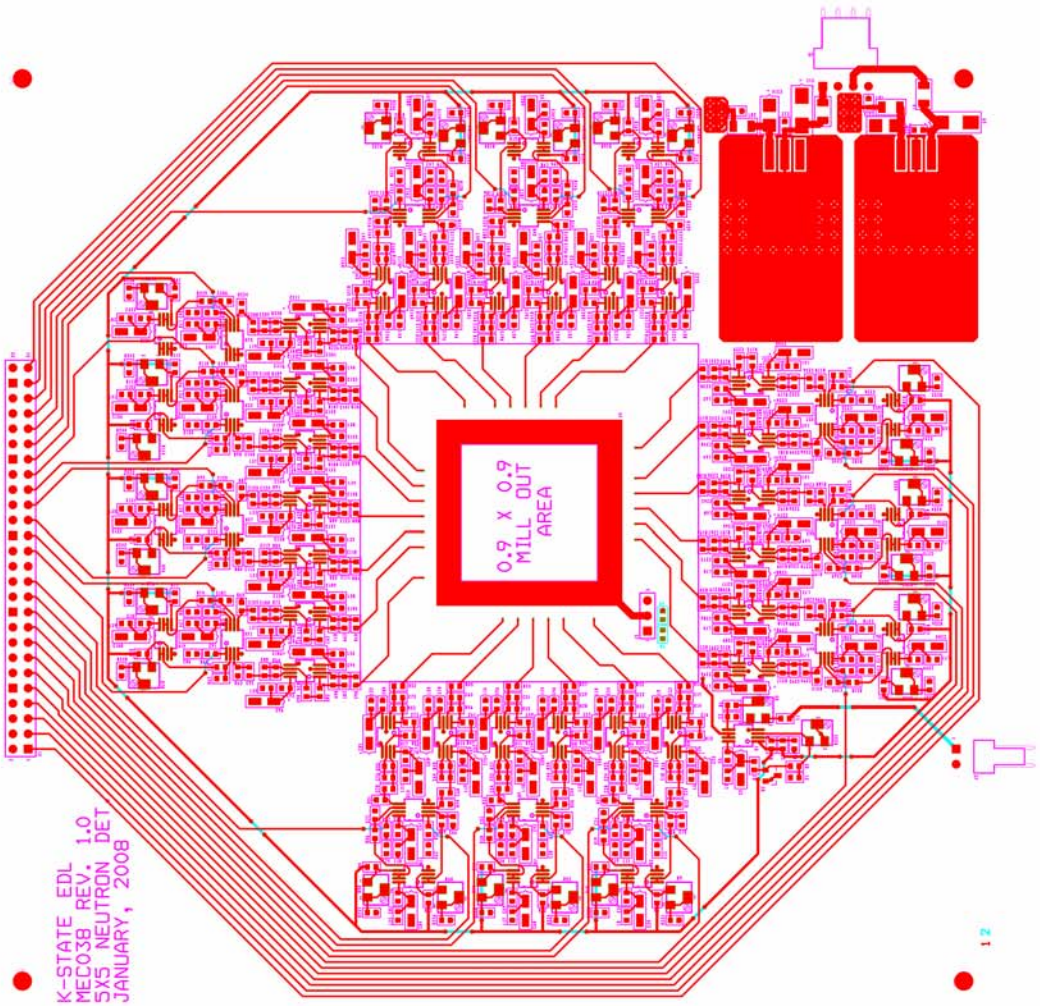
0.9 X 0.9
MILL OUT
AREA
K-STATE EDL
MEC03B REV. 1.0
5X5 NEUTRON DET
JANUARY, 2008

Appendix C - Reuter Stokes ^{3}He neutron detector pulse height spectrum and operation notes as provided by manufacturer

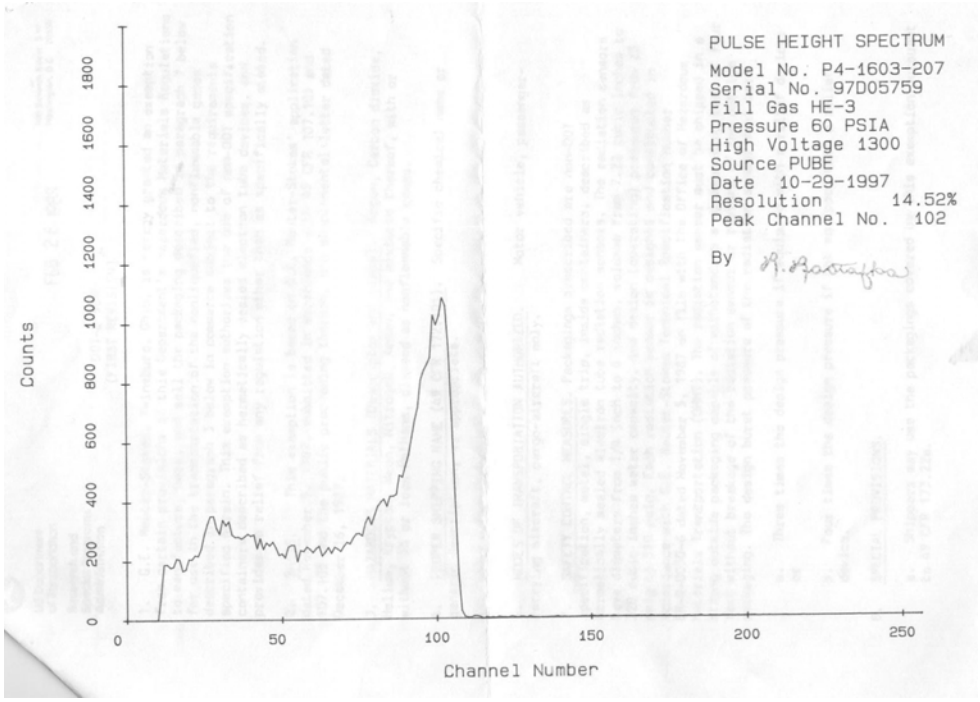

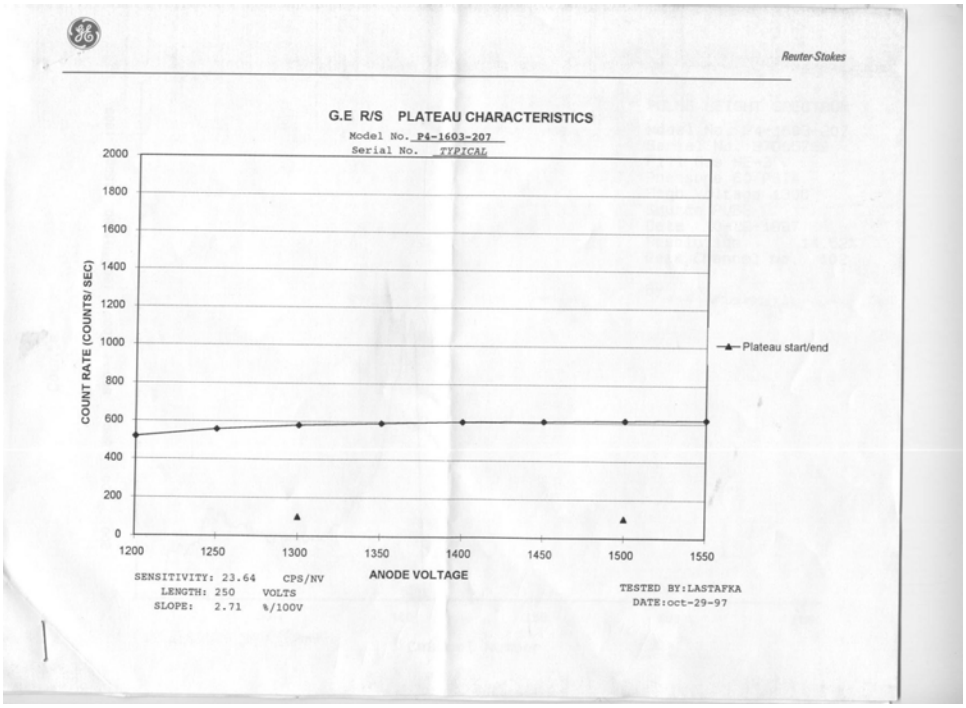

Appendix D - Beamport setup

C.1 Detector and monochromator alignments

The following are the steps required to perform an initial setup of the detector testing facility.

1. Locate rotary stages in the center of the collimator opening
2. Install ^{3}He detector on outer stage so that it is aligned with the central axis of the collimator and turn on the associated counting electronics
3. Verify motor controllers are on and without faults (red LEDs)
4. On computer open VI named beamalign.vi located on the desktop
5. Start the VI by clicking the run button
6. Click the “Detector Axis on” button
7. Click the “Find Detector HOME” button, the stage will rotate CCW until it reaches the limit switch
8. Turn the reactor on to a power of 1 kW.
9. Click the “Move to Count Position” button in the Detector Axis controls, the stage will rotate CW to a position of -15 degrees and began taking counts until it reaches +15 degrees
10. Locate the angular location of the peak counts
11. Type the peak count location on the box called “Detector Maximum Position”
12. Click the “Move to Max” button in the Detector Axis controls , the stage will move to the position and reset to zero and then move to a position of 30 degrees
13. Turn the reactor off and wait until it is safe to enter the neutron beam
14. Click the “Crystal Axis On” button
15. Click the “Find Crystal HOME” button, the stage will rotate CCW until it reaches the limit switch
16. Install the monochromator on the stage so that it is at a 0 degree Bragg angle
17. Turn the reactor on to a power of 1 kW

18. Click the “Move to Count Position” button in the Crystal Axis controls, the stage will rotate CW to a position of 5 degrees and began taking counts until it reaches 25 degrees
19. Locate the angular location of the peak counts
20. Type the peak count location on the box called “Crystal Maximum Position”
21. Click the “Move to Max” button in the Crystal Axis controls, the stage will move to the position and reset to 15
22. Type in a file location when prompted by the VI, the equipment is now ready to measure the beamport leakage spectrum.

C.2 Measuring beamport leakage spectrum

The following are the steps required to measure the beamport leakage spectrum

1. Perform steps 1-22 from Appendix C.1
2. Verify motor controllers are on and without faults (red LEDs)
3. On computer open VI named spectrum.vi located on the desktop
4. Start the VI by clicking the run button
5. Click the “Axes on” button
6. Click the “Starting Pos.” button, the stages will rotate to positions of zero degrees
7. Turn the reactor on to a power of 1 kW
8. Type the maximum desired monochromator position on the box called “Stop at”
9. Click the “Take Count” button, the stages will move in 0.1 (monochromator) and 0.2 (detector) degree increments until the stop at position is reached.
10. Type in a file location when prompted by the VI